11-15-2013

Modeling, Simulation, and Characterization of Space Debris in low-Earth Orbit

Paul D. McCall
pmcca001@gmail.com

DOI: 10.25148/etd.FI13120401

Recommended Citation

McCall, Paul D., "Modeling, Simulation, and Characterization of Space Debris in low-Earth Orbit" (2013). *FIU Electronic Theses and Dissertations*. 965.
https://digitalcommons.fiu.edu/etd/965

FLORIDA INTERNATIONAL UNIVERSITY

Miami, Florida

MODELING, SIMULATION, AND CHARACTERIZATION OF SPACE DEBRIS IN LOW-EARTH ORBIT

A dissertation submitted in partial fulfillment of

the requirements for the degree of

DOCTOR OF PHILOSOPHY

in

ELECTRICAL ENGINEERING

by

Paul David McCall

2013

To: Dean Amir Mirmiran
College of Engineering and Computing

This dissertation, written by Paul David McCall, and entitled Modeling, simulation, and characterization of space debris in low-Earth orbit, having been approved in respect to style and intellectual content, is referred to you for judgment.

We have read this dissertation and recommend that it be approved.

Jean H. Andrian

Armando Barreto

Naphtali David Rishe

Malek Adjouadi, Major Professor

Date of Defense: November 15, 2013

The dissertation of Paul David McCall is approved.

Dean Amir Mirmiran
College of Engineering and Computing

Dean Lakshmi N. Reddi
University Graduate School

Florida International University, 2013

DEDICATION

This text is dedicated to my wife and the love of my life, Natalie McCall. Without her support and sacrifice this effort would not have been possible. Thank you and I love you. 1 John 3:18

ACKNOWLEDGMENTS

First and foremost, I would like to convey my heartfelt gratitude to my mentor and research advisor, Dr. Malek Adjouadi. His support, passion, and commitment to research have been an inspiration to many young researchers including myself. His teachings, encouragement, and positive attitude have made this dissertation a reality. Throughout this entire process, from choosing internships, to preparing for presentations, writing recommendation letters, and editing this dissertation his knowledge, guidance, and patience have been truly inexhaustible. He is directly responsible for my choice to pursue graduate studies in signal and image processing. His dedication to research and his students are evident through all his actions and efforts. If blessed with the opportunity, I hope to be half the mentor to someone else that he has been to me. For the works listed above, and the numerous others not listed here, thank you.

I would like to recognize the other members of my dissertation committee, Dr. Jean H. Andrian, Dr. Armando Barreto, and Dr. Naphtali Rishe, for their continued commitment towards this research and the sage advice given throughout this process. Through numerous classroom lectures, projects, and discussions they have taught, challenged, and developed me as a young engineer. Their insight and expertise has allowed me to pursue diverse and meaningful research for which I am very appreciative.

I would like to take time to thank the other numerous scientists and engineers whom made this research possible; Dr. Leslie Vaughn and Mrs. Millay Morgan for their oversight of the Local Area Sensors program at the AFRL, Dr. Madeleine Naudeau, for her role as advisor and mentor during the Summer Scholars Program at the AFRL, Mr.

Chris Dodson for laying a foundation with the radiant flux modeling efforts, Mrs. Rachel Sharples for help, guidance, and contributions in all thermal-related simulation endeavors, Dr. Scott Milster for his help in astronomical conversions, Mr. Marlon Sorge for his assistance regarding astrodynamics and debris modeling, Mr. Tom Farrell for his guidance and expertise in optical systems, and Dr. Paul LeVan, Dr. Moriba Jah, and Dr. Carolin Frueh for their knowledge and guidance on many aspects of this research.

I would like to thank the many science, math, history, and literature teachers from elementary, middle, and high school that provided the much needed challenges, encouragement, and patience necessary to enable this life-long student with a thirst for knowledge.

My lab mates in the Center for Advanced Technology and Education at Florida International University, Krishna Vedala and Anas Eddin, have provided many thoughtful insights, laughs, and interesting discussions for which I am very thankful.

I would like to thank my family. My brothers, Philip McCall and Sean McCall, and sister, Heather, have all been a tremendous inspiration, guiding light, and support structure throughout my life. My parents, Philip and Phyllis McCall have been a blessing for which I cannot be thankful enough.

This work was supported by the National Science Foundation under grants CNS-0959985, CNS-1042341, HRD-0833093 and IIP-1338922 and IIP-1230661. The author of this dissertation was partially supported by the Department of Defense (DoD) through the National Defense Science & Engineering Graduate Fellowship (NDSEG) Program, and through participation in the Air Force Research Laboratory Summer Scholars

Program. The author is supported through the Betty G. Reader Graduate Scholarship from Florida International University. Use of STK 10 was provided via the Educational Alliance Program partnership between Florida International University and Analytic Graphics Inc. Dissemination and presentation of this work would not be possible without the support provided by Dr. Jaydeep Mukherjee and the Florida Space Grant Consortium.

ABSTRACT OF THE DISSERTATION

MODELING, SIMULATION, AND CHARACTERIZATION OF SPACE DEBRIS IN LOW-EARTH ORBIT

by

Paul David McCall

Florida International University, 2013

Miami, Florida

Professor Malek Adjouadi, Major Professor

Every space launch increases the overall amount of space debris. Satellites have limited awareness of nearby objects that might pose a collision hazard. Astrometric, radiometric, and thermal models for the study of space debris in low-Earth orbit have been developed. This modeled approach proposes analysis methods that provide increased Local Area Awareness for satellites in low-Earth and geostationary orbit. Local Area Awareness is defined as the ability to detect, characterize, and extract useful information regarding resident space objects as they move through the space environment surrounding a spacecraft.

The study of space debris is of critical importance to all space-faring nations. Characterization efforts are proposed using long-wave infrared sensors for space-based observations of debris objects in low-Earth orbit. Long-wave infrared sensors are commercially available and do not require solar illumination to be observed, as their received signal is temperature dependent. The characterization of debris objects through means of passive imaging techniques allows for further studies into the origination, specifications, and future trajectory of debris objects. Conclusions are made regarding the aforementioned thermal analysis as a function of debris orbit, geometry, orientation with respect to time, and material properties. Development of a thermal model permits the characterization of debris objects based upon their received long-wave infrared signals. Information regarding the material type, size, and tumble-rate of the observed debris objects are extracted. This investigation proposes the utilization of long-wave infrared radiometric models of typical debris to develop techniques for the detection and characterization of debris objects via signal analysis of unresolved imagery.

Knowledge regarding the orbital type and semi-major axis of the observed debris object are extracted via astrometric analysis. This knowledge may aid in the constraint of the admissible region for the initial orbit determination process. The resultant orbital information is then fused with the radiometric characterization analysis enabling further characterization efforts of the observed debris object. This fused analysis, yielding orbital, material, and thermal properties, significantly increases a satellite's Local Area Awareness via an intimate understanding of the debris environment surrounding the spacecraft.

TABLE OF CONTENTS

CHAPTER PAGE

LIST OF TABLES

TABLE PAGE

LIST OF FIGURES

FIGURES PAGE

LIST OF ABBREVIATIONS AND ACRONYMS

AEOS	Advanced Electro Optical System
AIUB	Astronomical Institute of the University of Bern
AR	Admissible region
BASS	Broadband Array Spectro-graph System
CCD	Charged Coupled Device
CDT	Charged Coupled Device Debris Telescope
CWT	Continuous Wavelet Transform
dB	Decibels
DoD	Department of Defense
ESA	European Space Agency
FEA	Finite Element Analysis
FOV	Field-of-view
FPA	Focal plane array
GEO	Geostationary or Geosynchronous orbit
GEODSS	Ground-based Electro-Optical Deep Space Surveillance
GTO	geostationary-transfer orbits
HAMR	High area-to-mass ratio
IC	Intelligence Community
IOD	Initial orbit determination
IR	Infrared
IRAS	Infrared Astronomical Satellite
ISAR	Inverse synthetic aperture radar

LAA	Local Area Awareness
LEO	Low-Earth orbit
LMT	Liquid Mirror Telescope
LSM	Least Squares Method
LWIR	Long-wave infrared
MASTER	Meteoroid and Space Debris Terrestrial Environment
MCT	Mercury Cadmium Telluride
MEO	Middle-Earth orbit
MWIR	Mid-wave infrared
NASA	National Aeronautics and Space Administration
NEO	Near-Earth-object
RAAN	Right ascension of ascending node
RPM	Rotations per minute
RSO	Resident space object
RTE	Radiative thermal equilibrium
SBO	Space-based optical
SBSS	Space Based Space Surveillance
SDT	Space Debris Telescope
SEET	STK Space Environment and Effects Tool
SNR	Signal-to-noise ratio
SOAP	Satellite Orbit Analysis Program
SOCIT	Satellite Orbital Debris Characterization Impact Test
SRDI	Single range Doppler interferometry

SSN	United States Space Surveillance Network
STK 10	Systems Tool Kit 10
TAROT	Rapid Action Telescopes for Transient Object
TASAT	Time-domain Analysis Simulation for Advanced Tracking
TIRA	Tracking and Imaging Radar System
TSA	Too Short Arc
WISE	Wide-field Infrared Survey Explorer

LIST OF SYMBOLS

λ	Wavelength
T	Temperature
L	Blackbody radiance
Υ	Throughput
Φ	Radiant flux
R	Range vector
δ, θ	Angles between normal vector and range vector
c	Speed of light
h	Planck’s constant
k	Boltzmann’s constant
D	Astronomical unit
σ	Stefan-Boltzmann constant
α_e	Earth depression angle
I	Irradiance
A	Area
γ, δ	Earth and Sun angles
α	Absorptivity
ε	Emissivity
G	Universal Constant of Gravitation
M	Mass of the Earth
T	Orbital period
ΔT	Differential orbital period

a	Semi-major axis
Δa	Differential semi-major axis
P	Power

1. INTRODUCTION

October 4, 1957 was an historic day for all nations as it marked the launch of Sputnik 1, the first artificial satellite placed in Earth-orbit. This was a meaningful day for all humanity as it symbolized a great technological feat and set the stage for future space research and technological achievements. Historians disagree as to the beginning of the Space Age; however it can be stated that with confidence that the problem of space debris has its genesis in the launch of Sputnik 1.

In general, space debris is defined as man-made material in space that no longer serves any useful purpose. Spacecraft whose lifespan has ended and whose orbits are uncontrolled, jettisoned rocket bodies, objects released during missions, and fragments caused by collisions or explosion in space can all be classified as space debris. With the advent of the Space Race in the late 1950's the United States as well as the Union of Soviet Socialist Republics began to put payloads, rocket bodies, and ultimately debris into Earth-orbit at a rapid pace. At that time international agreements or guidelines for the usage of space did not exist. This lack of self and multi-nation regulation resulted in many objects being placed in orbits ranging from low-Earth orbit, altitudes below 2000 km, to geostationary orbit, 35,786 km, without deorbiting capabilities. Objects placed in Earth-orbit will naturally decay due to gravitational forces and atmospheric drag acting upon the object. However, this method of deorbiting is dependent upon many factors including size, mass, material composition, but most of all altitude. In the year following the launch of the Sputnik 1 spacecraft the United States launched Vanguard 1 into a middle-Earth orbit, from 2000 km to 35,786 km. The Vanguard 1 spacecraft was not designed with the thought that it would need to be de-orbited in the future, thus it will remain in orbit for close to 2000 years.

In 1967 the United Nations agreed upon the Outer Space Treaty which outlines procedures for human activities in space. However at the time of this treaty the problem of space debris was not considered and the treaty does not stipulate any specific provision regarding space debris. The treaty proclaims that harmful contamination should be avoided during space exploration and that nations should adopt appropriate measures to ensure this, without defining what “harmful contamination” or “appropriate measures” consisted of. As of today there are loose international guidelines, set forth by the European Space Agency and National Aeronautics and Space Administration, which exist for the deorbiting of spacecraft in low-Earth orbit within 25 years of launch. These guidelines were developed to mitigate the possible exponential growth in the number of man-made space objects. The exponential growth of debris objects is due to the proposition of Kessler syndrome in 1968. National Aeronautics and Space Administration’s Donald Kessler proposed a scenario in which the amount and density of debris in low-Earth orbit reaches a critical mass at which point debris collides with other debris resulting in a cascading and stochastic debris environment which creates an increasingly greater likelihood of collisions.

While many satellites are designed with de-orbiting capabilities, less of these designs have been implemented to comply with the 25-year rule. The 25-year rule has seen little compliance on an international level and has become reduced to merely a recommendation. Partially due to this non-compliance, the amount of payloads in Earth-orbit has steadily increased from 1957 until now. However, the amount of space debris over that same timespan has seen a significant increase. The most widely used orbital region is that of low-Earth orbit and this has resulted in a global maximum spatial density of space objects between 800 and 1000 km in altitude.

While applying various shielding techniques to spacecraft may protect against collisions with debris smaller than 1 cm in diameter, no such techniques apply for debris ranging from 1 cm to 10 cm in size. Debris of this size is commonly referred to as the ‘lethal population’ as impacts will significantly affect the mission capabilities of the spacecraft and possibly render the spacecraft inoperable. Monitoring and tracking of this size debris is not yet practical and therefore collision avoidance maneuvers cannot be utilized to mitigate collision risks. When the energy-to-mass ratio of a collision is greater than 40 J/g a catastrophic collision ensues where the satellites may shatter and separate into several fragments, significantly and instantaneously adding to the amount of debris objects. To date four catastrophic events have occurred. In 1991 the inactive payload COSMOS-1034 and a fragment of the COSMOS-296 spacecraft collided. In 1996 the first recorded natural collision involving an active satellite occurred when the operational French CERISE micro-satellite and a fragment of an Ariane-1 upper stage collided. In 2005 a collision occurred between a Thor Burner IIA upper stage and a fragment of a CZ-4B, third stage. In 2009 the first collision between two satellites happened when the active Iridium-33 satellite and the decommissioned Cosmos-2251 satellite collided. These satellites impacted each other at a speed in excess of 40,000 km/h which resulted in the complete break-up of both satellites with 1400 trackable debris objects, greater than 10 cm in size, being created.

There are other means of creating space debris as became evident in 2007 when China destroyed one of its defunct weather satellites, Fengyun-1C, while demonstrating their anti-satellite missile capabilities via an Earth-launched missile. When destroyed, the Fengyun-1C was at an orbital altitude of 900 km. As a result more than 2700 trackable debris objects were created with the National Aeronautics and Space Administration estimating more than 150,000 debris objects created with a size greater than 1 cm. A year later in February of 2008 the United States destroyed one of their spy satellites, the USA-193, via a kinetic missile impact. A notable difference being that the US-destroyed satellite was in a much lower orbit when destroyed thus created few pieces of lasting debris with most of the debris rapidly re-entering and deteriorating in the Earth's atmosphere.

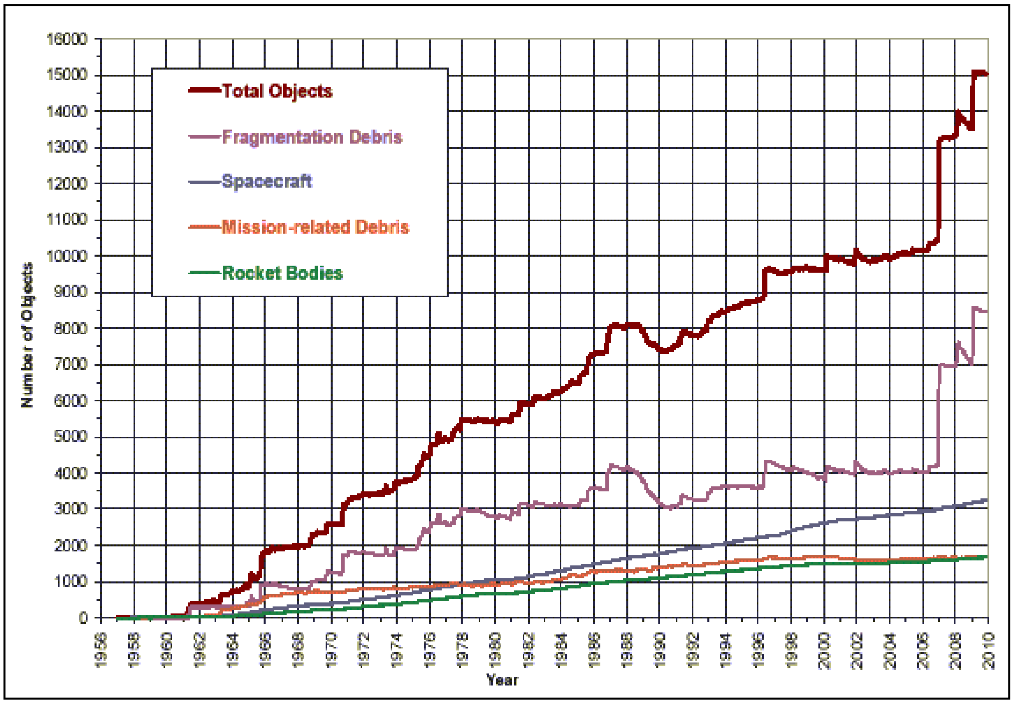

Figure 1.1: Monthly number of objects in Earth-orbit by object

To deal with the monitoring and tracking of space objects, the United States Space Surveillance Network is tasked with observing and cataloging objects in Earth orbit. To date the Space Surveillance Network tracks over 22,000 objects from 29 strategically placed optical and radar sites around the world. The Space Surveillance Network is the most complete and accurate source of the orbital parameters, radar-cross section, and other information pertaining to the space debris, rocket bodies, and functional and non-functional spacecraft. However, detectability and measurement accuracy are limited by the size of the orbital object. Using conventional techniques, objects at low-Earth orbit may be routinely tracked if they are greater than 10 cm in size while the lower limit for objects in geostationary orbit is 1 m in size. Observation and tracking of objects that exceed these thresholds has proved useful in preventing debris collisions in recent years due to the build-up of space tracking capabilities.

In 2009 alone, nine debris collision-avoidance maneuvers were performed by satellites under National Aeronautics and Space Administration control, and over thirty-two collision-avoidance maneuvers were performed in the year following the Iridium 33 - Cosmos 2251 collision, between February 2009 and 2010, with one maneuver performed by China. However, there exists a substantial amount of debris objects that cannot be observed and cataloged due to their size and orbit. A large number of these untrackable objects, the lethal population, are of a size and mass that could be potentially threatening to the operational safety of spacecraft in low-Earth orbit. Optimizing the use of collision-avoidance maneuvers and performing these maneuvers for currently untracked debris objects would ensure continued operation and usefulness of the spacecraft.

Many satellite operators, both foreign and domestic, rely in part on the capabilities of the United States Space Surveillance Network for the operational safety of their spacecraft. The goal of this current study is to increase a satellite's Local Area Awareness. For the research presented in this dissertation, the local area is defined as the 500 km radius sphere that surrounds the sensor platform or observing satellite in Earth orbit. Local Area Awareness is defined as the ability to detect, characterize, and extract useful information regarding resident space objects as they move through the local area relative to any spacecraft. Modeling and simulation, accompanied by radiometric and astrometric analysis of space debris will allow the spacecraft to gain insight into the space and debris environment surrounding it. Thermal radiometry is the measure of energy received from a satellite at infrared wavelengths. In the context of this dissertation astrometry is the scientific measurement of the position and motion of satellites. Local Area Awareness capabilities would allow the spacecraft operator, maintainer, or owner, to have a continuous and responsive link monitoring the dynamics of the surrounding space environment. It is thought that this added "awareness" can be made available through the implementation of small, relatively inexpensive onboard optical local area sensors. Since the system will be implemented on a space-based platform, problems due to distortion and atmospheric absorption are avoided.

Compact, simple on-board sensors are one solution for providing the data necessary for the analysis of debris objects. Sensors responsive in the long-wave infrared waveband are studied in this dissertation. Long-wave infrared imaging techniques offer many potential benefits when applied to the remote sensing of space debris. Long-wave infrared imaging technologies may allow for the imaging of objects with the Sun in the field-of-view without saturation of the imaging system. This type of sensor includes the ability to perform thermal characterization. Imaging space objects in the long-wave infrared band has the inherent advantage of not being completely dependent upon Solar or Earth illumination which makes observations and measurements possible even in partial or total eclipse. It is most efficient to observe the debris at their dominant thermal emission wavelengths as predicted by Wien's Displacement Law. Since orbital debris will have temperatures ranging from approximately 100-400K, their emissions will be primarily in the 7-30 μm waveband. Long-wave infrared sensors in the 7-14 μm wavebands, which are commercially available, would be attractive options to consider, especially when the development of a prototype system is considered. Thus, the goal of this investigation is to build long-wave infrared-based radiometric models of typical types of debris and use such models to develop techniques for detecting and characterizing debris by signal analysis of unresolved imagery.

Debris does not have any internal heat sources. The temperature of debris objects is dependent on the duration of time the object is illuminated by, or receiving radiative energy from, the Sun. Thermal radiation emitted by the Earth illuminating the object, Earthshine, can produce a large reflected signal. This illumination source can be particularly important during eclipse. However, the work presented in this dissertation only looks at the self-emitted component of the LWIR signal.

This temperature and wavelength dependence is expressed in Planck's equation for blackbody radiation. The spectral radiance of a blackbody is dependent upon the waveband of interest and the temperature of the emitting object. Therefore if one is concerned with the imaging of objects in the long-wave infrared band, the model, assumptions, analyses, and processes leading to the determination of the object temperature need to be accurate and plausible.

The characterization of space debris is important because an understanding of the structure, mass, shape, and material properties may help researchers to further extract needed information regarding the orbit and origination of such debris, as well as aid in orbit propagation calculations. To this end the radiometric aspect of this research is focused on the long-wave infrared signatures of space debris. In order to determine and model the long-wave infrared signatures of such debris in orbits between low-Earth orbit and geosynchronous orbit, a representative and accurate thermal model must be developed.

The radiometric analysis in this dissertation focuses solely on the long-wave infrared waveband, however the astrometric analysis and the pixel-speed classifier is sensor type agnostic. This means that the astrometric analysis is not tied to, or dependent upon, any specific sensing technology or waveband sensitivity.

A pixel-speed based classifier for rapid orbit characterization and trajectory analysis of debris objects in low-Earth orbit, based on the projected pixel-speed of the object across the focal plane array, would be a vital resource for the situational safety of satellites. The current study will quantify the ability of a satellite in low-Earth orbit to monitor, detect, catalog, and register objects, in a semi-autonomous manner and perform the required variance analysis through multiple observations of the same object. If this technique can be implemented, it would enable satellite operators to have an accurate understanding of imminent debris threats, both trackable and untrackable, and the space environment surrounding the observing spacecraft. This type of trajectory analysis is of greater significance when two-line element sets are not available. Two-line element sets for debris objects, which could be indicative of possible debris collision-threats, may not be available due to the size of the debris object, inaccurate orbit metrics, or previous uncorrelated object tracks.

With all trends showing that space debris will become more and more of a problem in the coming decades, it is necessary to investigate means of increasing a spacecraft's Local Area Awareness through the accumulation of information regarding astrometric and radiometric analysis of space debris that may pass within close proximity to the spacecraft. Through analysis, this information is converted into knowledge pertaining to the physical, material, and thermal characteristics of the debris object as well as its current and future orbital track.

The study documented in this dissertation will be laid out in three parts. The first part, Chapter 1 and Chapter 2, is composed of this introduction and a subsequent literature search documenting much of the current and past relevant work related to this field. The second part will focus completely on the modeling aspects of this research with consecutive chapters individually detailing the astrometric, radiometric, and thermal modeling efforts conducted by the author. Chapter 6 and Chapter 7, detailing the astrometric analysis and radiometric analysis separately, will be presented in part three followed by the final chapter formalizing the conclusions of this study.

2. LITERATURE REVIEW

2.1. Classical initial orbit determination methods

The practices and processes for initial orbit determination (IOD) and orbit determination have been well documented and continue to be of significance in the field of space debris research. Classical methods proposed by Laplace and Gauss [1], [2], have been used to estimate the motion of celestial bodies for centuries. An improvement over the classical methods of Laplace and Gauss for initial orbit determination of space debris is presented in [3].

The methods of Laplace and Gauss, in their approach to initial orbit determination, were limited to certain heliocentric orbital types. Having the ability of observing the same object from multiple sites on the same orbital pass was not practically realizable. They were also limited by the computing power which they had available to them. This naturally led to iteration-based approaches to the problem of initial orbit determination based on the estimated values of range from observer to observed object, ρ, and distance, r, from the center of force to the observed object. This approach is known as Escobal's double-r iteration method [4], where reasonable values are chosen for the initial scalar values of r_1 and r_3, the distance from the center of force to the observed object for the first and third observation.

The latest of the classical methods is the method proposed by Gooding for angles-only initial orbit determination [5]. Gooding's method is similar to the method proposed by Escobal in the sense that it is a range-iteration method and is based on the iteration of range values for two of the three unknown ranges. The difference between these two methods is at which step in the process the orbital dynamics are introduced. Escobal's method utilizes two time differences relative to the middle observation as the target functions while Gooding's method derives the objects position during the second observation based upon the assumed position of the object at the first and third observation times. The target function in Gooding's method then becomes the projection of the object's position on a plane which is perpendicular to the known observer's line of sight during for the second observation. In both methods the range estimates, ρ_1 and ρ_3, are used to define the orbital plane and the two positions within the plane corresponding to the observations. At this point Gooding's method introduces the known times and therefore the dynamics of the object while Escobal's method continues by computing additional positions within the orbital plane based on geometry alone.

2.2. Other orbit determination methods and associated topics

When observing space debris or any other space object, from ground-based observing stations, the measurements taken are referred to as a Too Short Arc (TSA). A TSA itself cannot provide enough information in order to determine the orbit of the observed object, yielding only two angular observations, right ascension and declination, there are four equations in six unknown orbital elements, [6]. Right ascension and declination are two angular measurements which make up astronomical coordinates on the celestial sphere, as shown in Figure 2.1 below. In this case, for successful IOD, two or more TSAs need to be linked or correlated to the same physical object. The linkage and correlation problem between TSA's for orbit determination has been well documented in previous literature, [7]–[13]. While some work has concentrated particularly on this problem relative to space debris, [3], [6], [9], [14].

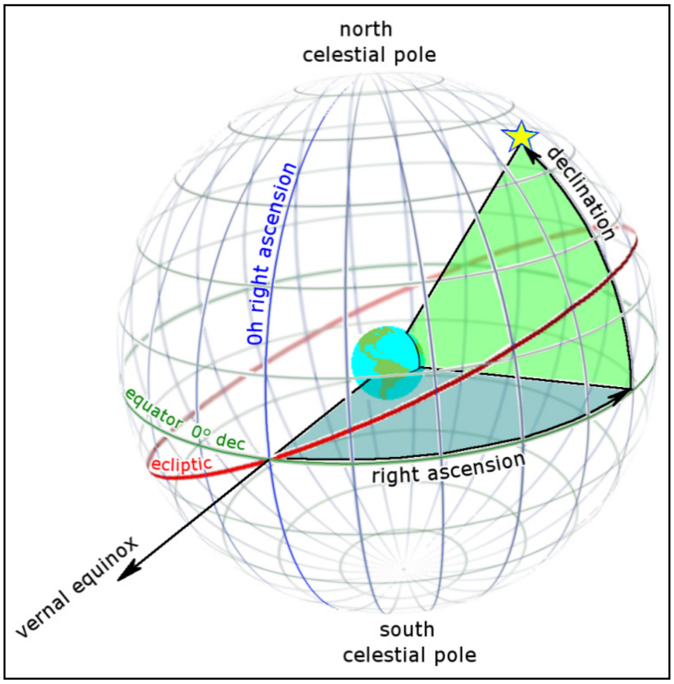

Figure 2.1: Celestial Sphere, Right Ascension and Declination

2.2.1. Too Short Arc observations

The concept of admissible region is introduced and utilized for correlation purposes in [8]. The admissible region (AR) is a compact subset of orbits, represented as a plane of two unknown variables (usually range and range-rate), which can be constrained based on assumptions or other findings. While the results detail space-based observations of objects in middle-Earth orbit (MEO) and geosynchronous orbit (GEO) from observer's in LEO and MEO, they do not detail the LEO-to-LEO case. The authors propose a method for the correlation or linking of observations based upon the intersection of their AR's. If the AR's for multiple observations intersect then the two objects may be associated or correlated as the same object. This is not a guarantee however; the implication is that the objects may be associated because each observation shares part of its AR with the resultant AR from the other observation. This method can be used for the LEO-based observing case for the possible correlation of LEO-observed objects and their initial orbital elements.

Research presented in [10] deals with the correlation problem via iterating through the AR based upon multiple TSAs. The AR is constrained based on the range and range-rate plane with space-based observations being made from a polar-LEO of objects in MEO and LEO.

The research presented in [11] focuses on the concepts of the AR and an 'attributable' for ground-based optical observations of heliocentric space objects. An attributable is a four-dimensional quantity defined by two or more observations and extraction of meaningful data from a TSA. More simply, an attributable is the resultant data from a TSA in the form of two angles and two angular velocities. For ground-based optical observations the attributable will be in the form of right ascension, declination and their respective angular rates. The information making up the attributable cannot itself give a full orbit solution consisting of six elements. The missing information, range and range-rate, is then defined and represented through the AR. The constraints placed on the AR in [11] are for heliocentric objects and not geocentric objects, so they will differ from constraints placed on the AR in the case of Earth-orbiting space debris.

Identification through the 'linking' aspect of the research is detailed in [12]. The identification of the heliocentric space objects is done through the linking of multiple

TSAs and as a result, multiple attributables. The more attributables that can be achieved for each observed object the higher accuracy the orbital determination process will yield. This research highlights the importance of correlation within the orbit determination process. In studies [11], [12] the authors detail the process of cataloging, linking, and iterating through attributables based on TSA observations, which allows for orbit determination solutions and possible correlation among heliocentric space objects.

In [13] an algorithm is presented for the correlation and orbit determination of LEO objects from ground-based radar and optical measurements. The algorithm presented needs only two observations from different orbital passes, while studies reported in [1], [2], [4], [5] necessitate three observations from different orbital passes. The initial orbit determination process is performed after two attributables are obtained for a given object. The form of the attributable is dependent upon the way the data is taken. For example, radar attributable will yield two angular values, range, and range-rate as the four-dimensional quantity while an optical observation will yield two angular values and their respective angular rates as the four-dimensional quantity. Therefore the unknowns associated with the radar attributable are the angular rates while the unknowns for the optical attributable are the range and range-rate. These unknowns are used as the axis for the AR. The space object population used for these simulations is derived from the European Space Agency's (ESA) MASTER-2005 model. The correlation of objects comes after the orbit determination process via the Least Squares Method (LSM). The author notes that even after the orbit determination process some associations may be false and further linking may be needed with more attributables, and hence more observations. This is the case if two attributable belong to different objects. The orbit determination process for this algorithm in [13] represents preliminary two-body orbits and may possibly account for the J2 perturbation experienced by LEO space objects. A perturbation is the force acting on a satellite that perturbs it away from the nominal, Keplerian, orbit. These perturbations, or variations in the orbital elements, can be classified based on how they affect the Keplerian orbital elements. Two-body, or Keplerian motion, describes the orbital force of a two-body system. In the case of geocentric satellites the two bodies will be the Earth and the satellite or space debris. Third-body perturbations account for either Sun or Moon effects on the geocentric satellite.

2.2.2. Orbit determination for space debris

In [6] the authors address the problem of initial orbit determination with TSA observations specifically for space debris in LEO. They cite the main problem in the orbit determination procedure for Earth-orbiting debris population as being the inability to identify, and separate, sets of data which belong to the same physical object. This is similar to the previously referenced correlation and linkage problem associated with TSAs for all space objects. Thus, a possible method for the identification of debris is proposed via a reduction from a two-dimensional uncertainty to a one-dimensional uncertainty. The authors' theory includes optical observations for debris in high orbits, and radar observations for object in low- and middle-Earth orbits. Different parameters are measured when observations are made optically versus observations made via radar. Of great relevance to the work presented in this dissertation, is the work reported in [6] which constrains the AR, firstly because the object is in a geocentric orbits, and secondly based upon minimum and maximum ranges as wells as the semi-major axis of the observed debris object. These constraints allow for the initial orbit determination process by generating a finite amount of initial condition orbits. The author notes that while orbital parameters can be extracted from radar signals of LEO debris objects, due to the pulse mode operation of many of these radars and the rates at which objects pass through the radar beam, poor orbital data is realized unless correlated follow-up measurements can be made.

The study pertaining to [9] deals with the orbit determination process of high area-to-mass ratio (HAMR) objects in GEO. The focus is placed on the trajectory analysis of these HAMR objects as they are subjected to modeled and un-modeled perturbations and accelerations. Numerous forces are acting on these objects throughout their orbit. These forces, or factors, include solar radiation pressure, thermal emission effects, and the interaction between possible surface electrostatic charging and the weak magnetic field. If these non-conservative forces are mis-modeled, which is usually the case, these perturbations can significantly impact the orbital trajectory making the correlation, linking, and orbit determination of these objects very difficult. These forces can induce errors into the orbit determination process from tens of days for smaller forces and weeks to years for larger non-conservative forces. The results from [9] illustrate the importance of utilizing accurate force models for the simulation of Earth-orbiting objects.

GEO HAMR debris objects are studied for correlation and linking purposes in [14]. The correlation problem is addressed via two algorithms for the linkage of TSAs in the orbit determination process. This process is based on the optical attributable from TSA observations and the definition of orbital elements.

2.3. Space-based angle and angular rate observations

In [15], [16] space-based observations were introduced as a viable means of IOD. This work has been extended through the work of [7], which was briefly mentioned earlier, by attempting to resolve the TSA problem for space-based observations from a low-Earth orbiting sensor platform.

The work most similar to this dissertation is that of [7], where the authors perform initial orbit determination for space-based observation from an observer placed in low-Earth orbit (LEO). Their algorithm is generic in that it does not limit the observer's location, thus allowing for space-based observations, and yields candidate orbits for every pass or, Too Short Arc (TSA). Since a candidate orbit is yielded at every pass, there is no need for multiple TSAs to be correlated. The observing satellite is placed in a polar-LEO circular orbit with a semi-major axis of 760 km, which is very similar to the observer orbit chosen for the research in this dissertation. While the orbital plane is well defined and the errors for inclination are low, it was found that the largest errors were associated with the determination of the semi-major axis and the eccentricity of the orbit. The algorithm showed an increase in accuracy over the classical Laplace, Gaussian, and double-r iteration methods for orbit determination. It is noted however that the observations of the very short arcs need to be performed with a high accuracy sensor.

Of particular interest to this research is the utilization of angle and angular rate data in the IOD process. Taff presented a process for IOD based on single and multiple observations of space objects in middle-Earth orbit (MEO) and Geosynchronous orbit (GEO) through the use of angles and angular rates, [17], [18]. In [17], [18] the observations are not considered to be TSA observations as they are acquiring angles data for 5, 10, 20, and 40 minutes. During the observations the topocentric distance is being calculated. This topocentric distance, the range from observer to satellite, allows for the rapid measurements of angles and the instantaneous angular rates of satellites. No LEO satellites were used in the aforementioned analysis. [18] builds on the findings of [17] by extending the work as to include multiple observations, which consists of the right ascension, declination, and their angular rates.

In [19] the authors presented research dealing with the use of angles and angular rate data for IOD pertaining to GEO objects. Ground-based observations, in the form of 10-minute tracking arcs, are simulated for three different near-GEO objects. Information pertaining to the semi-major axis, range, and geocentric orbit of the object independently act to constrain the AR. For example, the authors state that three angle pairs, right ascension and declination, are needed for the orbit determination process if the orbit is elliptical. However, if the assumption is made that the orbit is circular then only two angle pairs are required.

Other work for IOD with angles-only data has been performed and evaluated in [20]–[23]. In [20] the author extracts range data from ground-based angles only observations for LEO, MEO, and GEO objects. Three algorithms are presented for the initial orbit determination process. The research in [21] is focused on using multiple simulated ground-based and space-based angles only observations for the orbit determination process. The results show that the process is a viable alternative to the classic methods of orbit determination with the benefit of not reaching a trivial solution for the space-based observer case.

Space-based angular measurements are simulated in [22]. Objects are simulated in Keplerian, two-body, orbits. Azimuth and elevation are the space-based angular measurements simulated. Relative orbital elements are represented using spherical coordinates rather than rectilinear coordinates. This spherical coordinate representation for the relative positions allows for full recovery of the relative spacecraft state via the relative hybrid elements. The findings suggest that the relative hybrid elements are fully observable assuming there is time-varying relative motion between the observing and observed spacecraft.

In [23] the author offers an evaluation of Gooding's method for space-based space surveillance measurements. This analysis is based on the Space Based Space Surveillance (SBSS) initiative. Simulated observations were made of MEO and GEO objects from LEO, MEO, and GEO space-based platforms. The author concludes that the best initial orbit determination outcomes had closer initial range estimates, that more observations and continuous observation proved better for each simulated case, and that lower orbits such as LEO allow for greater precision tracking of the observing satellite. The best results occurred when greater relative motion between the observing satellite and the observed space object was present. The author notes that although continuous observation may not be practical, continuous monitoring of the immediate region surrounding a satellite may be of benefit.

The solution proposed in [11], [12] uses the concept of attributable. The attributable is the basis on which the AR can be computed. In [3] the authors present a means of defining and constraining the admissible region based upon the optical attributable as well as the radar attributable, which is more relevant for the study of LEO objects, [6], [11]. Through the use of the optical and radar attributables the author defines their respective admissible regions in the range and range-rate plane, and the right ascension rate and declination rate planes. The admissible region is then constrained based upon assumptions regarding the orbit of the object, the first assumption being that it is geocentric. Many constraints can be placed on the admissible region including, range, eccentricity, semi-major axis, and characterization of the orbital type of the space object from either ground-based or space-based observations, [8], [10]–[12], [19].

2.4. Space debris environmental modeling efforts

Since actual observations are limited by today’s technology it is impossible to detect, track, and characterize the entire Earth-orbiting debris population. Modeling efforts, created and maintained by NASA’s Orbital Debris Program Office, have yielded the EVOLVE, LEGEND, and ORDEM software packages. EVOLVE is used for modeling the long-term orbital debris environment, [24], [25]. LEGEND is a LEO-to-GEO Environment Debris model, which has the ability to represent and faithfully reproduce the historic Earth-orbiting debris environment. LEGEND also has the capability to extrapolate and predict for future debris environment projections. The model covers the near Earth space between 200 km and 40,000 km altitude and outputs debris distributions in one-dimensional (altitude), two-dimensional (altitude, latitude), and three-dimensional (altitude, latitude, longitude) formats, [26]. ORDEM is NASA's Orbital Debris Engineering Model which describes the orbital debris environment in the low Earth orbit region between 200 and 2000 km altitude, [27], [28]. These software packages have been used for explosion, fragmentation, and collision analysis pertaining to space debris, [29]. The Satellite Orbital Debris Characterization Impact Test (SOCIT) was a ground-based hypervelocity impact test against a realistic satellite target performed in order to validate NASA's breakup model, [30]. Complimentary to NASA effort, the European Space Agency's Meteoroid and Space Debris Terrestrial Environment (MASTER) models the spatial distribution and physical properties of Earth-orbiting space objects, [31], [32].

Three studies of interest concerning debris populations and their possible effect on the operational security of spacecraft are [33]–[35]. In [33] the number of warning events, close approaches, and collision avoidance maneuvers are analyzed as a function of orbital altitude for LEO spacecraft. The analysis looks at how many of the spacecraft and rocket bodies in LEO comply with international guidelines such as the 25-year deorbiting policy. They present findings that many spacecraft and rocket bodies in sun-synchronous and geostationary transfer orbits as well as payloads in critical LEO regions, such as 800 km – 1000 km altitude, demonstrate poor compliance with the 25 year deorbiting policy. Only one out of nine spacecraft with masses larger than 50 kg below 1300 km altitude comply with the deorbiting policy. This contributes to over 40 tons of mass annually remaining in space longer than allowed by international guidelines. The study suggests that the most effective way to stabilize the debris environment is the active removal of mass from orbital regions with high spatial densities. These conclusions are in line with the findings of [35]. However, the findings of [34] suggest increased monitoring and tracking capabilities, in contrast to active debris removal, as a more effective way of securing the operational security of spacecraft long-term. The study presented in [34] models and analyzes the space debris population and its growth over the next 30 years for effective methods for a possible reduction in the number of collision avoidance maneuvers performed by satellites.

2.5. Space object characterization efforts

There are three main techniques for the observation, monitoring, and characterization of space debris: radar measurements, optical- or visual-based measurements, and infrared- or thermal- based measurements. These observation technologies aid in the initial orbit determination process, conjunction or collision analysis, and in the space object characterization effort.

2.5.1. Radar-based techniques

Radar-based techniques have been used by the US SSN as well as many other laboratories and observatories around the world. Radar techniques have been classically limited to the analysis of space object in LEO due to the power necessary to get a return signal.

The Tracking and Imaging Radar System (TIRA) in Germany has been used for debris sensing purposes for debris in LEO, [36]–[38]. The radar limitation for size determination is dependent upon the size of the radar resolution cells versus the size of the measured object; the observed object must be at least ten times the size of the cells, [36]. The TIRA systems is capable of two-dimensional radar imaging using inverse synthetic aperture radar (ISAR) along with range profiles, [38]. Through the consecutive series of radar images, analysis into the rotation rate and rotation direction of satellites can be carried out. The research shows that this imaging technique can be used for resolved-image analysis of malfunctioning satellites for failure attribution.

In [39] the authors present an algorithm utilizing ISAR images for the high-resolution three-dimension imaging of rotating debris. The drawback of ISAR is that it is not capable of imaging objects which are smaller than the range resolution of the radar system. An alternative, single range Doppler interferometry (SRDI), was proposed which allows for the imaging of space debris of sizes smaller than that of the range resolution of the radar, [40]. This method utilizes the fact the space debris is usually subject to simple spin and rotational motion around its major axis. The SRDI method is applied to a sparse signal reconstruction problem with the goal of imaging space debris of 1 – 10 cm, [41]. Radar-based ISAR and SRDI techniques are able to yield resolved images of Earth-orbiting objects. ISAR efforts have resulted in the further characterization of satellites, and other orbiting space objects, through the analysis of consecutive resolved images. Many radar techniques are used for initial orbit determination, however some systems may be focused on perigee estimation, in which case the characterization effort only considers the rapid discernment between satellites and ballistic missiles, [42].

2.5.2. Optical observations

Optical observations of space debris constitute the most widespread and studied effort geared towards debris characterization. The Air Force Maui Optical and Supercomputing

(AMOS) detachment on Maui has three systems which can be used for optical and thermal imaging of debris, [43]–[45].

The author of [43] gives an overview of the LEO and GEO debris observing capabilities at AMOS and NASA. At AMOS there is the 3.67 m Advanced Electro Optical System (AEOS) telescope, which contains an adaptive optics system, for the imaging of LEO debris, anomalous events, and breakups. NASA has the Liquid Mirror Telescope (LMT) for optical studies of LEO debris down to 3 cm. NASA also operates the Charged Coupled Device (CCD) Debris Telescope (CDT), which is used for GEO observations.

For the ground-based optical observation of GEO objects the Rapid Action Telescopes for Transient Object (TAROT) facility in France offers a fully automated process for detection and correlation of both satellites and debris. In studies [46], [47] the author presents an algorithm for the real-time detection of GEO objects with near-zero false detection rate and non-detection rates. In [47] the algorithm presented allows for real-time orbit determination of GEO objects.

The Astronomical Institute of the University of Bern (AIUB) operates a 1-m telescope for the analysis of higher area-to-mass ratio (HAMR) objects in geostationary (GEO) and geostationary-transfer orbits (GTO) on behalf of the ESA, [48], [49]. In [48] optical observations, through the analysis of light curves, from the AIUB 1 m telescope are used for the initial orbit determination process which secures orbits for the area-to-mass determination. Many of these HAMR object observations in GEO, which range from 1 kg/m^2 to more than 40 kg/m^2, point to pieces of foils used in multilayer insulations of spacecraft as possible candidate objects. In [49] the efforts of the AIUB 1 m telescope are set toward the build-up of a small-debris catalog via photometry and light curves for the shape and attitude state of the GEO HAMR objects. [50]–[54] have utilized ground-based optical observations for characterization of LEO debris objects. The Ground-based Electro-Optical Deep Space Surveillance (GEODSS) telescope is used for the determination of debris albedo in [50]. The albedo of an object must be determined for the conversion of visual brightness to physical size. Infrared and optical measurements are used for the debris albedo determination, which ranges from 0.02 – 0.50 with a median of 0.14. These findings conclude that debris albedo is less than that of intact satellites because the debris has undergone a darkening effect due to their genesis in fragmentation and breakup events.

A wavelet-based analysis for the characterization of the Okean-3 LEO satellite using ground-based multi-band optical observations is proposed in [51]. The observations of unresolved resident space objects (RSO) were collected at the Magdalena Ridge Observatory using the Multi Lens Array camera coupled to the 2.4-m telescope. Characterization is performed in terms of satellite body motion estimation and surface materials analysis.

Simulated photometric data is used for material type determination in [52]. The author outlines an approach using filter photometry and orbit determination for estimation of material type. Once the material type is estimated the albedo can be determined along with additional information, which can then aid in the estimation of object shape.

Methods presented in [53], [54] involved detection, shape, and motion estimation of LEO debris objects. In [54] a Cosmos 2082 rocket body is analyzed via light curves from optical telescope observations to determine shape, rotational axis, rotation period, precession radius, precession period, and a composition parameter.

The concept of space-based optical telescopes launched into LEO, GEO, and GTO orbits for initial orbit determination, surveillance, and characterization of GEO space objects is covered in [55]–[57]. In [55] the authors propose a space-based 15 cm aperture telescope in a GTO for the observation of uncontrolled GEO objects. The proposed sensor has the capabilities to observe debris down to 1 cm in size with the purpose of the instrument being the observation of the debris population below 10 cm. An alternative space-based optical (SBO) telescope is proposed in [57]. The SBO payload was requested and designed to provide statistical information pertaining to the number of objects and size distribution of the space debris population in the GEO region of space.

2.5.3. IR and thermal techniques

Infrared, thermal, and multi-band observations of space debris aid in the material and temperature determination of the characterization effort. Early ground-based observations in the long-wave infrared (LWIR) were performed of GEO satellites in [58]. Sixty tracks were observed of 20 GEO satellites. The equilibrium temperature of these satellites was as expected, 270K – 380K, which corresponds to blackbody temperature flux curves with a maximum intensity between 8 – 13 µm, according to Plank's Law for Blackbody Radiation. The observations were taken with an N-band astronomical filter. LWIR measurements were taken of the satellites entering and exiting Earth shadow. It was found that payloads that included solar panels, such as the GE-5000 series satellites, display more variation in their radiant intensity with respect to phase angle when compared to static spin-stabilized cylinders such as the Boeing-376 series satellite.

The Broadband Array Spectro-graph System (BASS) sensor on the Advanced Electro Optical System (AEOS) telescope at AMOS has been used for the observation of GEO HAMR objects, [59], [60]. The BASS sensor is considered to be a mid-wave infrared (MWIR) device as it is sensitive in the 3 – 13 μm waveband of the spectrum. Observations were made, roughly 17 minutes in duration, of GEO HAMR objects. Results include the temperature, emissivity-to-area product, and their associated errors, [59]. These thermal and material properties affect the solar radiation pressure incident upon the object and therefore aid in more accurate force modeling and orbit prediction. In [60] the IR measurements are coupled with CCD measurements which allow for the characterization of space objects through the determination of temperature, materials, and orientation dynamics.

Space- and ground-based methods for the thermal imaging of space debris utilizing existing technologies is presented in [61], while [62] analyzes the parameter uncertainties associated with radiometric data. In [61] analytical modeling techniques are used for consideration of scenarios for the thermal imaging of space debris; of those scenarios a space-based thermal sensing payload is considered. [62] presents a method for analyzing the uncertainty in parameters obtained from radiometry-based characterization techniques. The goal of the study was to provide a model-based estimation approach to quantify the value of specific data types for satellite characterization efforts.

The Infrared Astronomical Satellite (IRAS) was launched in 1983 with a multi-band sensor to perform an all-sky survey in the infrared part of the spectrum, [63]. The IRAS payload was placed in a sun-synchronous polar low-Earth orbit at an altitude of 800 km. The IRAS detectors consisted of four wavebands centered at 12, 25, 60, and 100 μm. Characterization efforts using data from the IRAS mission could determine emissivity, absorptivity, temperature, and physical size of satellites and RSOs. The IRAS satellite was able to make position and radiometric observations of RSOs and many deep space satellites which allowed for correlation between observations and existing satellite catalogs. The IRAS mission was followed-up over two-and-half decades later with the Wide-field Infrared Survey Explorer (WISE) mission, [64]. The WISE payload contained four detectors centered at 3.4, 4.6, 12 and 22 μm wavelengths. Both satellites were placed in LEO sun-synchronous orbits for the observation of LEO, MEO, GEO and deep space objects. In [65] a space-based infrared sensing platform is proposed for the study of heliocentric near-Earth objects as mid-infrared observations have proven to be most effective for size determination.

[44], [45] utilize optical and infrared observation for characterization of space debris. In [44] characterization techniques for small spacecraft are presented and include semi-major axis determination, size, mass, and albedo estimation. The proposed characterization methods include analysis of photometry, radiometry, and spectroscopy for the characterization of small satellites and debris. [45] presents two methods for the determination of satellite surface properties from temporal sequences of whole-body, multi-band brightness measurements.

3. ASTROMETRIC MODELING

Rapid orbital characterization of local area space objects utilizing image-differencing techniques

Satellites have limited awareness of nearby objects that might pose a collision hazard. Small, relatively inexpensive on-board optical local area sensors have been proposed as a means of providing additional awareness. However, such sensors often have limited performance. Proposed are methods to increase the Local Area Awareness provided by such sensors by means of classical and novel image processing techniques. The local area of the sensor platform is defined, for our purposes, as a sphere of radius 500 km surrounding the sensor platform, or observing satellite. This analysis utilizes image differencing-based techniques, in the development of a detection algorithm and proposes a novel object-velocity classifier. This classifier may provide a means of rapidly distinguishing local area objects that pose a possible collision hazard when an orbital two-line element set is not available.

Derivation of a novel classifier is based on the speed of the projected object moving across the focal plane array of the detector. This technique relies on the assumption that detection from the sensor platform allows for tracking over all times the object if it is within the local area of the sensor platform. This alternative to intensity-based, signal-to-noise ratio detection is performed by exploiting the stellar background as a reference from a space-based observing satellite. Results presented in this chapter further demonstrate the ability of the proposed classifier to provide means for rapidly distinguishing objects that pose a possible hazard within the local area of the sensor platform. These preliminary results act to substantiate this claim and therefore lay out a pathway for relevant and meaningful future work in the area of Local Area Awareness for satellites.

3.1. Introduction

The most updated and reliable catalog for space debris is the United States Space Surveillance Network (US SSN). The SSN consists of an aggregate of optical and radar sites strategically placed around the world. The size of objects that are routinely trackable from ground-based systems is limited. Objects at Low Earth Orbit (LEO) may be able to be tracked if they are greater than 10cm, while objects at Geosynchronous Earth Orbit (GEO) are only routinely tracked if they are greater than 1m in size [66]. Tracking of these objects has paid off in recent years. In 2009, nine debris collision-avoidance maneuvers were performed by satellites under NASA'a controls, and over thirty-two reported collision avoidance maneuvers were performed between February 2009 and 2010, with one maneuver performed by China [67], [68].

Collision avoidance with both debris and spacecraft has become a priority since February of 2009. On February 10, 2009, a non-active Russian satellite collided with a United States privately owned telecommunications satellite 500 miles above Siberia [69]. This collision occurred at LEO orbit where tracking of objects is performed more routinely relative to objects at GEO orbit. The 24 hour orbital period of geostationary orbit offers significant advantages for certain applications, including communications, imaging, weather monitoring, etc. While debris is less of an issue at geostationary orbits, these satellites are extremely expensive and difficult to replace in a timely manner. For this reason, this research first looks at geostationary orbits; subsequent work will look at collision hazards at LEO. For the purposes of this dissertation, local area is defined as a sphere of radius 500 km centered on the sensing platform or observing satellite. Only objects that pass within the observing satellite's local area are considered.

The work by Tombasco [70] introduced a method for updating GEO elements using ground-based and space-based angles only data thereby improving GEO orbit determination and estimation. The research goes further and demonstrates improvement in the estimation of inter-satellite range as viewing times move from one hour towards twelve hours. Our research efforts differ in that we do not intend to perform orbit estimation or range determination; instead the efforts of this research are aimed at more rapidly discriminating between local area objects that may pose collision hazards and those which do not.

Many detection methods and algorithms that may be applicable to LEO and GEO based local area sensing have been developed. Bayes multi-frame detection and tracking [71] was proposed in order to extract target from clutter and interference. In work presented in [72] all candidates objects within an image were tracked, and then based on their trajectory and decision conditions, false targets are removed and real targets of interest are extracted. Work has also been done utilizing star-point target detection from Earth-based tracking systems in which detection and tracking are performed using inter-frame image differences with cluttered background removal via adaptive thresholding [73]. Early work on inter-frame difference method for identification of sources in low SNR environments among noisy backgrounds is presented in [74]. Much of the previous work cited is aimed at terrestrial-based detection and tracking of targets, with targets including near-Earth-objects (NEO) as well as other cosmological bodies of interest. This effort applies image difference based algorithms for detection and tracking in a local-area space environment.

3.2. Methods

This section will describe the methods and software that were utilized for this research. An overview of the method for this research is illustrated in Figure 3.1. The block diagram in Figure1 is configured to have three distinct parts: inputs, model assumptions, and analysis. The approach taken, as illustrated in Figure 3.1, remains independent of any sensing technology or sensor specifications so long as all model assumptions are achieved. In this way, this research aims for a generalized approach as it does not necessitate, or be constrained to, any particular technology. This will be discussed more in depth in the following sections. This method presents results in terms of pixel-speed analysis. This analysis is based on a continuous application of image-registration and image differencing that will be described in detail later in this chapter.

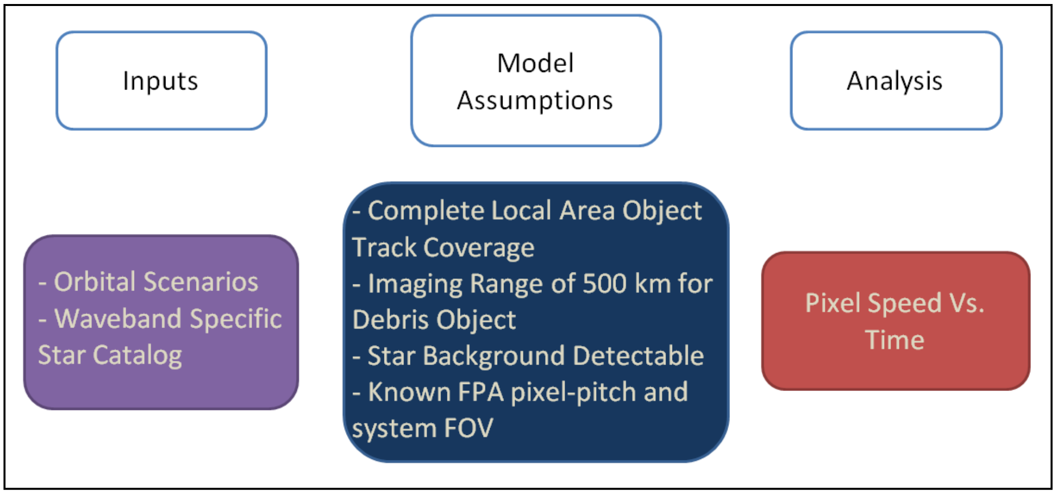

Figure 3.1: Astrometric Modeling and Structure of the Methodology

3.2.1. Inputs

The orbital information of the sensing platform and the debris objects are entered into the Satellite Orbit Analysis Program (SOAP). The data resulting from SOAP provide the position and velocity information of the debris relative to the sensor platform as a function of time. The initial orbits that were simulated for the preliminary results presented in this chapter are as listed in Table 3.1.

Table 3.1: Orbital dynamics scenarios used for simulations

Row	Altitude Difference [km]	Starting Altitude Relative to Observing Satellite	Orbital Type	Eccentricity
1	100	Above	Circular	0
2	100	Below	Circular	0
3	Varying	Above	Non-Circular	.0012

All orbits are in-plane with the sensor platform and the Earth's equator. Two of the orbits are circular. One is located 100km below the sensing platform (i.e. between the earth and

GEO); one is located 100 km above the sensing platform (beyond GEO). As these orbits do not cross the GEO belt, they do not pose a collision hazard with the sensor platform. The third case describes a slightly elliptical orbit, with an eccentricity of .0012, which does cross GEO and is phased in such a way as to collide with the sensor platform. Therefore it will have a “Varying” altitude difference relative to the sensing platform In all cases, the initial phasing of the orbits in the simulation was such that the debris was initially just outside the local area, and therefore not detected by the sensor. As the simulation progressed, the debris entered the local area and was sensed by the camera.

The simulation was run for 24 hours in the case of the circular orbits and 12 hours in the case of elliptical orbit. The simulation is run in the early summertime, when the sun is inclined north of the Earth's equator. The orbital data provided by SOAP was imported into MATLAB along with a star catalog. The star catalog used should be representative of the waveband and sensitivity of the sensing technology selected. As an example, the Hawaii IR Parallax Program star catalog shown in Figure 3.2 is a measure of the magnitude of stars in the infrared waveband. While this research is not aimed at any specific waveband, the star catalog that is used should be described in the same waveband as that of the sensing technology.

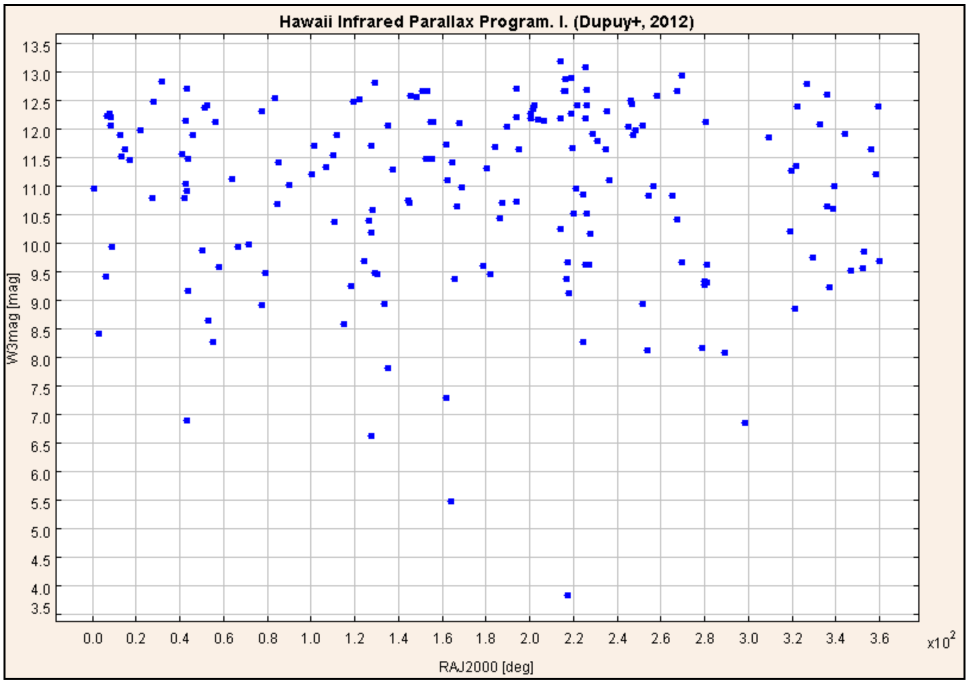

Figure 3.2: Example star catalog: Hawaii Infrared Parallax Program star catalog

3.2.2. Model Assumptions

The image processing analysis proposed in this chapter does not necessitate the complete description of the detector and its specifications. In seeking a solution to this problem, the configuration of the sensor platform must meet four assumptions. The first assumption is made regarding the placement and orientation of the sensor on the spacecraft and its field-of-view. Second, while gaps in coverage may be deemed acceptable in a final system design, this model was constructed so that the entire orbital track of the debris object could be viewed with no coverage gaps. Third, background objects were not included in the simulations; the configuration of the sensor(s) was such that complete spherical coverage was achieved. Fourth, that the sensor technology was configured to provide an unresolved signal of the debris object only when the debris was within the local area of the sensor platform (i.e. a range of 500 km or less). The approach taken relies on a star background being recorded by the sensor. Therefore, it is assumed that there are stars of sufficient magnitude in the simulation to provide a reference for the image differencing technique. In those situations where the star background is not available, an alternative means of detecting and registering the object must be employed or this method will not be applicable. This situation may occur when the sensitivity of the sensor is not sufficient or when the stars are occluded by the sun, moon or earth. While the detailed sensor description is not necessary, it is assumed that the field-of-view (FOV) and pixel pitch of the focal plane array (FPA) are known.

It is worth noting that at this point in the research the problem of detection while the object or debris contains the Earth in the background has not yet been considered. The model assumption states that the object should be completely tracked through the local area of the sensing platform. If the object is tracked by the sensing platform for long enough without moving to within the angular subtend of the Earth, then the analysis can still be performed. This is the case for the "Below" orbital simulation case.

3.2.3. Analysis

This chapter will detail the Pixel Speed vs. Time output in the analysis section of Figure 3.1 shown earlier. Since the specifications of the imaging system would be known, such as pixel-pitch and FOV, as well as the period of orbit for the sensing platform or observing satellite, we can therefore deduce the rate at which the stellar point sources move across the FPA of the detector. Using this determined static rate of positional change of the projected sources across the FPA, we can detect other objects with varying levels of confidence by the difference between their rate of change as projected across the

FPA and the known rate of the stellar background. This analysis goes further and plots these detections as a function of object position as projected on the FPA versus time. With positional data as a function of time, we can then derive the velocity or pixel-speed data as a function of time. This technique is used and a classifier is proposed to provide a means of rapidly distinguishing objects that pose a possible collision or interference hazard within the local area of the sensor platform.

3.3. Results

The simulation output is a string of successive detections as a function of time for which the observed local area object is in view of the sensing platform. This process is illustrated in Figure 3.3 for the "100 km Below" case presented previously in Table 3.2.

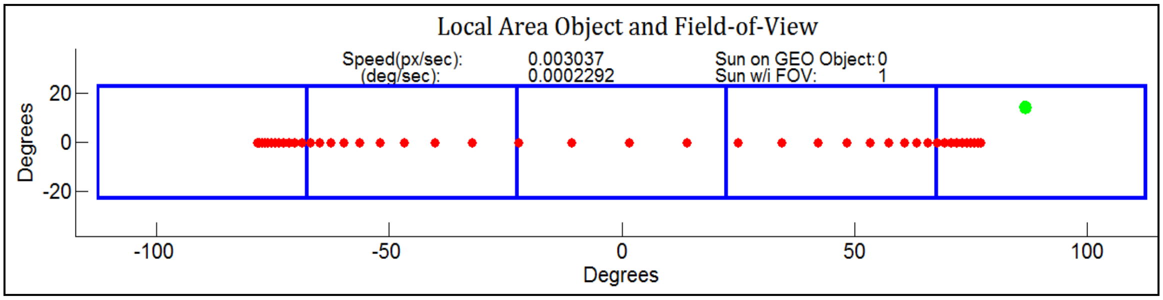

Figure 3.3: Object position and FOV: successive detections of the Local Area object

The blue rectangles in this figure represent sensors oriented in such a way that they achieve perfect sensor hand-off. This means that once the observed object leaves one sensor's FOV, it is immediately picked up by an adjacent sensor. The red indicator represents the projected position of the local area object on the FPA of the detector. Each red indicator is plotted at a fixed time interval. The difference in distance from one red indicator to the next is proportional to the object-velocity in the horizontal direction as projected onto the FPA. The green circle that moves through the plots during the simulations represents the position of the Sun. The signal due to the Sun may be important if the local area object and the Sun fall onto the same pixels on the FPA. This "Sun" term would be accounted for in a noise model and will no longer be discussed in this chapter.

3.3.1. Image-Differencing for Detection

As seen earlier in Figure 3.3, the simulation yields the projected position of the local area object across the FPA as a function of time. This data is plotted in Figure 3.4, with the x-axis representing time in seconds, and the y-axis representing the horizontal object location as projected upon the FPA in terms of degrees.

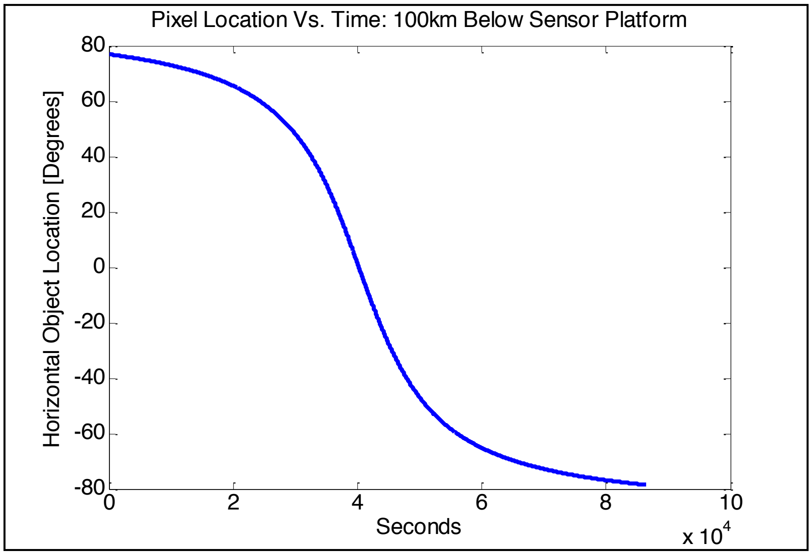

Figure 3.4: Local Area object angular track of Local Area object over 24-hour period

With the projected horizontal object location of the imaged local area object known, a curve can be fit using polynomial regression. The resultant curve is smooth and a derivative can be calculated, yielding the pixel-speed, or angular-speed, of the observed local area object as a function of time. The pixel-speed for the "100 km Below" case as well as the other two cases is shown in Figure 3.5.

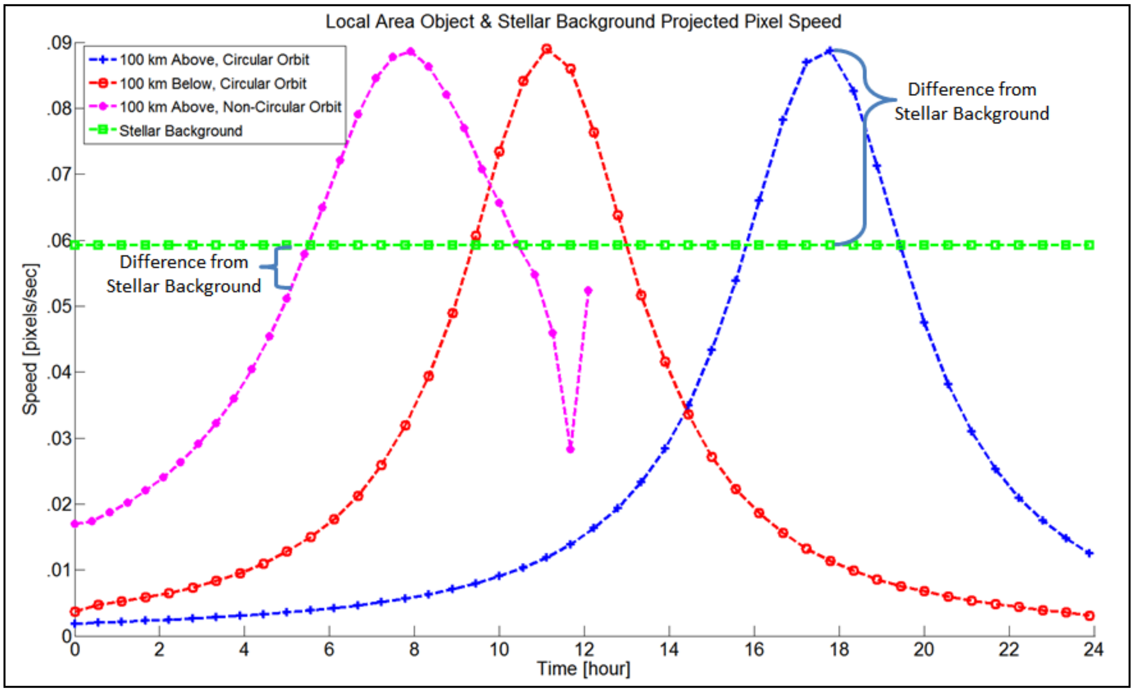

Figure 3.5: Composite Local Area object angular-speed data: all simulated orbits

From these results, it can be seen that the local area object moves at a dynamic range of speeds across the FPA compared to the static and determined rate of the stellar background. All three orbits have pixel speeds curves that cross the stellar background rate multiple times. At the instance the pixel speed of the object is equal to the approximate pixel speed of the stellar background, detection using this technique is not feasible. However, Figure 3.5 shows that the pixel speeds of the local area object for different orbits are not similar to the pixel speed of the stellar background for a substantial amount of time, especially early on in the simulation. This demonstrates the use of this image-differencing approach for detection given there is a stellar background or other means of realizing precise registration between subsequent images for reference. Qualitative analysis shows that the greater the difference from pixel speed curve of the object to the static rate of the stellar background, the better chance it has of being detected. Therefore, this analysis leads to a sort of confidence rating upon detection.

3.3.2. Pixel-Speed Orbital Characterization Classifier

The final results presented in this chapter deal with the angular-speed curves presented in Figure 3.5. While the determination of pixel-speed curves for each of the local area object orbits demonstrates the feasibility for a space-based detection method using the stellar background as a reference, it also sets the stage for a novel classifier for local area orbital characterization. Figure 3.6 shows the result of centering the pixel-speed curves on their max value and windowing for a 12 hour time window. Both of the non-approaching circular orbits follow very similar curves, however the non-circular orbit's pixel speed curves varies drastically from the two circular orbits and is therefore separated and characterized as such very early on in the simulation process.

It should be noted even though the results presented in Figure 3.6 are in terms of pixels per second, the process itself is not sensor technology dependent. As mentioned previously, it is assumed that the FOV and pixel-pitch are known. These parameters may change for different technologies, sensors, and optical configurations. However, the dynamics of the projected pixel speed curve, or angular rate, will remain constant with only the scale of the y-axis changing so long as the object can be seen throughout the local area of the sensor platform.

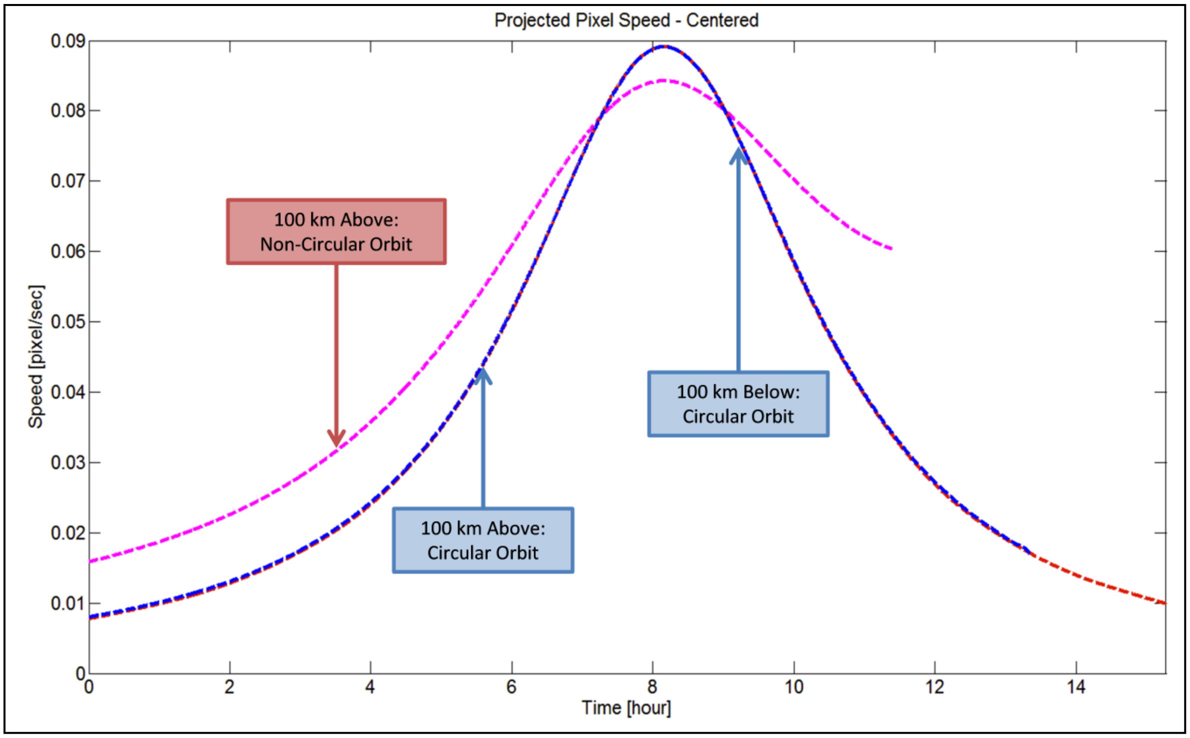

Figure 3.6: Composite Local Area object angular-speed data: angular-speed data for all simulated orbits - centered

3.4. Conclusion

The results presented in Figure 3.6 demonstrate the ability of the pixel-speed classifier to characterize the orbits of local area geostationary objects. The results presented in this chapter further demonstrate the potential of the proposed classifier to provide a means of rapidly distinguishing objects that pose a possible collision hazard within the local area of the sensor platform or observing satellite. Given that the proposed classification technique is dependent upon fitting a point to curve on the pixel speed graph, this process can theoretically be performed relatively quickly. It is only limited by the time it takes the object to move from one pixel to another on the FPA. This again will be dependent on the imaging system characteristics, the orbital dynamics of the object, and the sensor platform.

The results presented substantiate the claims made regarding an alternative to intensity-based detection of local area geostationary objects. Figure 3.5 showed that by utilizing image-differencing techniques, local area objects can be detected as they are imaged from a space-based geostationary sensor platform. This type of alternative detection method may prove to be useful when intensity-based detection techniques fail. This may occur when the signal-to-noise ratio of the object is low due to any number of factors including the space environment and the imaging system. The demonstration of detection via a passive space-based sensing platform is performed as a "means-to-an-end" so that the aforementioned orbital classification process can take place.

This research was performed using GEO and near-GEO orbits. This was done in order to better understand the dynamics associated with approaching objects in a slow-moving environment relative to LEO obits. The next phase of this research is to continue the analysis of what information can be extracted from unresolved image data at LEO where debris and collision avoidance is a significantly higher priority. This will allow for more orbital simulations to further validate the orbital characterization classifier and establish the means of providing a confidence metric. Detection and tracking algorithms can be developed utilizing the methods and processes laid out in this work.

4. RADIOMETRIC MODELING

Sensor model for space-based local area sensing of debris

A model is proposed to evaluate the capabilities of various LWIR sensors and combinations of sensors to provide Local Area Awareness for satellites in low-Earth and geostationary orbit. The system performance of LWIR detectors mounted at various locations on the satellite is evaluated against multiple observation scenarios with multiple debris configurations. LWIR sensors have been chosen as the detector technology for the initial phase of research because of their ability to operate with the sun in their field of view (FOV) while imaging nearby debris in the long-wave infrared band without the need for additive components such as baffles or solar occluders.

Preliminary results demonstrate the modeling of debris and its LWIR signature for each simulated orbital path. Results are presented in terms of radiant flux of the tracked debris. Radiant flux results are shown for all times the observed debris can be seen by the observing satellite or sensor platform. These results are evaluated for each face, or side, of the observed debris, as well as a composite of all faces. It is shown that intensity-based detection and characterization techniques may be quantified from this research, based on the different emissivities and temperatures of certain space debris materials. The results presented in this Chapter are of simulated debris in the local are of a GEO based sensing platform.

4.1. Introduction

The problems of space debris and collisions related to space debris have become more predominant in recent years. As of launches through December 2012, there are over 3000 known and registered satellites orbiting the Earth according to NASA estimates. This number is up over ten percent from two years prior and is due to more nations having access to space with military and commercial interests and the benefits that are offered with certain orbits. This trend towards more satellites in Earth-orbit is believed to grow even faster in coming years with more countries vying to become space-faring nations. Algeria, Brazil, Chile, Egypt, India, Iran, Malaysia, Nigeria, North Korea, South Africa, and Thailand have all placed a priority on space utilization, [75].

One method of increasing LAA is through the use of on-board optical sensors. Optical sensors come in many different configurations and wavebands; which is optimal depends on how the sensors interact with the specific scenario chosen and the characteristics of the background noise. While any final solution will likely utilize a combination of sensor types, is the focus here is placed on a long-wave infrared (LWIR) based approach. A generalized model, as shown in Figure 4.1, can be used to evaluate the system performance of LWIR sensors mounted at various locations on the satellite against multiple observation scenarios.

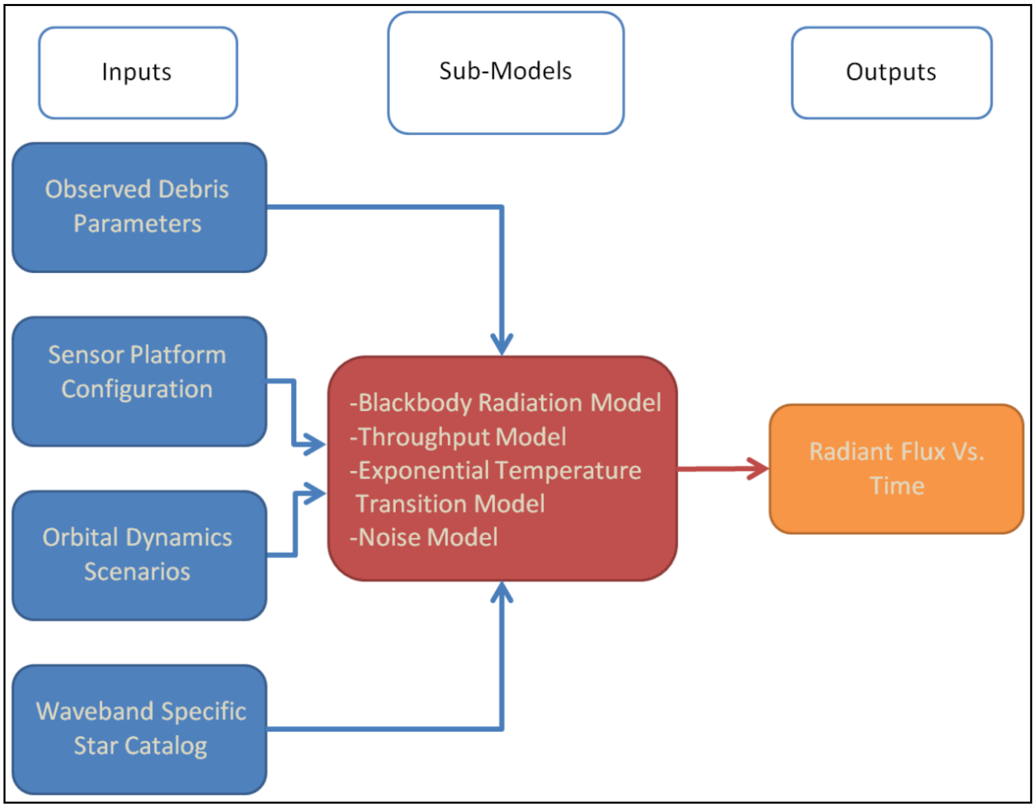

Figure 4.1: Model overview: proposed generalized model

Equation 4.1 shows Wien's Displacement Law, [76], according to which the peak radiation emitted by blackbodies with temperatures ranging from approximately 100-400 K corresponds to the LWIR waveband of 7-30 µm. We will initially limit ourselves to a detector waveband of 7-14 µm, which corresponds to a temperature range of 200-400K.

$$\lambda_m = \frac{2898}{T} \qquad [\mu m] \qquad (4.1)$$

4.2. Methods

Once the model is completed, a significant aspect of the research will be to show the feasibility of different sensors, sensor configurations, sensor placements, and sensor orientations. With this in mind, it is necessary to assemble a generalized model for all aspects of the research that are being considered. In this way, we have configured the model to have three distinct parts; inputs, sub-models, and outputs as shown earlier in Figure 4.1.

4.2.1. Inputs

The inputs component of our model is comprised of four sets of information. The first input deals with the properties of observed debris that are relevant to calculating the signal seen by the observing satellite or sensing platform sensors. The observed debris that we chose to simulate for this research is a cuboid type piece of hollow debris. This input can be changed to characterize many different configurations. Each side of the cube is defined as having materials and/or components, with each having a temperature range, active area, and emissivity. The temperature range is based on thermal equilibrium temperature that debris materials will reach due to heating from the Sun and from radiative heat exchange in deep space. The lower bound on the temperature ranges is the thermal equilibrium that will be reached by the materials radiating heat to the 77K space environment of geostationary orbit; the upper bound represents heat exchange with the sun. Because of heat transfer between the various sides of the debris and the thermal mass of the material, it is anticipated the actual temperature of each side will vary within this range according to the particular configuration and composition of the debris.

The parameters for the initial simulations reported in this chapter are shown in Table 4.1 and Table 4.2. The area and the temperature ranges selected for each side of the cuboid are listed in Table 4.1. Table 4.2 highlights the different material configurations that were chosen for these simulations. Both Roughened Aluminum and Graphite were applied to all sides of the debris and separate simulations for all orbits were run for both debris materials. The model can handle temperature and wavelength dependent emissivity when the data is available. All emissivity values pertaining to our simulation are chosen from online databases for the emissivities of certain materials and are approximations over the LWIR spectrum [77], [78].

Table 4.1: Rigid body construction of observed debris parameters

Side	Area $[m^2]$	Temperature [K]
Front (Earth-facing)	1	[305 – 325]
Back	1	[305 – 325]
Left	.1	[305 – 325]
Right	.1	[305 – 325]
North	.1	[305 – 325]
South	1	[305 – 325]

Table 4.2: Material properties of observed debris parameters in LWIR waveband

Material	Emissivity
Roughened Aluminum	.1
Graphite	.76

The second input component is the Sensor Platform Configuration that is located on our observing satellite. This is where the sensor is chosen and parameters are given concerning the Field-of-View (FOV), number of pixels on the Focal Plane Array (FPA), pixel pitch, as well as the placement, orientation, and number of sensors to be mounted.

In order to fully consider the implications of relative orbital dynamics and the effect of background objects on the measured signal, the model was configured assuming a 360 degree, gap-free coverage along the equatorial plane. For 45 degree FOV sensors, this requires eight sensors to be mounted around the body of the spacecraft. At this juncture in the development of the model, sensors have not been placed to observed orbital motion that is not in the equatorial plane. To account for this, we have chosen orbits that have no inclination relative to our sensing platform. As a result, the “North” and “South” faces of the debris will be out-of-plane with our sensors, thus never being seen and not contributing to any derived signal. In subsequent work, sensors and orbits including differing inclinations will be included in the analysis. Once it is understood how to most efficiently extract the needed information from this gap-free sensor configuration, means of minimizing the number of sensors required to obtain this information can then be explored.

The third input component of the model is the orbital dynamics scenarios that dictate the motion of the observed debris. These simulations will deal with two types of orbits, which are classified as near-geostationary circular and near geostationary non-circular. The circular tracks are those in which the observed debris will be in a circular orbit at an altitude difference of 100 km both above and below the sensor platform; the non-circular orbit will encompass orbital tracks that are “Varying” in their altitude difference relative to the sensing platform due to an elliptical orbit. The non-circular orbit, which will be referred to as “Above non-circular” from here on, will start at an orbital altitude of 100 km higher/above the sensor platform and migrate into an orbit at the same altitude as the sensor platform, posing a possible collision hazard. For all these orbital dynamics scenarios, the attitude state for the observed debris will be Earth-facing, where one face is oriented toward the Earth at all times. More random states of motion will be included in the future. A list of all orbital scenarios that were simulated is shown in Table 4.3.

Table 4.3: Orbital dynamics scenarios used for simulations

Row	Altitude Difference [km]	Starting Altitude Relative to Observing Satellite	Orbital Type	Eccentricity
1	100	Above	Circular	0
2	100	Below	Circular	0
3	Varying	Above	Non-Circular	.0012

The fourth and final input component to our model is a waveband specific star catalog to provide sensor registration. The IR star catalog is derived from the Strasbourg Astronomical Data Center [79]. The IR star catalog is comprised of point source catalogs that have been merged and configured to yield a radiant flux in the LWIR band for each point source. The current implementation of the IR star catalog remains incomplete and is recommended as future work.

4.2.2. Sub-Models

Contained within the model are sub-models which are used to characterize physical aspects of the system. The most fundamental part of our research is the sub-model defining the light propagation, or our blackbody radiation sub-model. This defined model considers the four input components of our system: the Observed Debris Parameters, the Sensor Platform Configuration, the Orbital Dynamic Scenarios, and the waveband Specific Star Catalog.

All objects that have a temperature other than 0 K are continuously emitting and absorbing radiation. The radiation characteristics of an ideal blackbody are fully specified if the temperature of the body is known. A perfect blackbody has an emissivity, ε, equal to one. In this research we will be observing greybodies, which are defined as having $\varepsilon <$

1. Emissivity of certain materials can be both wavelength and/or temperature dependent. The model incorporates temperature dependent emissivities for certain materials, when such data is available. The power spectral density curve of a greybody has the same shape of that of an ideal blackbody; however at any wavelength, λ, it has a value that bears the ratio of ε to that of an idea blackbody [76]. The blackbody radiation sub-model is based on Planck's equation, Equation 4.2, and yields radiance, $L(\lambda)$, at any given wavelength λ. We then integrate Planck's over a desired waveband to yield spectral radiance, as defined in Equation 4.3.

$$L(\lambda, T) = \frac{2hc^2}{\lambda^5}\frac{1}{e^{\frac{hc}{\lambda kT}}-1} \qquad [\frac{\mathrm{Watts}}{m^2\ m\ sr}] \tag{4.2}$$

$$L = \int_{\lambda_1}^{\lambda_2} L(\lambda, T)d\lambda \qquad [\frac{\mathrm{Watts}}{m^2\ sr}] \tag{4.3}$$

The Throughput sub-model calculates the signal measured by the sensor. The visibility of the debris itself is due to the orbital dynamics scenarios and is dependent upon whether or not the debris is within the FOV of the sensor. We also have to account for the visibility due to the sides or components of the observed debris that are not perpendicular to the sensor. This results in a cosine projection of the debris on our image axis and the received signal is affected proportionally. The last aspect of the visibility sub-model is dependent on the range. This relationship is commonly termed the "inverse-squared law." This law characterizes the irradiance of a point source on a surface as being inversely proportional to the square of the distance from the point source [76], [80]. All aspects of the visibility sub-model are illustrated in Figure 4.2, and incorporated into the "throughput" term ϒ, as expressed in Equation 4.4.

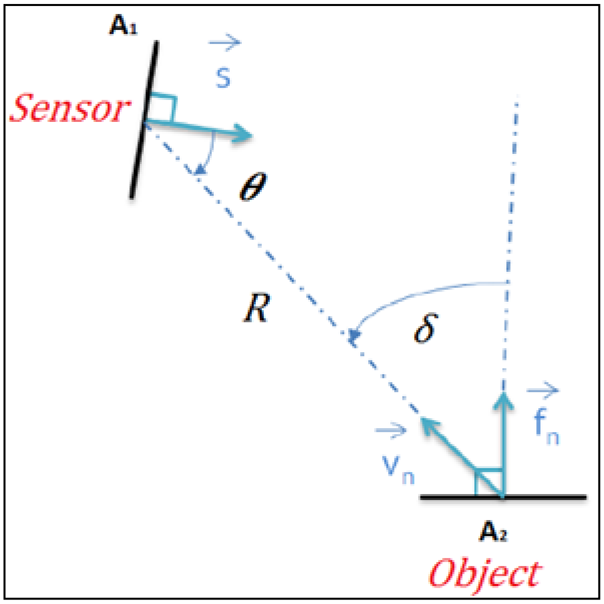

Figure 4.2: Overview of ‘throughput’ model

Note that the first cosine dependent term is set to unity due to the properties of the system’s lenses.

$$\Upsilon = \frac{(A_1 * \cos\theta)(A_2 * \cos\delta)}{R^2} \qquad [\mathrm{m}^2\ \mathrm{sr}] \tag{4.4}$$

The three preceding Equations, 4.2 through 4.4, incorporating Planck’s Law and Throughput, combine to yield our desired signal, Φ, in radiant flux or Watts. This is shown in Equation 4.5.

$$\Phi = L * \Upsilon = \left[\frac{\mathrm{Watts}}{\mathrm{m}^2\ \mathrm{sr}}\right] * [\mathrm{m}^2\ \mathrm{sr}] = [\mathrm{Watts}] \tag{4.5}$$

The next sub-model is the exponential temperature transition model. This sub-model aims to approximate the fashion in which different debris materials will heat up and cool down based on the radiative heating effects of the Sun and internal heat conduction. The rates at which certain materials and components heat up and cool down are dependent upon their thermal and conductive properties. At this point in the research the thermal and conductive properties of the materials have not been modeled and arbitrary limits for the upper and lower bounds have been set as 305K and 325K. Exponential growth and decay curves are used to model the temperature transitions of the materials throughout the simulation relative to the position of the sun for each face of the debris. These transitions are modeled according to the Equation 4.6.

$$T_{growth} = 305 * e^{0.0008*t} \ ; \ T_{decay} = 325 * e^{-0.0008*t} \tag{4.6}$$

There are constraints placed on the upper and lower temperature limits of the object due to its radiative equilibrium temperature. A logistic model for growth that incorporates these constraints would be more appropriate. For the current work, a first-order approximation is assumed with the exponential growth and decay functions as expressed in Equation 4.6, with the outputs bounded to 305K – 325K. For the given equations the objects will both heat and cool to its equilibrium in less than two minutes. As the actual thermal characteristics of the materials are modeled and more representative equilibrium temperature constraints are studied they will be added to the model accordingly.

A true sensor evaluation tool must include a model of all of the sources of noise so a SNR can be calculated. Such a tool should also consider the impact of background objects (such as the signature of the earth, moon, stars, and sun) on the sensor performance.

4.2.3. Outputs

The model described above considers radiant flux for its output and analysis. This analysis will be intensity-based and is a function of the radiant flux incident on the detector as a function of time. Once a noise model has been incorporated, this output will be presented as SNR as a function of time. This will allow for further evaluation of when (and to what extent) the observed debris is detectable by the sensor. This will log in units of Watts all instances in which the observed debris is within the FOV of any sensor .

4.3. LWIR Sensors

Mercury Cadmium Telluride (MCT) and bolometers are two types of commercially available LWIR sensors. In the context of uncooled infrared imaging technologies, the term “infrared bolometer” usually refers to resistive micro-bolometers in which the temperature increase is measured by a resistance change [81]. Micro-bolometers are durable, robust, and commercial available through multiple vendors. While cooling the sensor below ambient temperature significantly reduces the noise floor, bolometers are still considerably noisier than their LWIR photonic counterparts, such as MCT detectors. MCT detectors achieve superior performance as the absorption of the photon results not in heat, but in an electronic excitation. However, MCT detectors are often operated at well-below ambient temperatures (<100K) in order to reduce noise. This requires more involved cooling schemes. This noise will significantly impact the range at which an object can be detected and tracked. Since this is a report on the developmental stages of modeling the self-emissive radiation of debris, we will not choose any specific detector technology for our analysis. Instead the focus will be on the LWIR signature, or received radiant flux, of space debris within the LWIR waveband. The received radiant flux of an object onto a detector,Φ, is a function of its pixel pitch, for our purposes we will choose an arbitrary pixel pitch along with other imaging system characteristics such as FOV.

Once noise models are incorporated, specific LWIR detector technologies can be evaluated.

For our initial study a 640x640 pixel detector with a 45°x45° FOV, 30μm pixel pitch, and spectral range of 7 – 14 μm has been chosen. With these characteristics, each pixel will subtend a solid angle of 0.0703125 degrees or 253.125 arc seconds in the vertical and horizontal directions. The specifications of the arbitrary LWIR sensor that was modeled for an initial sensor platform configuration are shown in Table 4.4.

Table 4.4: Arbitrary LWIR sensor specifications

Field-of-View	Pixel Pitch	Spectral Range
45° x 45°	30μm	7 – 14 μm

4.4. Results

In this section simulation results are graphically displayed. This is not an exhaustive representation of all the simulations that were run, however the results shown will be adequate for the reader to understand and identify trends and relationships in the data.

Three orbital dynamics scenarios have been simulated, as provided in Table 4.3. For rows 1 and 2, the corresponding "Altitude Difference" value represents the altitude difference when the debris is closest to the observing satellite. For row 3, the corresponding "Altitude Difference" value represents the initial difference in orbital altitude between the observed debris and the sensor platform for the "Above non-circular" simulation.

An overview of the simulated orbits is shown in Figure 4.3. For the "Below" scenario there will be a time when the debris and the Earth may be projected on the same pixels on the FPA. Future work will need to address background objects to ensure accurate detection and tracking of the debris in these types of situations; which are considered beyond the scope of this dissertation.

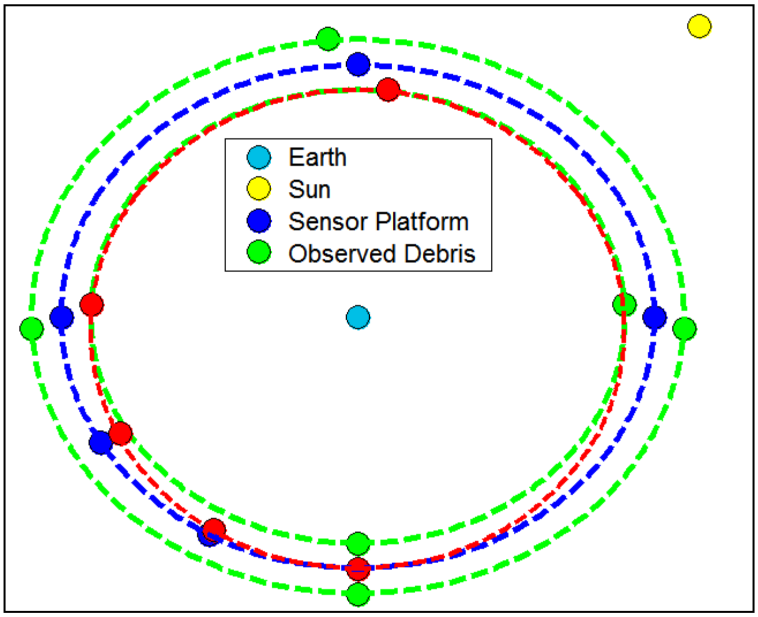

Figure 4.3: Overlay of simulated orbits relative to GEO orbit

Figure 4 illustrates the received radiant flux signal due to each side, or face, of the debris that was observed in the 100 km above sensor platform scenario for an Earth-facing attitude state. In this case the four in-plane and the two out-of-plane sides of the debris were analyzed.

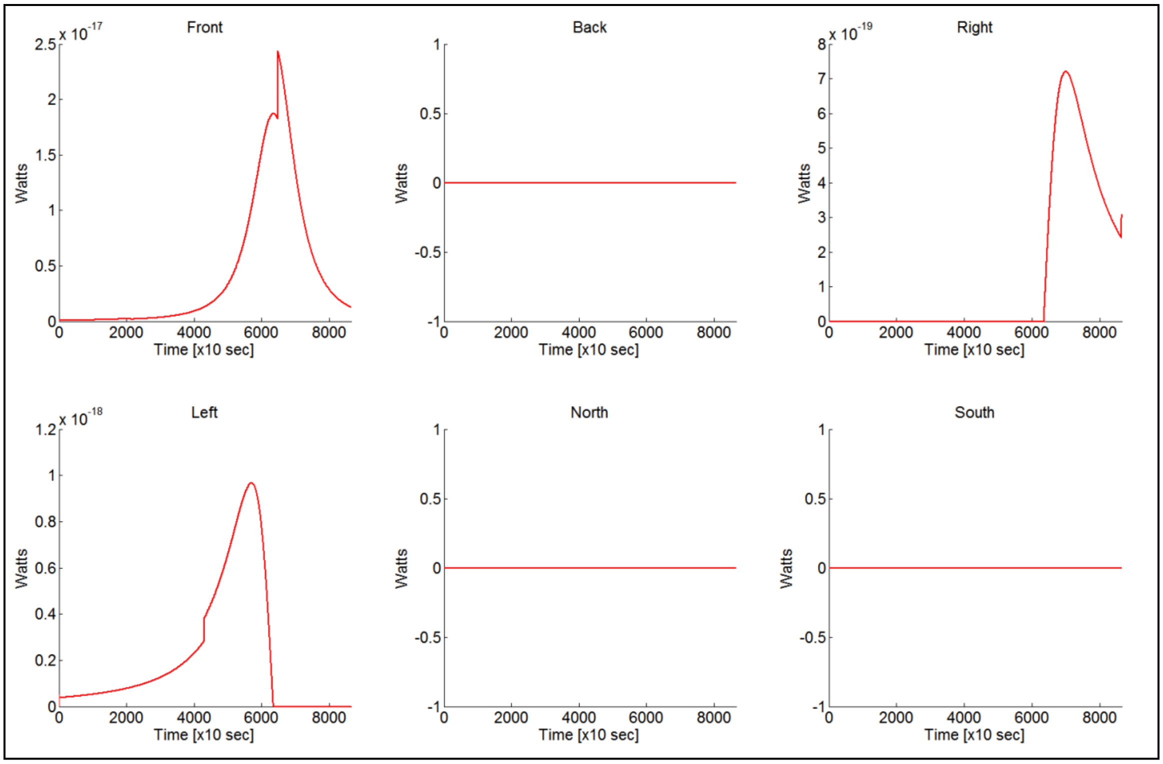

Figure 4.4: Radiant flux signal of individual facets: circular orbit 100 km above scenario: graphite debris

From these of outcomes, simple checks can be performed to ensure that the results make intuitive sense. In this particular scenario, the observed debris' "Back", will always be facing away from the Earth and will never be seen by the sensor platform. The "Left" and "Right" faces will rotate towards the sensor platform over the course of the 24 hour orbit, but the sensor platform will never be able to see both the "Left" and "Right" faces at the same time. The same is true for the "Front" and "Back" faces as well as for the "North" and "South" faces.

The sensor itself will not be able to differentiate to which face a signal will be attributed to; it will only realize the entire composite signal which is due to the summation in time of all faces. The face-by-face signal analysis in Figure 4 helps the reader assess the physical and orbital aspects of what is happening in each simulation. This is done with the expectation of developing analysis tools that can be utilized on the aggregate signal, namely the Composite Radiant Flux signal as shown in Figures 4.5, 4.6, and 4.7 as a function of time. The blue line represents the range of the debris relative to the sensor platform; however this is not shown to scale and is meant to only give the reader an intuitive understanding of the physics and orbital dynamics involved. The solid red line represents the received radiant flux as a function of time for the graphite debris, while the dashed red line represents the received radiant flux as a function of time for the roughened aluminum debris. Both debris were subjected to the same orbital dynamics scenarios under separate simulations and are overlaid to highlight the differences in received signal magnitude from one piece of debris to the next.

It can be observed that the received radiant flux for the roughened aluminum and the graphite debris cases yield similar curves at different scales. This is because the debris objects share the same orbital dynamics, temperature ranges, temperature transitions, and rigid body configuration for each simulation with only their respective emissivity differing. It can also be observed that there exist fast transitions, or so-called hick-ups, in the data that are shared by both debris objects. These fast transitions are due to the temperature transitions of the sides of the debris that is being observed by the sensing platform, as well as sides rotating in and out of view of the sensor platform.

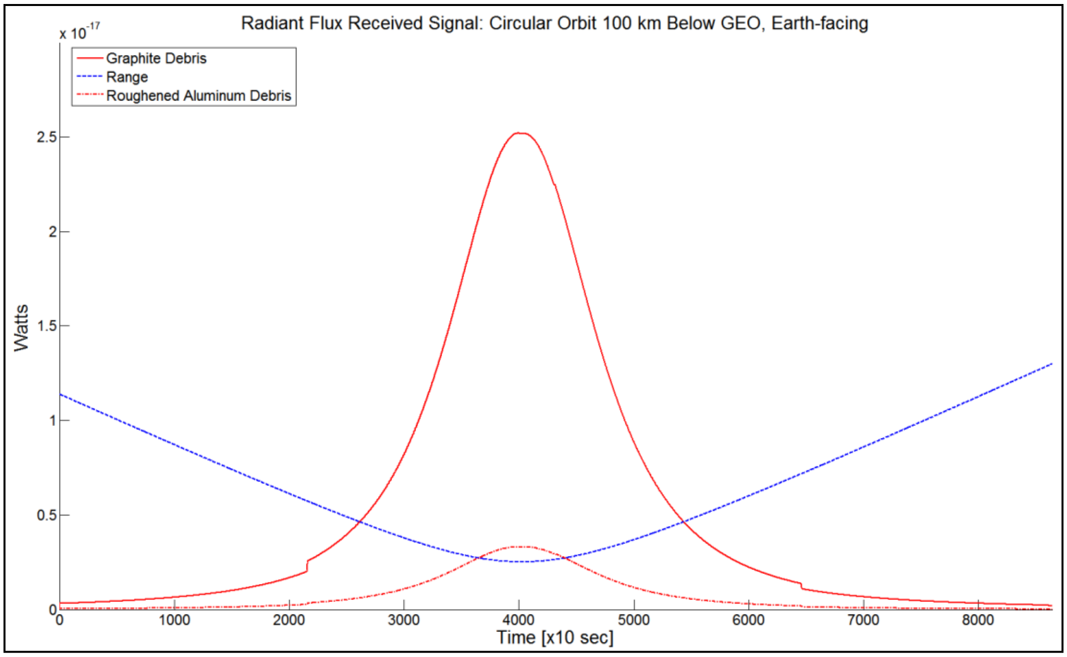

Figure 4.5: Composite radiant flux signal: circular orbit 100 km below GEO scenario

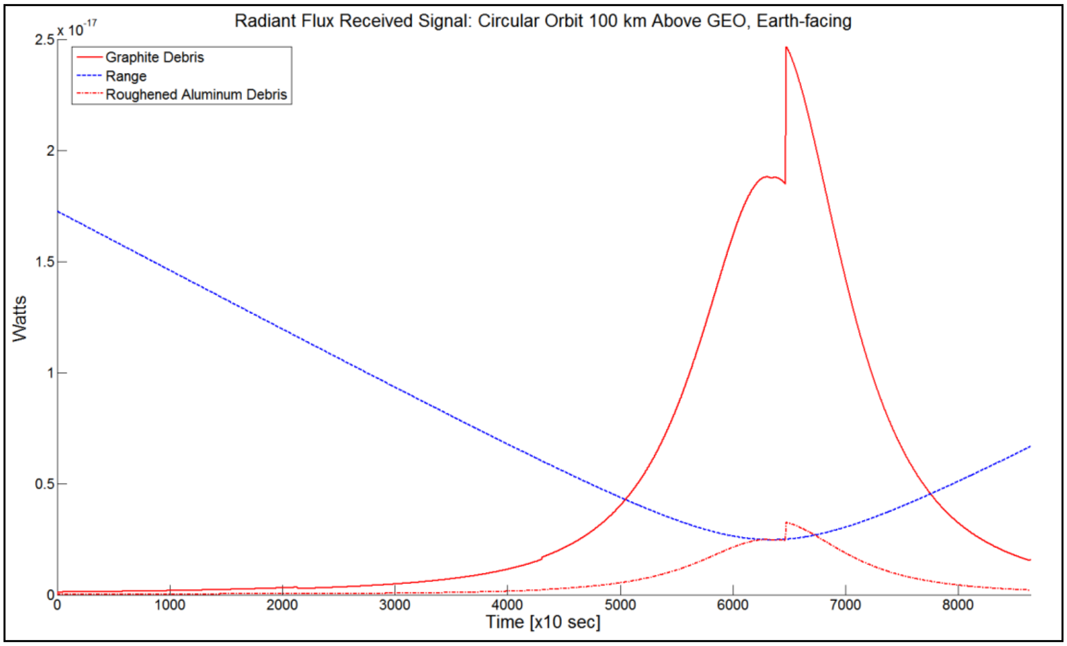

Figure 4.6: Composite radiant flux signal: circular orbit 100 km above GEO scenario

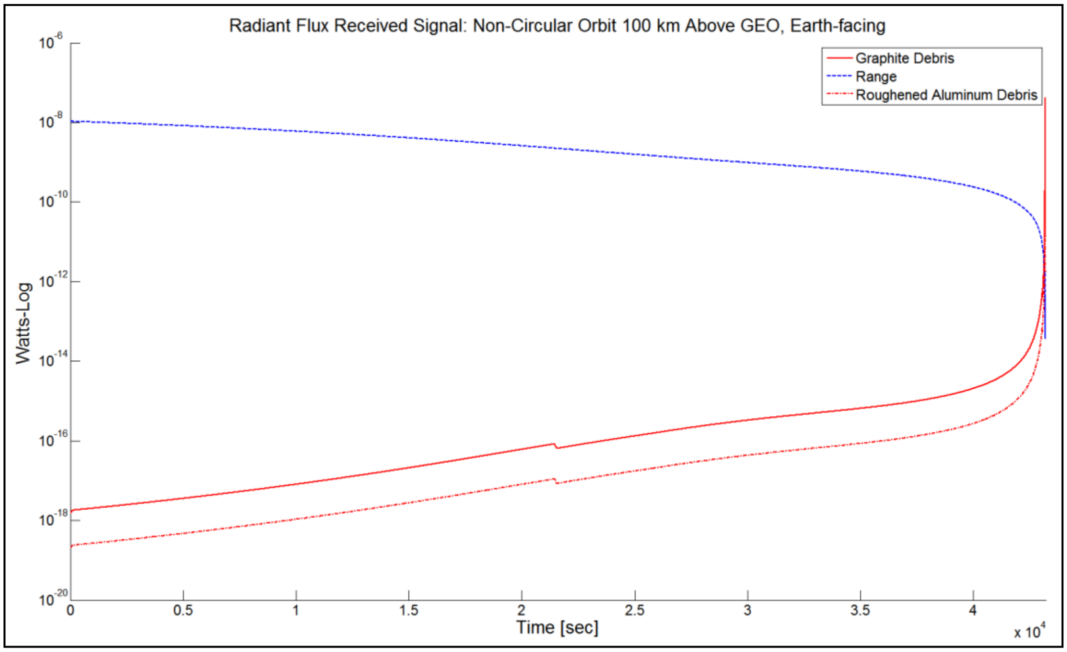

Figure 4.7: Composite radiant flux signal: above non-circular orbit 100 km above GEO scenario

Radiant flux analysis has applications for observed debris detection and observed debris characterization. However, there is other information about the observed debris' orbit that we would like to explore. In Figure 4.7 it can be seen that the signal experiences a significant increase when the Above non-circular orbit case is approaching its closest range. As the observed debris gets closer, the distance between the sensing platform and the observed debris decreases, resulting in a dramatic increase in the received signal. This is due to the signal being inversely proportional to the square of the range between the sensor and the imaged object. This happens to be beneficial in terms of detection; however it is desired to have indications of an approaching piece of debris as early as possible.

4.5. Conclusions

All simulations were run with a sensor platform in geostationary orbit. This was done with the goal of understanding how temperature transitions, differing material emissivities, and attitude states of debris contribute to the received radiant flux on an arbitrary detector on a very slow time scale (twenty-four hours at geostationary orbit). This knowledge will then be applied via LWIR radiant and reflective modeling of debris at LEO from a space-based platform. The goal will be to develop an imaging system with an adequate sensor for the characterization of various types of debris in LEO, where space debris is a more serious current and future concern. This chapter is aimed at detailing the developmental stages of this process with the simulation of debris LWIR signatures as viewed from a space-based sensor platform.

A model is considered to evaluate what information could be derived from unresolved image data regarding debris in geostationary and near-geostationary orbits as observed from a geostationary sensing platform. This model, albeit in its early structure, is created with sufficient flexibility for future variations in configurations of sensors, sensing platform, differing orbital scenarios, and differing observed debris configurations. Sub-models are defined for the physical aspects of the modeling.

Since the model is to be used to perform an application based sensor trade study, future work will fully and quantitatively describe the noise in terms of the detector technology as well as qualities inherent to the imaging system. When this is performed all results will be in terms of signal-to-noise ratio (SNR). Additional future work will focus on performing more simulations with varying orbits, more observed debris configurations, updating the thermal properties of materials, and initial solar configurations. From these analyses recommendations for the design of a realistic sensor will be made. The model will be further developed and applied to debris in LEO orbit, where Earthshine (thermal radiation emitted from the earth) becomes a primary illumination source during solar eclipse conditions.

5. THERMAL MODELING

Thermal modeling of space debris via Finite Element Analysis

The characterization of debris objects through means of passive imaging techniques would allow for further studies into the origination, specifications, and future trajectory of debris objects. The long-wave infrared waveband is a potential candidate for the observation of space debris. However, in order to simulate and study the radiance of these objects on long-wave infrared detectors, assumptions have to be made regarding the properties of the object, which determines both the temperature and the amount of LWIR radiation reflected by the object. The purpose of this investigation is to study the steady-state radiative thermal equilibrium temperature, temperature transients, and object temperature as a function of time, for varying cuboid-type space debris objects; reflectance properties are the subject of another study. Conclusions are made regarding the aforementioned thermal analysis as a function of debris orbit, geometry, orientation with respect to time, and material properties.

5.1. Introduction

The characterization of space debris is important because an understanding of the structure, mass, and material properties may help researchers to further extract needed information regarding the orbit and origination of such debris. To this end the broad scope of this research is focused on the Long-wave Infrared (LWIR) signatures of space debris. In order to calculate and model the LWIR signatures of such debris in orbits between low-Earth orbit and geosynchronous orbit, a representative and accurate thermal model must be developed.

The thermal analysis described here takes into account the specific orbit, size, orientation, rigid body structure, and material properties of simulated debris. Approximations for the rigid bodies of space debris are comprised of cuboids, cylinder, plates, and rocket bodies. The steady-state section of this analysis calculates the radiative equilibrium temperatures of debris due to the radiation emitted by the Sun as well radiation emitted by the Earth.

In the area of space debris research there exists data regarding the temperatures of debris in orbit with respect to time [50]. However, previous studies have not been completely exhaustive or robust as to allow for modeling of a wide variety of debris objects. As each face of the debris object will be receiving heat flux at a different rate during orbit, the problem cannot be simplified to a one- or two-dimensional analysis. Determining the three-dimensional thermal profile of the debris while considering the effects of received radiant flux, radiation from the debris out to space, and conduction of heat through the debris material in all three dimensions results in a set of partial differential equations with respect to three variables that cannot be solved analytically but can be approximated using the method of Finite Element Analysis (FEA). Finite element analysis will be used further for the transient analysis, adding specific material specifications such as conduction and emission properties, in order to approximate the thermal transients of debris. Such transient scenarios would occur where debris passes through eclipse due to its orbit, which is representative of much of the debris in low-Earth orbit.

5.2. Methods

There are two main components inherent to the thermal modeling described in this chapter: 1) the definition and calculation of the radiance profiles and 2) the insertion of this data into the Finite Element Analysis software package in SolidWorks.

5.2.1. Radiance Profiles

The derivation of the radiance profile that is experienced by the orbiting debris object is a function of the debris orbit, geometry, orientation with respect to time, and material properties. The normalized vectors from the debris object to the Earth and the Sun are calculated for all points along the debris object's orbital path. The debris object is then given a three-dimensional geometry, or rigid body structure, along with a specified tumble rate and tumble direction. Once the geometry of the debris object and the orientation of the debris solid body relative to the local coordinate system are known, the normalized vectors for all sides of the debris object can be determined. Assumptions are made regarding the size, distance, and radiating temperature of the Earth and Sun. With a known range, angular subtends, and radiating temperature, the radiant flux density incident upon the point in space which the debris object occupies along its orbital track can be calculated. The normalized vectors for all sides of the debris object, their orientation relative to that of the Earth and Sun, and the irradiance due to the Earth and Sun on a specific point in three-dimensional space where the debris object is located are all known. Therefore, the projected area receiving radiation and the amount of radiative energy the projected area is receiving, from the Sun and/or Earth can be determined for all sides as a function of time for all points along the orbital path of the debris object.

The first step in the calculation of the radiance profiles is to determine the vectors stemming from the center of the debris object and pointing towards the Sun and the Earth. These vectors are determined relative to an Earth-centered coordinate system. The vectors are calculated in 10-second increments for one entire orbital period. Contained within the vectors is the range from the object to the Sun and to the Earth. The vectors data can be created in MATLAB [82] or exported from simulation scenarios modeled in Systems Tool Kit 10 (STK 10) [83].

After the Earth and Sun vectors have been calculated, the debris object is given a three-dimensional solid body representation, a tumble direction, and accompanying tumble rate. For the simulations contained in this chapter, the debris object three-dimensional solid body is constrained to a cuboid structure of varying size and mass. The cross-sectional areas, construction, tumble directions, and tumble rates used to specify the debris objects to be simulated are described in Table 5.1. The orbital characteristics of the simulated debris object are shown in Table 5.2.

Table 5.1: Geometric and tumble constraints used for simulation

Side Area [cm]	Debris Construction	Tumble Direction	Tumble Rate [rpm]
10	Solid	Spin about Nadir axis	0.01
17	Hollow		0.1
			1

Table 5.2: Debris object orbital characteristics

Orbital Type	Semi-major Axis	Eccentricity	Inclination	Orbital Period [min]	Propagator
Circular - Prograde	7278.14 km	0	98°	102.9	J2

The tumble rate and tumble direction are specified with a yaw and pitch angular offset relative to the local coordinate frame. These specifications establish the initial conditions for the orientation of the front face of the orbital debris. Once the orientation of the front face is established, the normalized vectors for each face, or side, of the debris can be determined since the object is of a cuboid geometry. Assumptions regarding the distance, size, and radiating temperature of the Earth and Sun are made. These values are shown in Table 5.3.

Table 5.3: Earth and Sun constants used for simulations

Temperature – Sun [K]	Temperature – Earth [K]	Radius of Earth [km]	Earth Albedo	Astronomical Unit [km]	Solar Constant [W/m^2]
5778	254	6,371	0.306	149,597,871	1368

Typically, the Sun is assumed to operate as a point source in regard to the Earth-centered orbits that are simulated in this research. Equation 5.1 represents the radiant flux density due to the Sun at Earth-orbit [76]. The distance to the Sun remains relatively constant and is set to 1 AU. This is expressed as the parameter '*D*' in Equation 5.1.

$$SC = \frac{4\pi * R_{Sun}^2 * \sigma * T_{Sun}^4}{4\pi * D^2} \qquad \left[\frac{\text{Watts}}{\text{m}^2}\right] \tag{5.1}$$

The distance from the Earth-orbiting debris object can be dynamic and is determined with the extracted vectors data from STK 10. Due to the relative proximity of the Earth to the debris object, the Earth cannot be assumed to operate as a point source. Instead the Earth is modeled as an extended area source, and as such, the amount of the Earth's surface that will radiate energy to the debris object is dependent upon the height of the object above the surface of the Earth. This relationship is demonstrated through the Earth depression angle, α_e, expressed in Equation 5.2 where the 'r' represents the radius of the Earth and 'x' represents the orbital altitude of the debris object above the Earth's surface [76].

$$\alpha_{\mathrm{e}} = \cos^{-1}\left(\frac{r}{r+x}\right) \qquad \left[\frac{\mathrm{Watts}}{\mathrm{m}^2}\right] \tag{5.2}$$

Figure 5.1 below demonstrates the relationship between Earth depression angle and subtended field-of-view as a function of orbital altitude above Earth's surface. As the distance between the Earth's surface and the object decreases, the amount of surface area of the Earth which radiates energy to the object will also decrease. As a result the amount of radiated energy from the Earth to the debris object will not simply be a function of range and temperature of the Earth but will include the amount of the Earth's surface area re-radiating energy to the object as well.

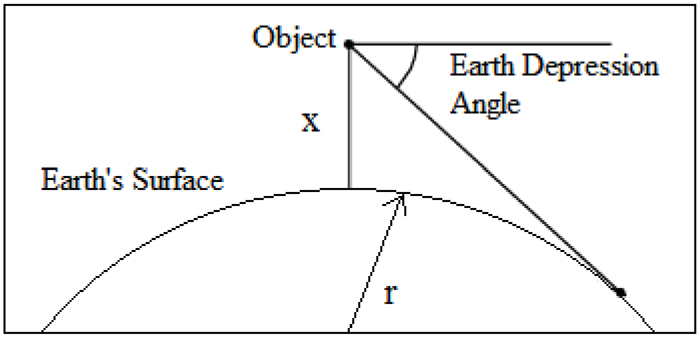

Figure 5.1: Earth depression angle

The surface of the Earth is modeled as a composite of eight quarter-spheres. A quarter-sphere is shown in Figure 5.2 and is constructed by dividing a hemi-sphere into four equal parts. The quarter-sphere is comprised of an aggregate of Lambertian radiators [80]. Each radiator has a given surface area representing the emitting area of that region of the Earth's surface and the radiating temperature as indicated earlier in Table 5.3. Once the quarter-sphere is modeled, the distance from the debris object to each radiator and the angle between each radiator normal vector and the debris object are calculated. The irradiance from the Earth to any point in space can be calculated using Equation 5.3 and is expressed in Watts per meter squared [76]. The 'A_{rad}' parameter in Equation 5.3 represents the projected surface area of the Earth which is radiating energy to the debris object according to the Earth depression angle.

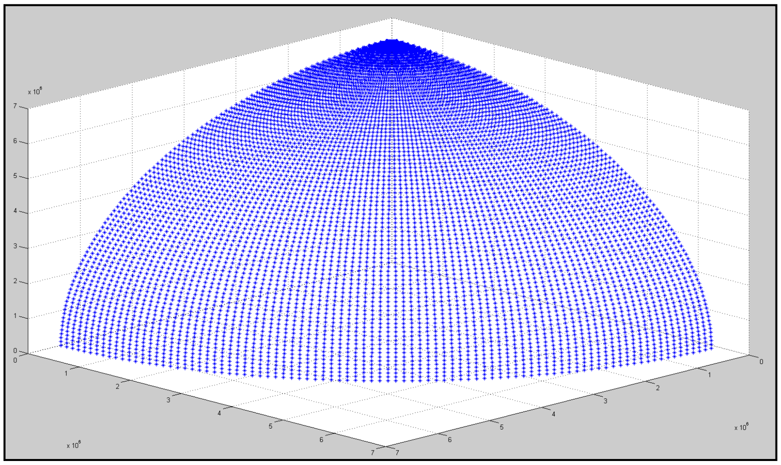

Figure 5.2: Earth quarter-sphere

$$I_{Earth} = (1 - a_{earth}) * \frac{A_{rad} * \sigma * T_{earth}^4}{2\pi * D^2} \qquad \left[\frac{\text{Watts}}{\text{m}^2}\right] \tag{5.3}$$

Equations 5.1 and 5.3 represent the irradiance at a point in space due to the Sun and Earth. However, this is not equivalent to the radiant flux experienced by the orbital debris occupying that point in space. The radiant flux incident upon the orbital debris will depend upon the attitude of the object as a function of time along the orbital path of the debris object. The received radiant flux for each side of the debris object is determined by calculating the dot product of the normal vector from each face of the debris object with the Earth and Sun vectors. The resultant dot product is used as the projected area of each face of the debris object that is receiving radiation from the Sun and/or the Earth. The radiant flux profiles for every side of the object can be determined utilizing the calculated radiant flux densities from the Earth and Sun on the object using Equations 5.1 and 5.3 and the projected area of the debris object that is receiving radiation from the Sun and the Earth. The total radiant flux incident on each face of the debris object is expressed in Equation 5.4 [76]. The '$\cos\gamma$' and '$\cos\delta$' terms represent the dot product calculation of the normal vector for each face with the vectors from the debris object to the Earth and the Sun, respectively. The total radiant flux on each face 'Φ_{Total}' is expressed in Watts.

$$\Phi_{Total} = I_{Earth} * \cos\gamma + SC * \cos\delta \quad \text{[Watts]} \tag{5.4}$$

5.2.2. Finite Element Analysis

A detailed summary covering the finite element analysis of the thermal simulations is found in Appendix A. These simulations were performed in a joint publication, [84], and are included for convenience to account for a complete understanding of the thermal modeling process.

5.3. Results

The results provided in this chapter are focused on analyzing the dependency of certain orbital debris specifications such as size, material, geometry, tumble rate, and thermal properties on the temperature profile of the debris object with respect to time for three faces (Mission, Anti-Mission, and North) of the debris object. An example is shown in

Figure 5.3 illustrating the temperature of three faces of an object for fixed material specifications and debris geometry with differing tumble rates.

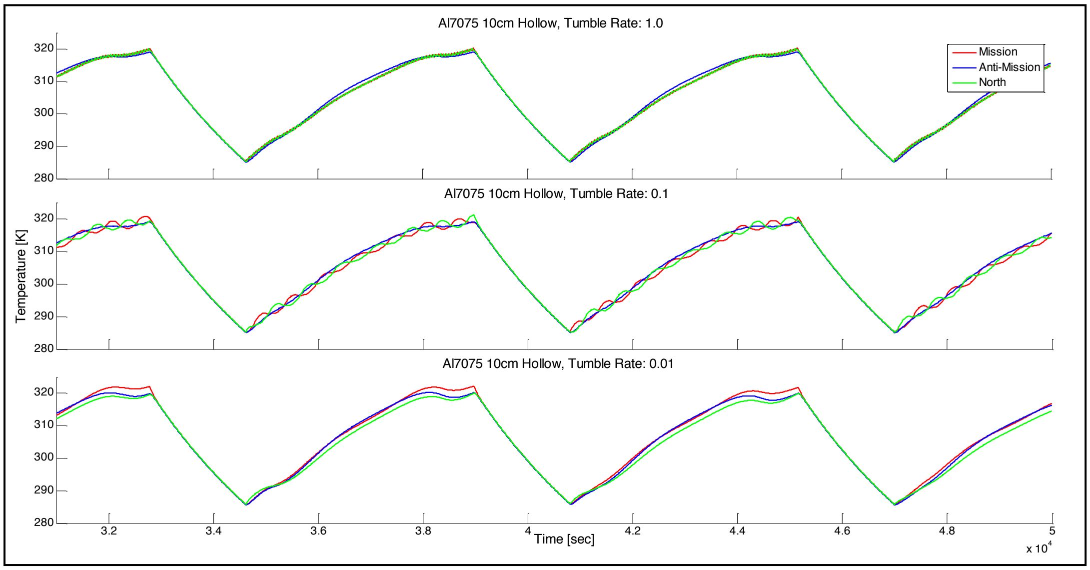

Figure 5.3: Temperature profiles versus time for multiple faces and tumble rates

From simulations, Figure 5.4 shows that the radiative thermal equilibrium (RTE) temperature is minimally dependent upon the size and mass of an object. It also shows steady-state simulations for Al-7075 and titanium, along with two purely theoretical materials: Al-7075 with the specific heat of titanium, and Al-7075 with the conductivity of titanium. Analysis of the ‘Al-075’ case shows that for all debris geometries simulated, the difference in RTE is less than 1K. For the ’Titanium’ case the difference between maximum and minimum RTE for debris geometries simulated is less than 3K. The RTE profiles for the debris geometries are notably different for the two hypothetical materials. The ‘Al7075_cpTI’ case, Al-7075 with the specific heat of titanium, yields the same RTE values for the 10 cm solid and the 17 cm hollow debris geometries; however there is a 1.5K increase in the RTE of the least-massive debris object, the 10 cm hollow case. The

‘AL7075_kTi’ case, Al-7075 with the conductivity of titanium, replicates the ‘Titanium’ RTE profile with the exception that the RTE temperatures have decreased by 1K.

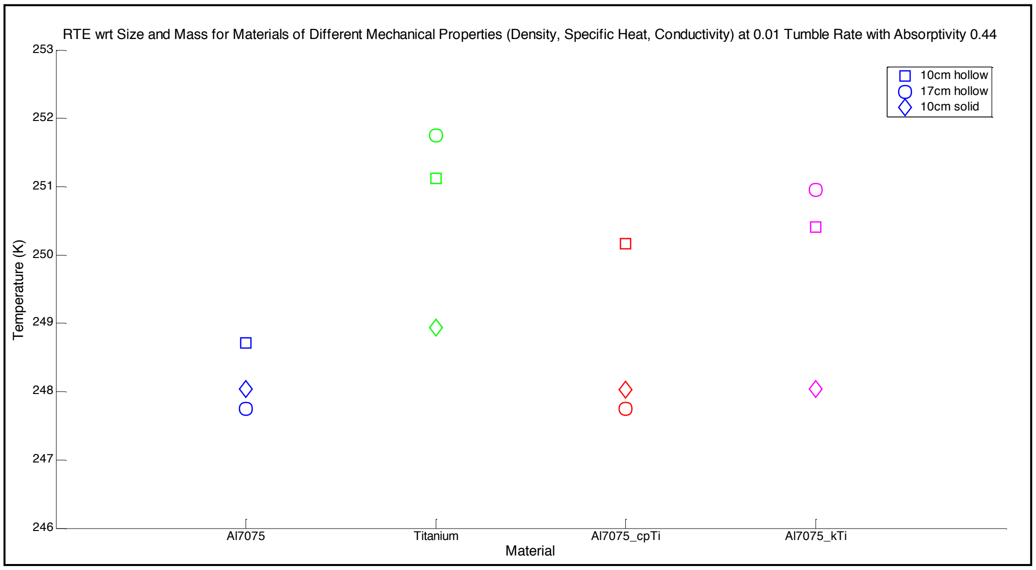

Figure 5.4: RTE of varying materials for differing size and mass debris objects

Figure 5.5 demonstrates that different materials may experience different temperature values for their steady-state RTE; however the size and mass of the debris object itself has little effect on the RTE of the debris object. The maximum temperature gradient within a material simulation occurs in the ‘Titanium’ case and is less than 3K.

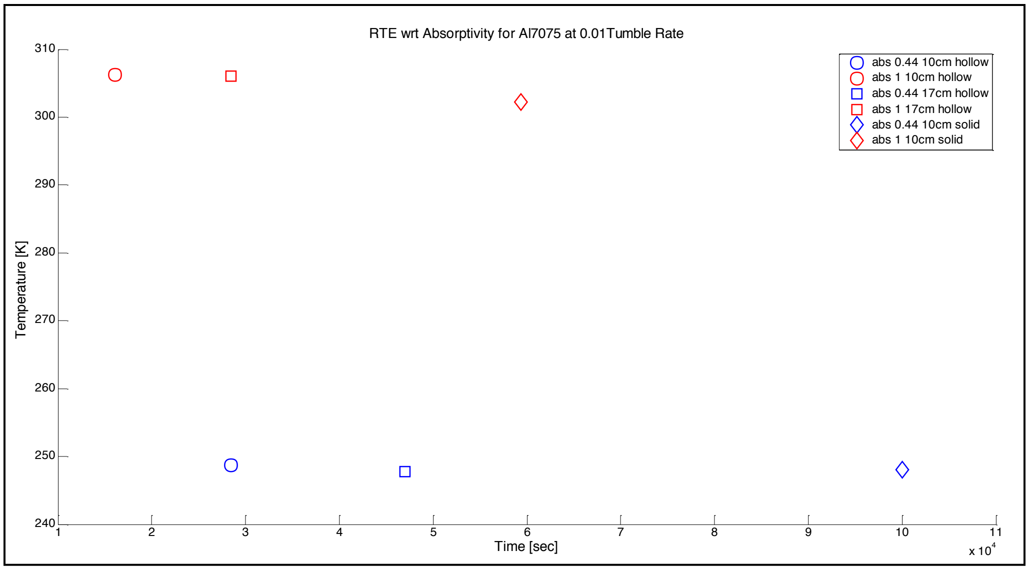

Figure 5.5: Time to steady-state and RTE temperature for varying absorptivity values and debris geometries

This figure also shows the simulation results for three different debris geometries while modulating the absorptivity values for the Al-075 material. This is done in order to investigate the effect that absorptivity and debris geometry have on the RTE temperature and time to reach steady-state. It can be seen that all debris geometries simulated with absorptivity equal to 0.44 reach RTE at 248K +/- 1K. The same debris geometries simulated with absorptivity equal to 1.0 reach RTE at 304K +/- 2K. In accordance with the findings expressed in Figure 5.4, results in Figure 5.5 also show that debris geometry has little effect on the variance of the RTE for a given material. Instead the RTE reached by debris is more dependent on the absorptivity-to-emissivity ratio than on the debris geometry. A material with a higher absorptivity-to-emissivity ratio will reach a higher RTE temperature because it is absorbing radiation at an increased rate relative to materials with lower absorptivity-to-emissivity ratios. Further analysis into Figure 5.5

demonstrates that the more massive an object is, and the lower its absorptivity value is, the longer it will take to reach its steady-state RTE temperature.

Analysis was carried out regarding the tumble rate of orbital debris and its effect on RTE temperature. These results are shown in Figure 5.6. The Al7075 material was simulated for a 10 cm hollow and solid cube having absorptivity values of 0.44 and 1 for three tumble rates: 0.01, 0.1, and 1 rpm. The data points shown in the top subplot of Figure 5.6 are broken out into the bottom three subplots to show detail along the time and temperature axis.

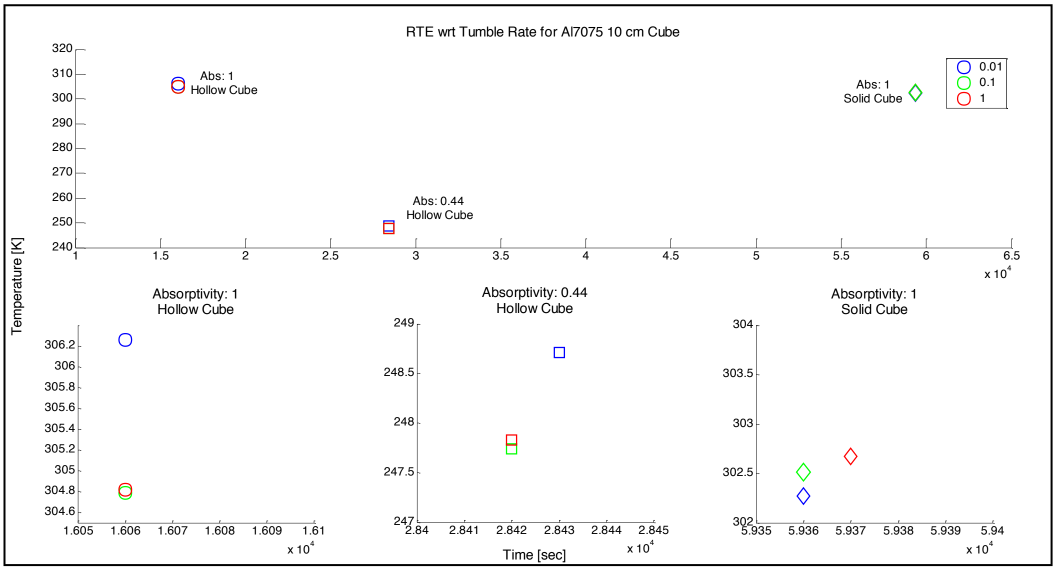

Figure 5.6: RTE versus tumble rate for Al-7075 10 cm

Regardless of tumble rate, analysis of the top subplot of Figure 5.6 leads to findings that are similar to that of Figure 5.5; RTE temperature reached and time to steady-state are dependent upon the mass and absorptivity of a certain debris object. When analyzing the data points representing the different tumble rates in the bottom three subplots, the RTE temperature reached for a given simulation varies by less than 1.5K, while the time to steady state varies by less than 10 seconds.

The last aspect of this analysis is concerned with the temperature deviations experienced by the debris object from one face to another. Figure 5.7 analyzes the RTE temperature versus time to steady state for the different faces of the cuboid debris object. The top and middle subplots in Figure 5.7 shows the data points for three faces of the debris geometry for all three debris geometries simulated.

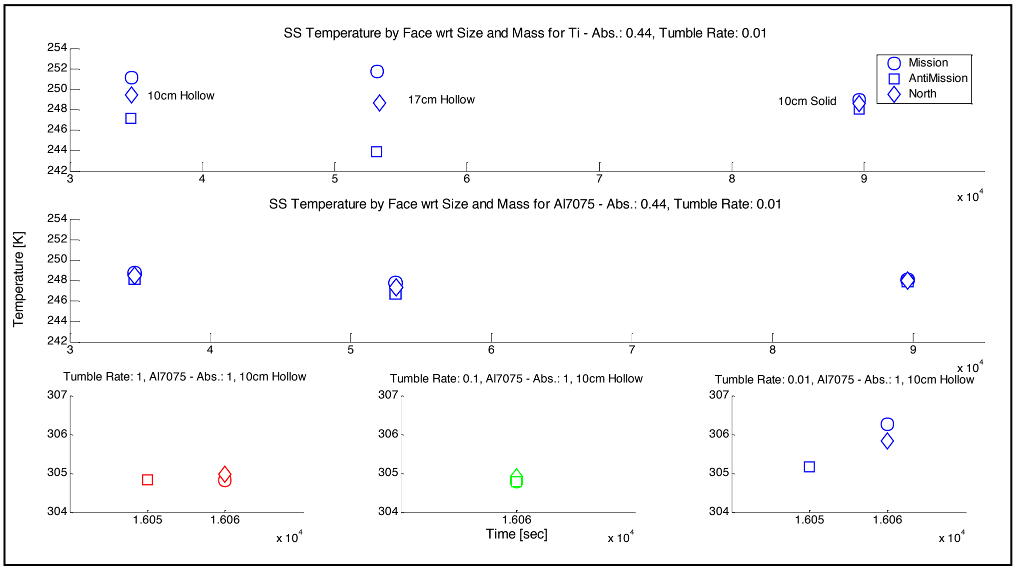

Figure 5.7: Time to steady-state and RTE temperature of multiple faces

The top subplot utilizes titanium for the simulation material with a given absorptivity and tumble rate, while the middle subplot utilizes Al-7075 for the simulation material with a given absorptivity and tumble rate. The maximum temperature gradient between faces, 8K, occurs in the titanium simulation for the 17 cm hollow debris geometry. All inter-face temperature gradients for the Al-7075 simulation are less than 1K. For both materials, the inter-face temperature gradient decreases as the faces become less thermally independent. For fixed material specifications, the smaller and the more solid an object is, the more thermally dependent one face will be on another, therefore decreasing the inter-face temperature gradient. Heat energy will be able to transfer more easily due to the increased amount of thermally conductive connections and decreased distance between faces. The inter-face thermal gradients will be larger for the titanium relative to the Al-7075 due to the decreased thermal conductivity of the titanium. The three subplots on the bottom row of Figure 5.7 show the RTE temperature for an object with fixed material specifications and debris geometry for all three tumble rates. The inter-face thermal gradient for each tumble rate is less than 1K.

These findings are also supported by Figure 5.8 which shows the temperatures with respect to time for three of the six faces of the cuboid debris object. The disparity between face temperatures is greatest for the 17 cm hollow titanium simulation in the top left subplot. As the debris object becomes smaller and more solid (the right-most subplots), the disparity between face temperatures decreases. This transition to a more solid object is accompanied by a decreasing thermal envelope. In addition, as the material's thermal conductivity increases (the bottom subplots), the disparity between face temperatures decreases as well.

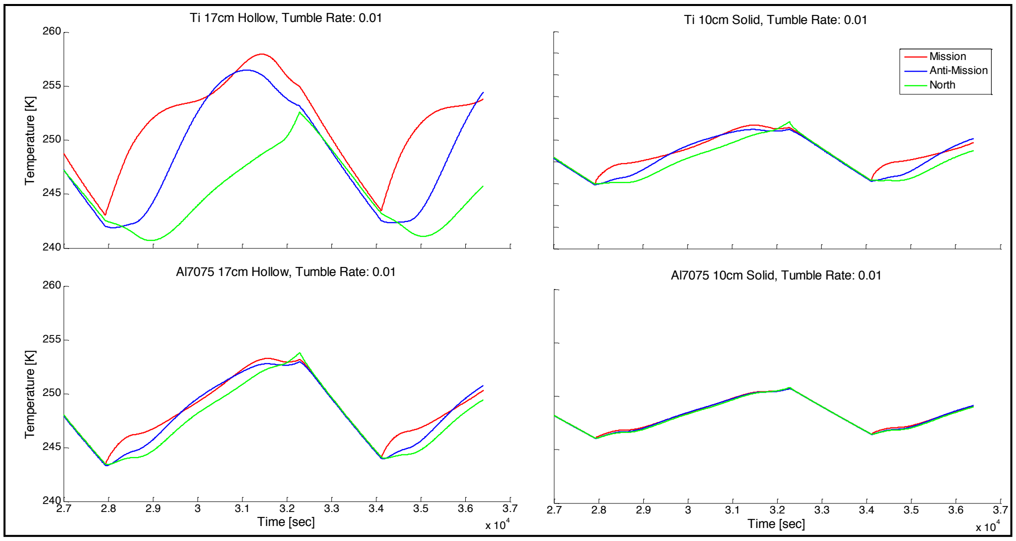

Figure 5.8: Temperature profile by face for varying material, size, and mass debris objects

5.4. Conclusions

Debris objects were modeled with differing materials utilizing both real and hypothetical values for their material and thermal properties for this investigation. The radiance profile was calculated for each face of the cuboid debris object which was simulated in a polar low-Earth orbit. The radiance profile calculated takes into account the radiation emitted from both the Sun and the Earth on the debris object. The radiance profiles are then subjected to finite element analysis utilizing the specified debris geometry, resulting in temperature profiles for each face of the object. These temperature profiles were analyzed and the following conclusions can be made.

The radiative thermal equilibrium (RTE) temperature of an object seems to be a function of material properties, solar absorptivity and emissivity, and is independent of size (10 cm case versus 17 cm case), or mass (hollow versus solid objects). Larger, more massive objects will reach the same RTE as less massive objects with similar properties. However the larger, more massive objects will take longer to reach their RTE. More massive objects will experience a decreased thermal envelope because they will heat up and cool down more slowly than similar, less massive, objects. Faces of a simulated cuboid debris object appear to approach the RTE temperature of the object throughout simulations. The Mission, Anti-mission, North, etc., faces all share similar temperature profiles throughout material simulations. This may allow for certain objects to be treated as a simple isothermal node having a certain orientation and location. RTE temperature appears to be independent of tumble rate for our chosen rates of 1, 0.1, and 0.01 rpm.

Further work should incorporate additional debris geometries such as flat plates, spheres, and other non-cuboid objects into such a study in a varying number of low-Earth orbits. Future analysis should also take into consideration how the thermal behavior of space debris may change due to the aforementioned variations of debris specifications.

6. ASTROMETRIC ANALYSIS

On-orbit trajectory analysis of Local Area objects in low-Earth orbit

Many satellite operators rely in some part on the capabilities of the United States Space Surveillance Network for the operational safety of their spacecraft. A FPA pixel-speed based classifier for rapid orbit characterization and trajectory analysis of LEO objects would be a vital resource for the situational safety of satellites. Knowledge regarding the orbital type and semi-major axis of the observed debris object are extracted, which may aid in the constraint of the admissible region for the initial orbit determination process. This knowledge may also provide an alternative to two-line elements sets for rapidly providing warning regarding potential collisions. The proposed approach assesses the feasibility of performing this analysis for objects in various LEO orbits with simulated space-based observations made from LEO. The debris objects modeled for this analysis are contained within the untrackable population; therefore satellite operators would not have access to data regarding the orbit of the observed debris object. This analysis would increase a satellite’s Local Area Awareness via an intimate understanding of the trajectory of objects passing through the environment surrounding the spacecraft.

6.1. Introduction

The goal of this study is to increase a satellite’s Local Area Awareness. In this dissertation Local Area Awareness is defined as the ability to detect, characterize, and extract useful information regarding resident space objects as they move through the local area relative to any spacecraft. Modeling, simulation, and astrometric analysis of space debris will allow the observing spacecraft to gain insight into the space and debris environment surrounding it. For the purposes of this study, the local area is defined as the 500 km radius sphere that surrounds the sensor platform or observing satellite in Earth orbit. Many objects that pose collision hazards to spacecraft are in similar or counter-rotating orbits relative to the spacecraft. This ensures that many possible collision objects will pass through the local area of the observing spacecraft numerous times allowing for multiple observations. Not all possible collision objects will fit this criterion and may not be observed through multiple orbits due to their out-of-plane trajectory.

This chapter is structured in the following manner. Background and previous relevant work will be described in Section 6.2. Section 6.3 will detail the methods and procedures for the procurement of data from Systems Toolkit 10 [83], (STK 10) and the accompanying analysis performed in MATLAB [82]. The data collected for the simulations and the results regarding these simulations is provided in Section 6.4. Section 6.5 provides a discussion and the conclusions reached on the basis of our findings and their significance within the field of remote sensing and local area sensors. Potential venues to extend this research work are proposed as future work.

6.2. Background

Many of studies on IOD have dealt with the topic of the admissible region as a means for the initial estimation of, and iteration through, sets of orbital parameters towards orbit determination solutions. The research presented here aims to contribute towards this aspect of the IOD efforts for space debris. That is, part of the focus of this work is to effectively extract knowledge regarding the orbital type and differential semi-major axis of the observed object from space-based observations thereby allowing for constraints to be placed on the admissible region.

Novel image processing techniques have been demonstrated by the authors for rapid identification of objects passing through a satellite’s local area. A discrimination technique that does not require the generation of a TSA was developed to rapidly distinguish those objects which may pose collision hazards [85]. The discrimination techniques examines the instantaneous angular rates of the object relative to the observing spacecraft for detection of possible collision detection, as opposed to calculating initial orbital elements and extrapolating of object orbital position via different propagation techniques. This astrometric classifier, based on the relative speed of an object across the focal plane array (FPA), has been shown as a feasible method of discrimination for collision threats of various circular and near-circular, slightly elliptical and near-GEO orbits with the observations made from a GEO-orbit. The current work, reported here, is to assess the feasibility of performing this analysis for objects in various LEO orbits from observations made from LEO. Further analysis aims to catalog and register local area environment objects through multiple observations. These observations will focus on the synchronicity of the debris object’s orbit and observing satellite’s orbit, and the variance in the FPA pixel-speed classifier as a means of extracting further information regarding the current and future trajectory of the object.

Further validation of a FPA pixel-speed based classifier for rapid orbit characterization and trajectory analysis of LEO objects would be a vital resource for the situational safety of satellites. The current study will quantify the ability of a LEO satellite to monitor, detect, correlate, and register objects, in a semi-autonomous manner and perform the required variance analysis through multiple observations of the same object. This would enable LEO satellite operators to have an accurate understanding of imminent debris threats, both trackable and untrackable by the SSN, and the space environment surrounding the observing spacecraft. This type of analysis is of greater significance when two-line element sets are not available. Two-line element sets for debris objects, which could be indicative of possible debris collision-threats, may not be available due to the size of the debris object, inaccurate orbit metrics, or previous uncorrelated object tracks.

6.3. Methods

The STK 10 software suite was utilized for visualization and examination of several scenarios regarding the interactions of objects in various low-Earth orbits with that of a sensing platform which was placed in a pre-determined polar orbit. The observing sensor is housed on a satellite in a pre-determined polar orbit and will be referred to as the observing satellite. The observing satellite, and all simulated objects contained in each scenario, were propagated with the STK 10 propagator called J2. It accounts for the J_2 Earth gravitational field expansion term. While the J2 propagator does not account for a full gravity field model, it does produce a general approximation for the evolution of an object's orbit due to the significant effect of the asymmetry in the Earth's gravitational field. This effect is expressive of the hemispherical oblateness of the Earth [86].

In STK 10, the J2 propagator does not take into consideration the geometry of the satellite or orbiting debris object and therefore does not contain a term for atmospheric drag or solar radiation pressure, but models the objects as a point mass.

The focus here is placed on objects that pass within the local area surrounding a satellite or sensor platform. For the purposes of this study, the local area is defined as being a 500 km radius sphere surrounding the observing satellite; all objects that pass through this sphere will be subject to trajectory analysis. The local area sensor, which monitors the aforementioned local area, will be mounted on the observing satellite in a circular polar orbit with prograde motion. All following observations will be made relative to, and access intervals determined by, the orbit of this observing satellite. The orbital elements of the observing satellite are given in Table 6.1.

Table 6.1: Initial orbital elements of observing satellite

Semi-major Axis	Orbital Period	Eccentricity	Inclination	Argument of Perigee	RAAN	True Anomaly
7178.14 km	100.7 min	0	98	0	0	0

The simulations performed in STK 10 model twenty-five objects in five low-Earth orbit types. The analysis is constrained to these objects and their respective initial orbits. The five low-Earth orbit types are: 1) in-plane circular orbit with prograde motion, 2) circular orbit with differing inclination as to result in a crossing orbit relative to the observing satellite, 3) in-plane elliptical orbits, 4) in-plane circular orbit with retrograde motion, and 5) in-plane decaying debris due to the effects of atmospheric drag. For the rest of this chapter these orbital types will be referred to numerically as they were previously described, hence orbital types 1, 2 3, 4, and 5. Atmospheric drag is ignored in orbit types 1 through 4. For orbit 5, the SGP4 propagator is used and takes into account orbital decay using a model for atmospheric drag. For each of the first four orbital types that will be simulated, six variations of that orbital type are constructed by changing the semi-major axis of the object's orbit. The six variations will have a differential semi-major axis relative to the observing satellite: 200km above, 100 km above, 50 km above, 50 km below, 100 km below, and 200 km below. Orbital simulation details for all orbital scenarios are given in Appendix B.

Although Appendix B does not provide an exhaustive list of orbits that debris or other space objects will have throughout their lifetime, it is meant to approximate a significant range of the orbits that will be seen as orbital debris and space objects evolve due to the J2 perturbations and effects modeled by the SGP4 propagator. These debris objects may have their genesis in collisions, explosions, shedding or other events. Figure 6.1 demonstrates the interaction of the observing satellite with a debris object of orbital type 1, in-plane circular orbit with prograde motion, and a different semi-major axis relative to the observing satellite. The local area of the observing satellite is visualized as a white sphere traveling through space surrounding the observing satellite; the orbital track of the observing satellite is in light-blue. The arc length of the orbital track of the debris object will be red for all points along the orbital track when the object is within the local area of the observing satellite and observation by the local area sensor is possible. The purple line illustrates the orbital track of the object for a segment in which the object is not yet within the local area; this orbital track has turned red for a future segment in which the object will be within the local area of the observing satellite. For the snapshot shown in

Figure 6.1 the debris is currently not within the local area sphere, but as the sphere moves it will enter the sphere at the point shown where the orbital track of the debris becomes red.

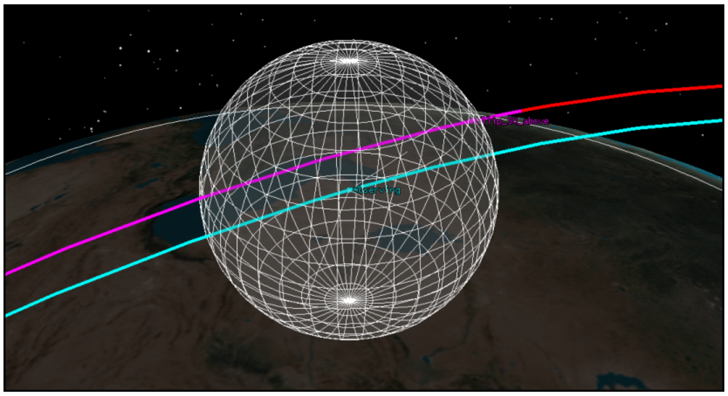

Figure 6.1: Object passing through Local Area sphere

The only constraint placed on the data providers in STK for the simulations is that the object must be within the local area of the observing satellite for data to be polled. While the object is within the local area of the observing satellite, the sensor which will have "access" to the object and the "Sensor Based Angles" data provider will yield time of access, access pass number, angle off sensor boresight, and horizontal angle and vertical angle relative to the sensor boresight. This assumes all object, that are within this sphere can be detected. This is a broad approximation, for a more detailed analysis see [87], [88]. This data will provide the necessary information for the trajectory analysis and differential semi-major axis analysis which is documented below.

6.4. Results

The trajectory analysis being performed can be broken into two components: differential semi-major axis determination and orbital type determination. The results section will cover two different approaches for accomplishing the trajectory analysis: access interval analysis and astrometric, or angles, analysis. The differential semi-major axis determination and orbital type determination can be performed with either approach. A subsequent analysis on decaying orbital debris is also provided. The following discussion will describe the two approaches in detail and highlight the benefits and constraints of each approach.

6.4.1. Access Interval Analysis

The purpose of the access interval analysis is to determine if the different orbit types have characteristic access times associated with them that can act as an orbit type discriminator. The access interval analysis is performed for all times in which the local area sensor has access to the objects whose orbits are described in the Appendix. For each simulation it is assumed that access to the observed objects can be registered and correlated with previous and future object passes. With this assumed registration, either from optical signatures or other means, the analysis can look at successive passes of the object through the local area of the observing satellite and for each respective access interval. Both the duration of each access interval and the time between access intervals are used in this analysis. Access duration is defined as the time in which the object is within the local area; the time between observations is defined as the time between any standard and reproducible point in the object's orbital track relative to the observing sensor for consecutive passes. For our purposes the time between initial detection or access onset of consecutive passes was used to define the time between observations. However, if the local area sensor is not able to detect throughout the extent of the entire local area, then the time at which the object passes through the horizontal or vertical planes of the sensor boresight could be used as the definition for determining time between consecutive accesses.

The top subplot in Figure 6.2 illustrates the orbital periods for each differing semi-major axis. The bottom subplot in Figure 6.2 represents the differing orbital period of the debris object relative to the observing satellite due to their differential semi-major axes. The differential orbital period is positive when the debris object has a semi-major axis less than that of the observing satellite, which means the debris object is, on average, moving faster than the observing satellite. The sign is reversed when the debris object has a semi-major axis greater than that of the observing satellite, which means the debris object will, on average, move more slowly than the observing satellite.

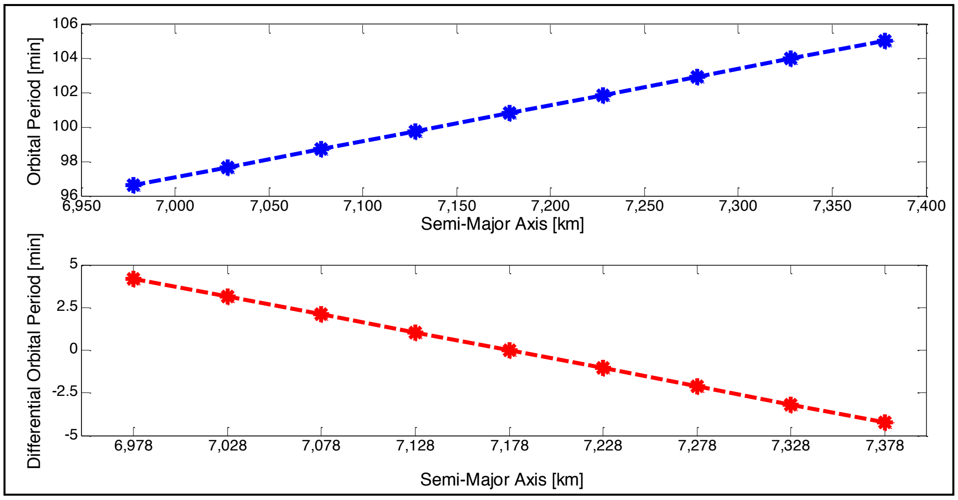

Figure 6.2: Orbital period and differential orbital period for differing semi-major axis

Equation 6.1 expresses the orbital period, *T*, of an object having a semi-major axis represented by the variable 'a'. The variables '*G*' and '*M*' represent the gravitational constant and the mass of the Earth, respectively.

$$T = 2\pi\sqrt{\frac{a^3}{G\cdot M}} \tag{6.1}$$

The differential orbital period of a debris object relative to the observing satellite is expressed in Equation 6.2. The variables '$a_{observing}$' and 'a_{debris}' represent the semi-major axis of the observing satellite and the debris object being observed, respectively.

$$\Delta T = \frac{2\pi}{\sqrt{G\cdot M}}\left(\sqrt{a_{observing}^3} - \sqrt{a_{debris}^3}\right) \tag{6.2}$$

Figure 6.3 shows the observation and access data for the first four orbital types (where atmospheric drag is not included) with a differential semi-major axis of 200 km relative to the observing satellite; the elliptical case is shown having a differential semi-major axis of 100 km relative to the observing satellite. The elliptical case having a differential semi-major axis of 200 km relative to the observing satellite will be subsequently discussed in detail as it a special case.

The subplot in the top left quadrant, subplot 'a' of Figure 6.3, demonstrates orbital type 1 where both the observing satellite and the observed object are in similar in-plane circular orbits with prograde motion. Access from the sensor to the observed object is occurring approximately every 2350 minutes. It can be seen that there exists other consecutive access intervals that occur on a very short time scale, such is the case for observation 31. These data points are due to the sensor losing and regaining access to the observed object on the same orbital pass and are therefore not considered for further analysis. In this case, when considering the time between sensor access there is a single "level" of approximately 2350 minutes. This level is established because of the differential orbital period of the observed object relative to the observing satellite. With both objects in prograde motion orbiting the Earth and in the same orbital plane, the only possibility for access occurs when the object with the smaller semi-major axis, and shorter orbital period, "catches up" to the other object.

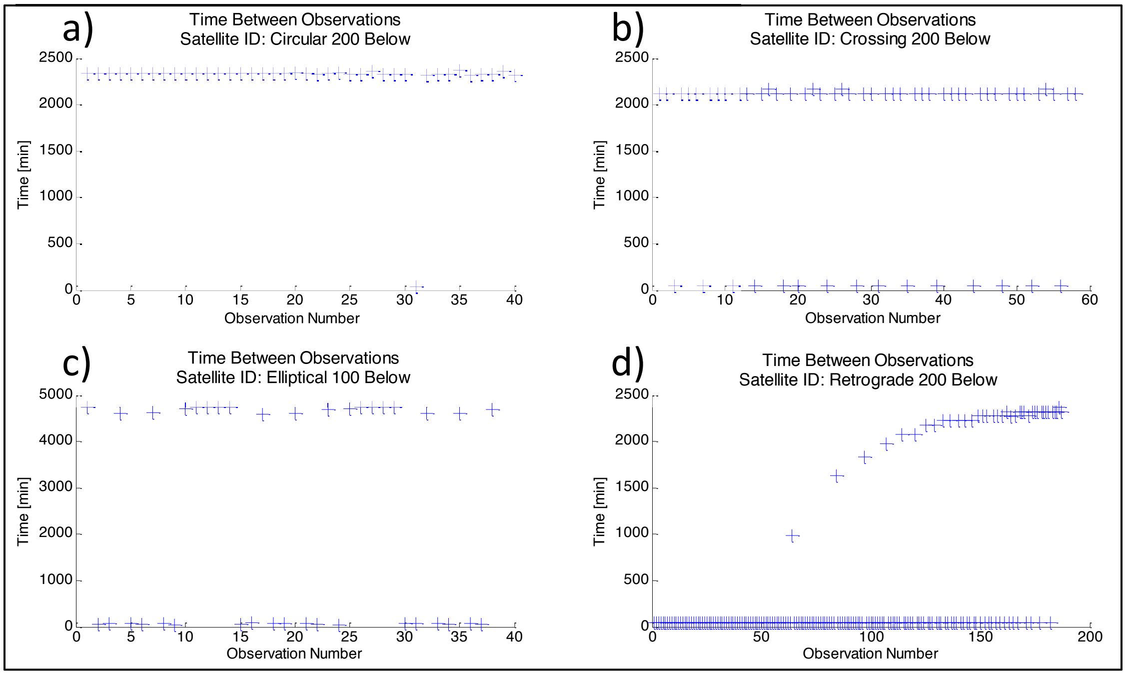

Figure 6.3: Access interval durations and level for circular, crossing, elliptical, and retrograde orbital types

The access data for orbital type 2, which results in a crossing orbit, is shown in subplot 'b' of Figure 6.3. Orbits with different inclinations will have intersecting orbital planes. This intersection of orbital planes means that the time between observations will have two levels as is the case with the aforementioned subplot. The upper level for the crossing orbit case shown in Figure 6.3 is approximately 2200 minutes, while the lower level for time between consecutive accesses is 49.2 minutes. The upper limit is partially due to the differential inclination, intersection of the orbital tracks, and because one object is orbiting the Earth faster than the other object due to their differential semi-major axis. Recall that the orbital periods for all objects are shown in the Appendix. Once the two objects are out of phase, along their orbital tracks relative to the intersection of their orbital planes, it takes a significant amount of time for the objects to be aligned in such a way with respect to their orbital tracks that access occurs. However when access does occur there is a high likelihood that the object will be accessed again within the same orbit on the opposite side of the Earth. When this is the case a second, lower level appears in the time analysis plots.

For orbital type 3, which is the elliptical orbit case, orbits and eccentricities were chosen such that the perigee and apogee of the observed object will dictate that its orbital track will pass both above and below the observing satellite on every orbit, and therefore increase the possibility of collision with the observing spacecraft. Subplot ‘c’ of Figure 6.3 shows the elliptical scenario for an object with a semi-major axis that is 100 km below the semi-major axis of the observing satellite. Similar to the crossing orbital scenario, there exist two levels for the time between consecutive observations. The upper level is due to the difference in semi-major axis relative to the observing satellite. Data points on the lower level occur when the observing satellite accesses the object numerous times on the same orbit, because the elliptical trajectory of the object brings it in-to and out-of the local area. For the elliptical orbital scenario there is a special case in which the orbital track of the object will pass both above and below the observing satellite, similar to the case previously stated; however, it has an apogee that dictates at least part of its orbital track will take it out of the local area of the observing satellite.

Orbital type 4, which is the last orbital scenario presented in the access interval analysis, is the circular case with the object in a retrograde motion. The circular scenario with retrograde motion, shown in subplot ‘d’ of Figure 6.3, does not possess the static upper and lower levels demonstrated in previous cases. The lower level is static and the data points contained on this level occur when the observing satellite accesses the observed object twice per orbital pass, and since they are traveling at very high relative velocities these interactions happen rapidly. The access intervals for the retrograde objects happen in bursts; this means that there will be many consecutive access intervals with a short amount of time between observations. These access bursts end with a significant delay until the next access. As the retrograde orbit evolves, the amount of accesses contained within a burst decreases while the delay between bursts, the upper level, increases. This dynamic is due to the effect that the J2 perturbation is having on the orbit of the object in retrograde motion. The object in retrograde motion will start in the same orbit as the observing satellite, only having a different semi-major axis. As the orbital planes are still nearly aligned and the angle between orbital planes remains small, the sensor will have access to the observed object for numerous passes with a short duration between consecutive accesses. However, as the orbit of the object in retrograde motion evolves due to the effect of the J2 perturbation, the angle between the orbital planes increases therefore decreasing the amount of observations per burst and increasing the duration of time between bursts. As the orbit planes continue to separate this case will look similar to orbital type 2, with the difference being the object would be in a retrograde orbit. Note that the data shown in Figure 6.3 corresponding to the upper and lower levels for the time between consecutive accesses is averaged and aggregated together for comparison.

There exists a special case for the simulated elliptical orbit type which has an apogee that dictates at least part of its orbital track will take it out of the local area of the observing satellite. The time analysis of this case is shown in Figure 6.4. It can be seen that there are three levels when the apogee for an elliptical orbit makes part of its orbital track unobservable for the observing satellite, due to the definition for the size of the local area. The middle level for this case is similar to the high level for the previous elliptical orbital scenario; data points on this level occur when the object is accessed according to the difference in orbital period between the object and the observing satellite. The lower level for this case is also similar to the previous elliptical orbit scenario; the data points on this level occur when the object is accessed numerous times on the same orbital pass. The upper level for the special elliptical case is due to the objects being aligned in their respective orbital tracks, which would have previously made access possible; however, the observed object is passing through the apogee of its orbital track which is now outside of the local area of the sensor and therefore not observed until the next time the objects align in their orbital tracks and the observed object is again within the local area of the observing satellite. Due to these effects the upper level for the time between observations is twice the duration of the middle level. The effect would be similar if the perigee of the orbit was sufficiently low to bring the object outside of the local area.

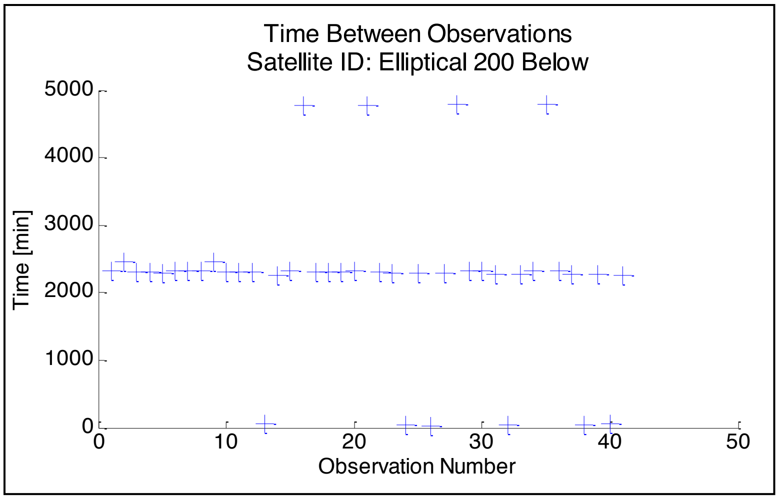

Figure 6.4: Access interval durations and level for elliptical orbit

In Figures 6.5 through 6.8 the data representing the magnitude of the time-averaged levels in minutes is represented graphically with a "+" indicating orbits with a semi-major axis greater than the observing satellite orbit and a "O" indicating orbits with a semi-major axis smaller than the observing satellite orbit. Upon visualizing that data in this way, it becomes clear that the extracted levels data from the observation and access data make possible the differentiation of the semi-major axis of the observed object and its orbital type. For all cases, except the elliptical case with 100 km differential semi-major axis relative to the observing satellite, only one level is necessary to uniquely identify the difference in semi-major axis if information regarding the orbital type is known. In the elliptical case with 100 km differential semi-major axis, the lower limit value can discern between the differences in semi-major axis, however it cannot discern between whether that difference in semi-major axis is either greater or smaller than the semi-major axis of the observing satellite. This problem is resolved if the upper and lower levels for time between observations, as illustrated in Figure 6.3 and Figure 6.4 and quantified in Figures 6.5 - 6.8, thereby allowing for the orbital type and differential semi-major axis to be uniquely identified.

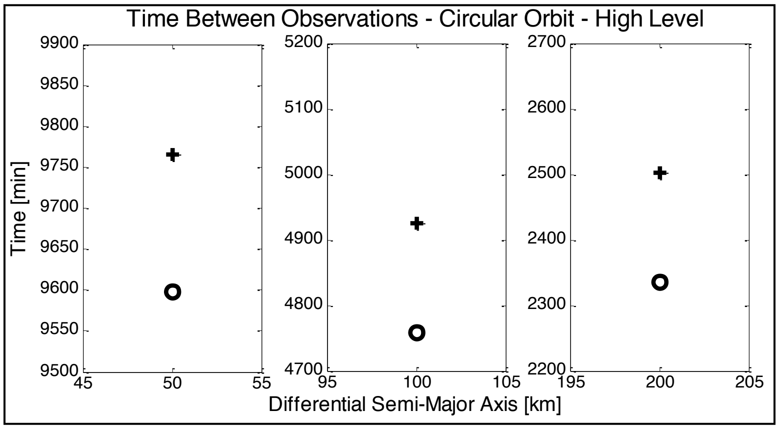

Figure 6.5: Access interval levels for orbital type 1: circular - prograde

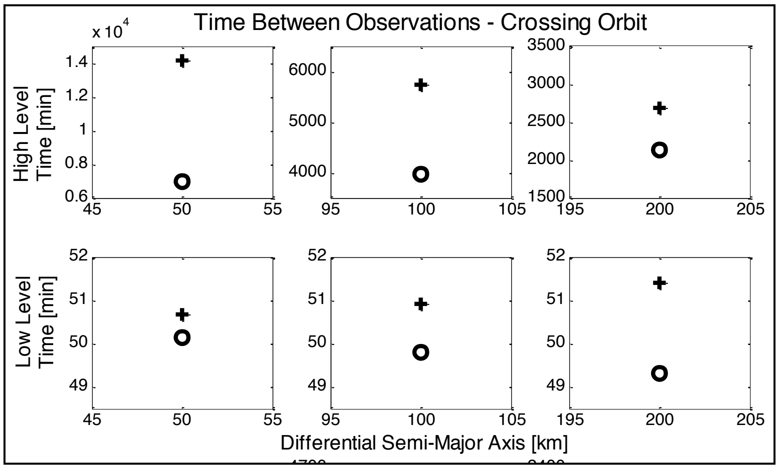

Figure 6.6: Access interval levels for orbital type 2: crossing

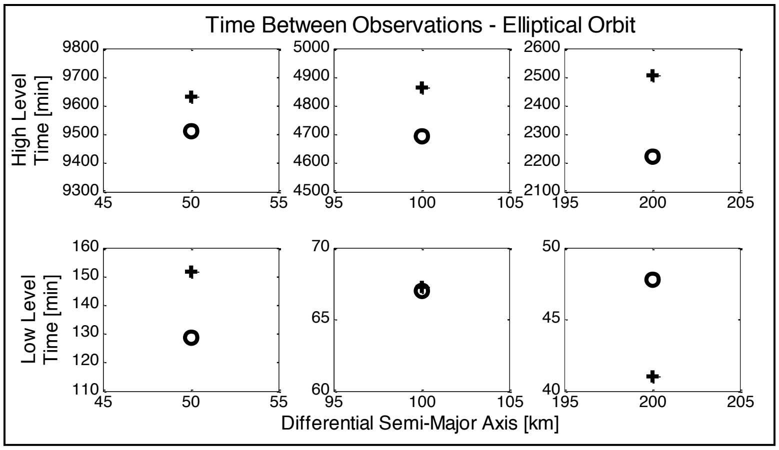

Figure 6.7: Access interval levels for orbital type 3: elliptical

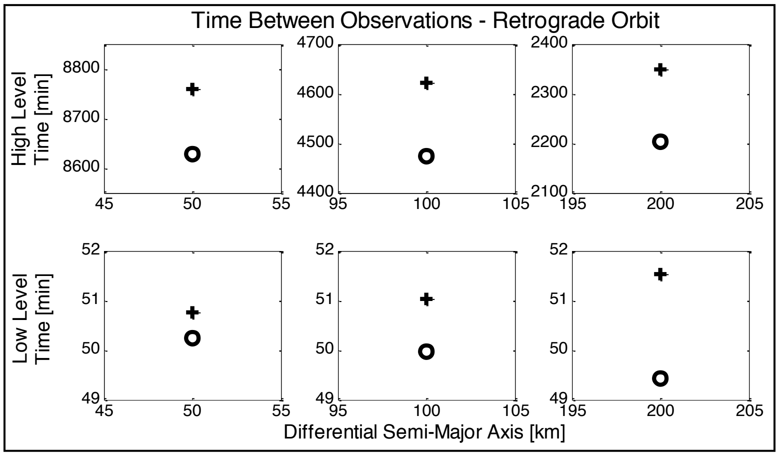

Figure 6.8: Access interval levels for orbital type 4: circular - retrograde

6.4.2. Astrometric Analysis

For all times that the sensor has access to the observed object, the object is projected on the FPA and angles data can be extracted. The angles that are used for the astrometric speed analysis are the horizontal and vertical angles relative to the boresight of the sensor. The sensor boresight is aligned along the nadir axis of the spacecraft. For the cases with a semi-major axis less than that of the observing satellite the sensor is oriented along the positive-nadir axis, and the negative-nadir axis for cases with a semi-major axis greater than the observing satellite. These angles are derived as a function of their position along the FPA and a derivative operation is performed yielding the angular rates as projected along the horizontal and vertical axes of the FPA. Due to the alignment of the sensor, the horizontal axis projection lies along the in-track component of the observing satellite orbital track while the vertical axis projection lies along the cross-track component of the observing satellite orbital track. This can be thought of as a projected angular speed. The track speed is also calculated which takes into account both the horizontal and vertical projections of the object along the FPA. Since the debris object and the observing satellite are in similar orbits the behavior in the graphs in this section is a measure of the amount of similarity in the orbits of the debris and the observing satellite.

For the circular orbital scenarios the range from sensor to object during access is shown in Figure 6.9. The sensor will not have range data to the object, however from Figure 6.9 it can be seen that all access intervals start when the object enters the local area at a range of 500 km. Due to the different orbital periods of the observed object, the object that passes within 50 km of the sensor will have significantly longer access duration than the object passing within 200 km of the sensor. As expected, this figure shows that duration for all passes of objects with a differing semi-major axis of 200 km, either above or below the sensing platform, have an access interval around 51 minutes. Access duration increase for the 100 km and 50 km differential semi-major axis cases are around 104 minutes and 212 minutes respectively. This dynamic is manifest in the “Horizontal

Angular Speed” subplot in Figure 6.10, which illustrates the horizontal angular rate at the beginning of the access interval. Figure 6.10 illustrates horizontal and vertical angular speed plots for orbital type 1, the in-plane circular orbital scenario with prograde motion. These plots are shown for all values of differing semi-major axis for numerous passes. Due to the similar relative in-plane motion of the observing satellite and the observed object for the circular orbital scenario, significant deviations in the angular rate of the object will be seen in the horizontal or in-track projection while the vertical or cross-track angular rate will be significantly smaller. With the horizontal angular rate being much greater than the vertical angular rate, the track speed across the FPA will be dominated by horizontal angular rate. The horizontal angular projection curves differ in magnitude at the onset. The magnitude of the horizontal angular speed at access onset increases as the differential semi-major axis increases. For the 50 km, 100 km, and the 200 km differential semi-major axis cases the magnitude of the horizontal angular speed at access onset is 0.001, 0.004 and 0.015 degrees-per-second respectively. Therefore the magnitude of the horizontal angular speed at access onset, in addition to access duration, can be used as a discriminator between prograde circular orbital types with differing semi-major axes.

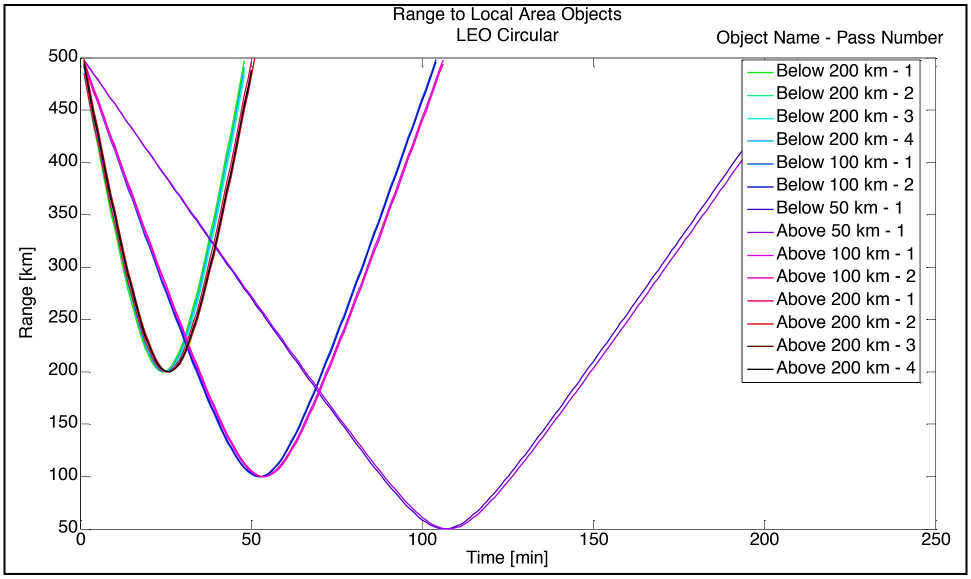

Figure 6.9: Range for Local Area accesses – circular orbit

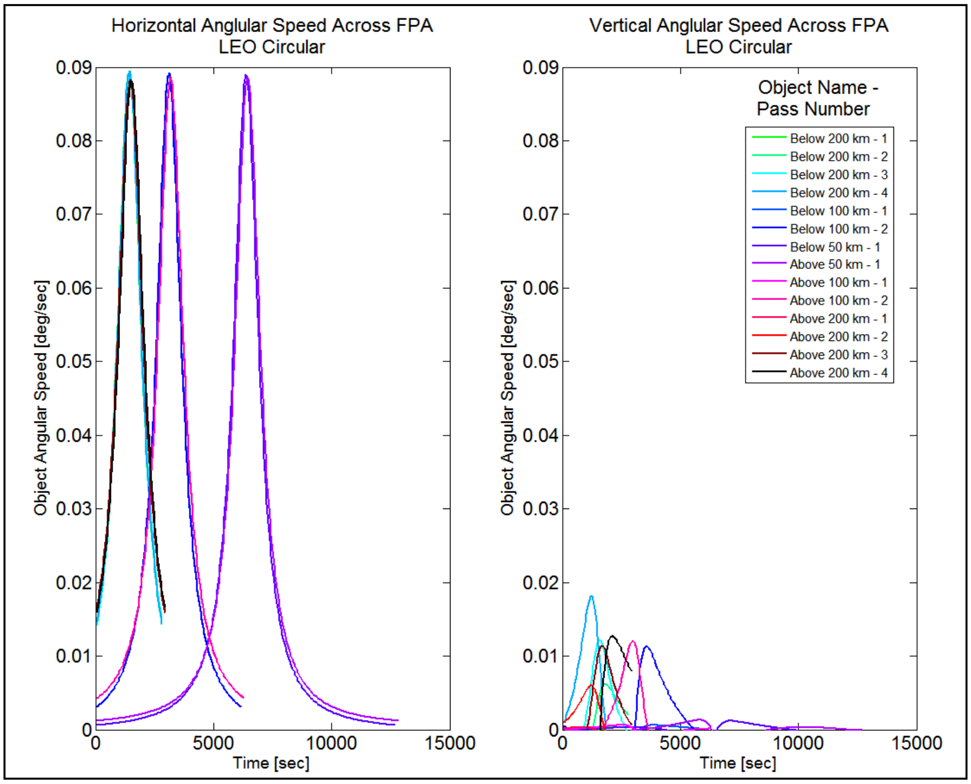

Figure 6.10: Horizontal and vertical projected angular rates for prograde circular orbital cases

Figure 6.11 centers the horizontal angular rate curves on their maximum value, which for orbital type 1 is the point of closest approach. The time represented by the x-axis in Figure 6.11 will be the relative time measured from closest approach as opposed to the simulation time in Figures 6.9 and 6.10. This demonstrates that all horizontal angular rate curves for orbital type 1, regardless of their semi-major axis, fall on a similar curve. In Figure 6.11 the different magnitude at access onset significantly differs based upon its differential semi-major axis. The differential semi-major axes, represented as Δa, of 50 km, 100 km, and 200 km have values of 0.001, 0.04, and 0.015 degrees per second.

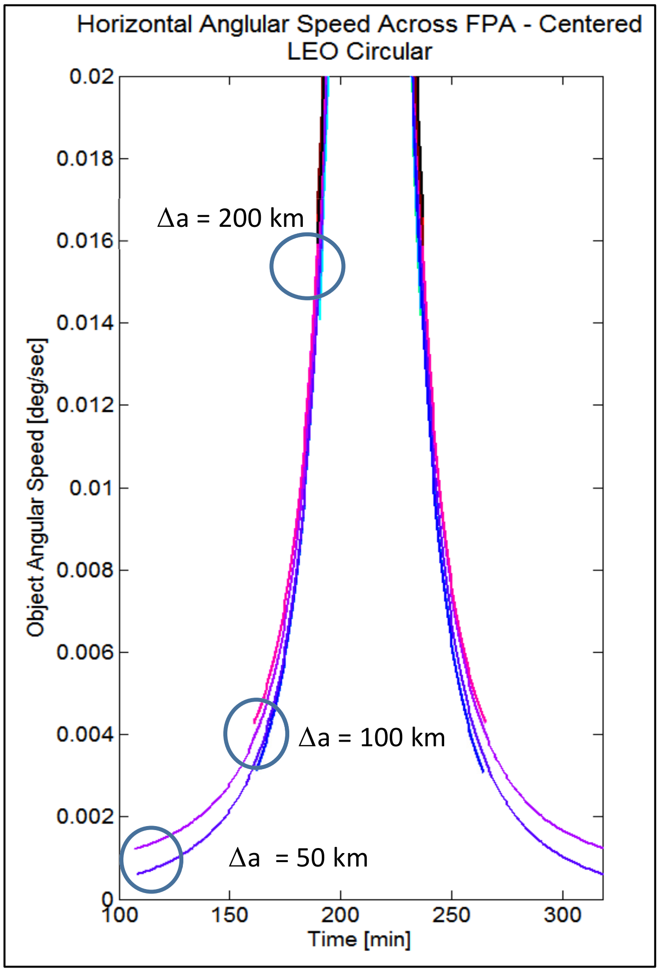

Figure 6.11: Centered projected horizontal angular rate – circular orbit

Similar analysis can be performed for the orbital scenarios where the object and observing satellite will have crossing orbits, as is the case with orbital type 2. Figure 6.12 shows the centered vertical angular projection rates for the crossing orbital scenarios. The time represented by the x-axis in Figures 6.12 and 6.13 will be the relative time measured from closest approach The crossing orbital scenarios will have many more passes because the sensor will have the opportunity to access the observed object twice every orbit when they are in phase. This also means that the J_2 perturbation on the orbit will have a greater effect on the alignment of the objects relative to each other and will therefore result in more partial track observations than the prograde motion circular case. A partial track is created any time the object will not be observed as crossing either the horizontal or vertical boresight axes. When a full track observation does occur, it can be seen from Figure 6.12 that as the differential semi-major axis decreases from 200 km to 50 km, the leftmost subplot to the right most subplot, the peak vertical angular rate increases sharply thereby allowing for discernment between differential semi-major axes. Figure 6.13 demonstrates that the same analysis can be performed with the horizontal angular rate for orbital type 4, the in-plane retrograde circular orbital scenarios.

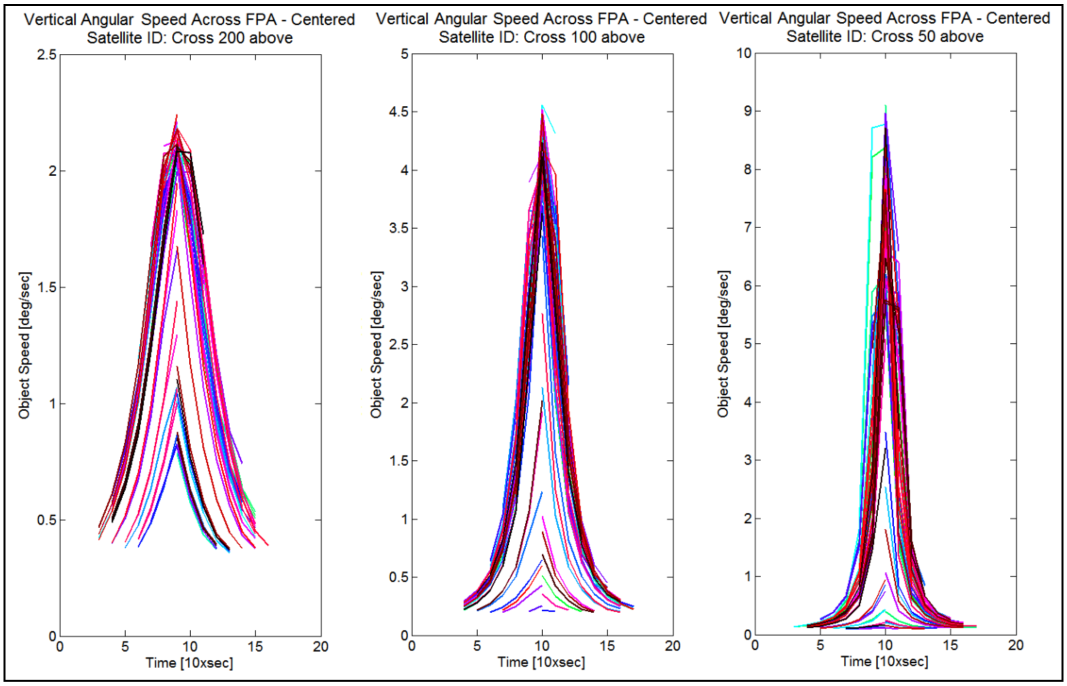

Figure 6.12: Centered projected vertical angular rate – crossing orbital scenario

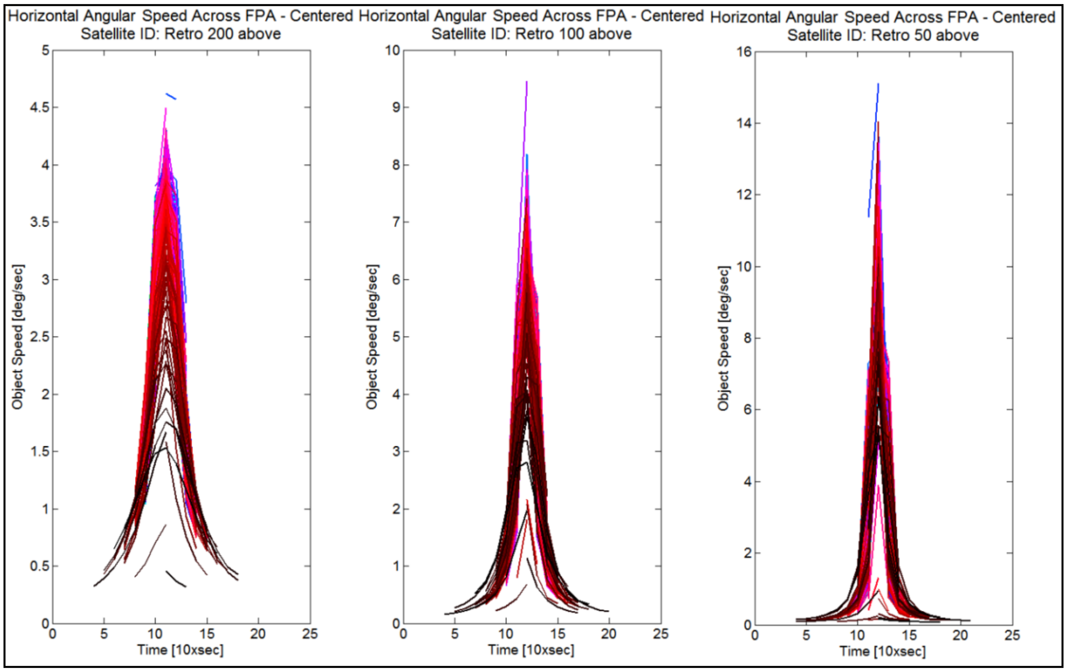

Figure 6.13: Centered projected horizontal angular rate – retrograde - circular orbital scenario

The elliptical orbital scenario cases, orbital type 3, are more convoluted when it comes to the differential semi-major axis determination relative to the observing satellite. Figure 6.14 shows that centered horizontal angular rate plots for the elliptical cases yield sharp peaks whose magnitudes cannot be used as a discriminator for their differential semi-major axis. These rapid changes in the horizontal angular rate are due to the range from the sensor to object decreasing due to the differing eccentricities of their orbits. When this is the case, the observed object will be closer to the sensor and therefore moves much quicker across the FPA due to the parallax effect. It is worth noting that these rapid transitions can be utilized as flags indicating that the object is within close proximity to the observing satellite and may pose a collision risk on future orbital passes. The three subplots contained in Figure 6.14 represent the three differential semi-major axes. The larger the differential semi-major axis is the shorter the access duration will be. This is due to the differential orbital periods resulting from the differential semi-major axis and thus the reason the durations appear different for each subplot. The different colors represent subsequent passes for each object.

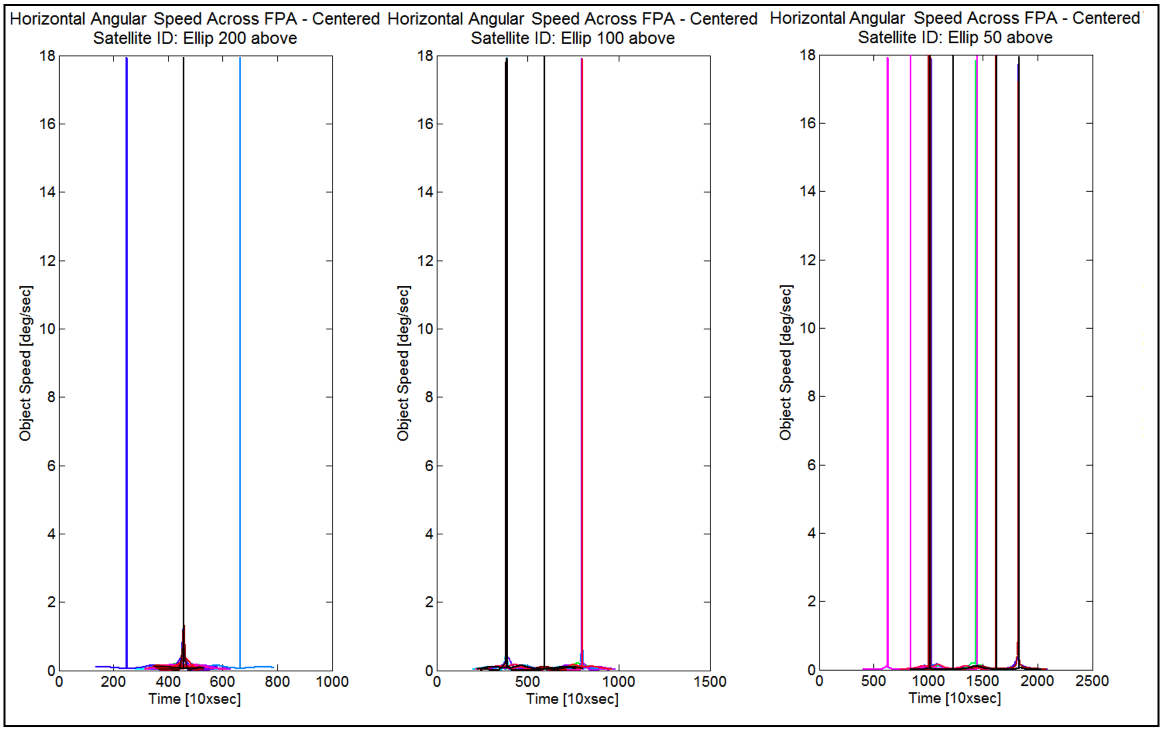

Figure 6.14: Centered projected horizontal angular rate – elliptical orbital scenario

6.4.3. Decaying Orbital Debris

The last case to be considered is the decaying debris scenario, orbital type 5. The debris object being observed is initially set in an in-plane circular orbit with prograde motion and utilizing the SGP4 propagator which accounts for atmospheric drag, which will result in the decay of the debris object over time. The object will decay into an orbit where it will pose a collision risk and then continue to decay below the observing satellite. Figures 6.15 and 6.16 illustrate the evolution of the orbit through the horizontal angular rate for consecutive observations leading up-to, and following the possible debris-to-sensor collision. In Figure 6.15, the horizontal angular rate curve changes as the object experiences decay due to atmospheric drag. The observation duration increases while the horizontal angular rate at onset decreases for each successive pass. These dynamics are demonstrative of the orbit, while appearing circular at each pass, having a decreasing differential semi-major axis relative to the observing satellite. Initially these horizontal angular rate curves would be categorized as circular with a differential semi-major axis relative to the observing satellite. This categorization would then be labeled as a non-future collision threat if only a single pass of the object was observed. However since multiple observations have occurred it can be seen that the orbits is in fact not circular but decaying at a certain rate and will pass through the orbital track of the observing platform causing a future collision threat. This trend is reversed in Figure 6.16 as the debris continues to decay below the observing satellite with an increasing differential semi-major axis.

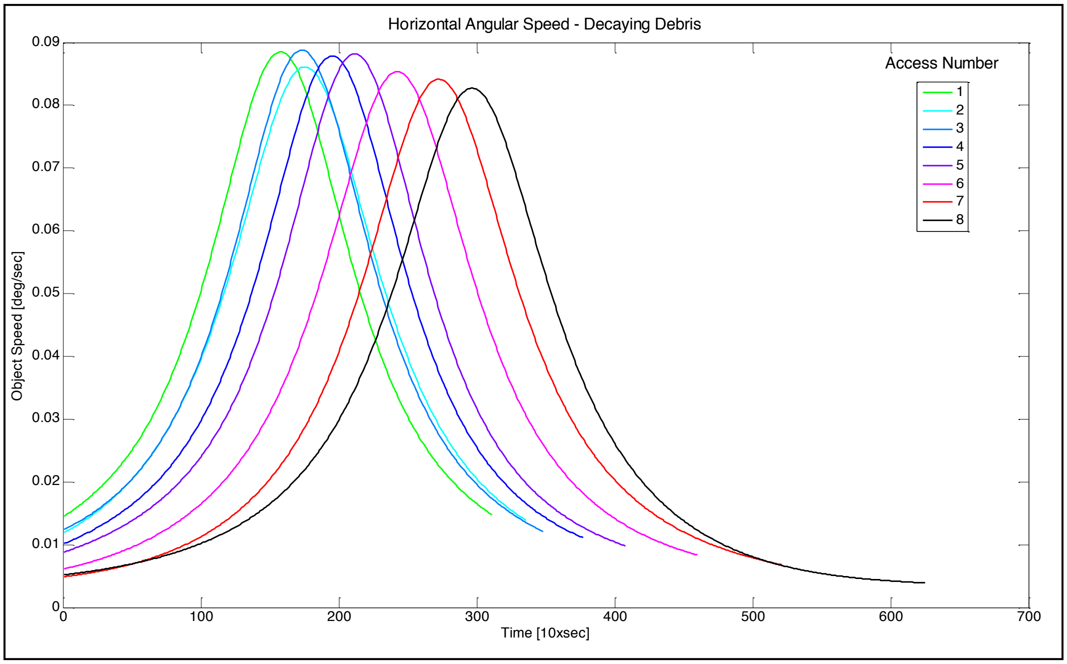

Figure 6.15: Projected horizontal angular rate – decaying debris with decreasing differential semi-major axis

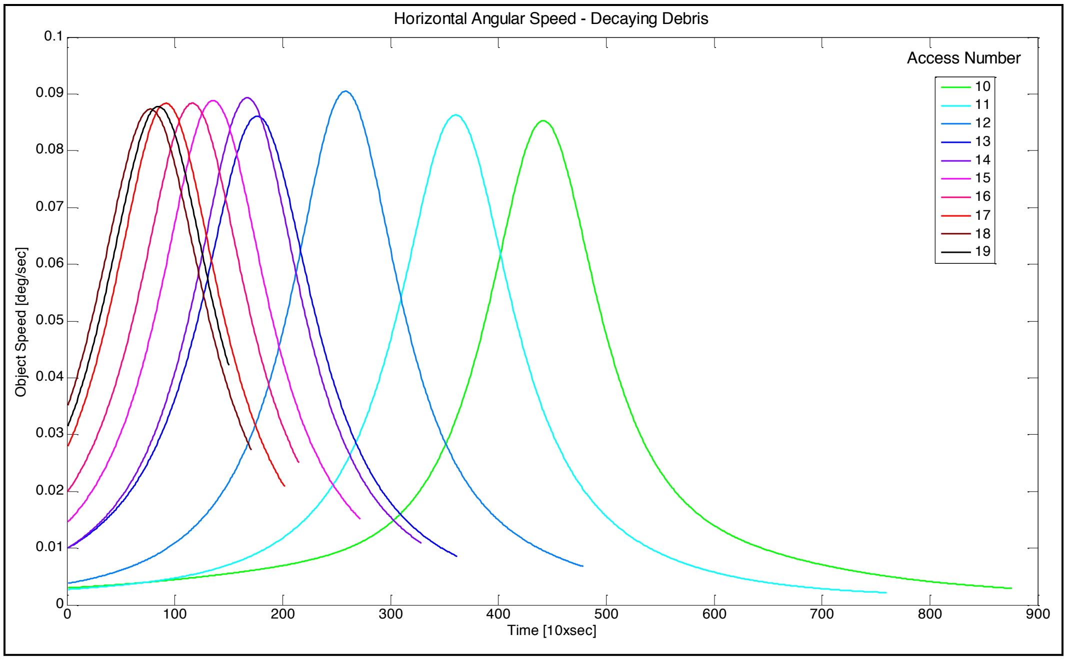

Figure 6.16: Projected horizontal angular rate – decaying debris with increasing differential semi-major axis

Information regarding the future trajectory of the decaying orbital debris can also be extracted from the access interval analysis in the decaying debris scenario. Although distinct levels do not exist for the time between observations, patterns are evident when considering both the duration of the access intervals and the time between access intervals. These trends are shown in Figure 6.17. These subplots show that both the duration of the access interval as well as the time between access intervals increases as the objects decay into an orbit with a similar semi-major axis relative to the observing satellite. Once entering into this similar orbit, the only point at which the debris object may cause a collision possibility, the debris will continue to decay and increase its differential semi-major axis relative to the observing satellite. This results in a decrease in the duration of the access interval and the time between access intervals, which is evident in both subplots of Figure 6.17. In this way the access interval analysis is not limited to the time between observations, but can be combined with data regarding the duration of the observation and used in conjunction with the angular rates data to yield more confident hypothesis.

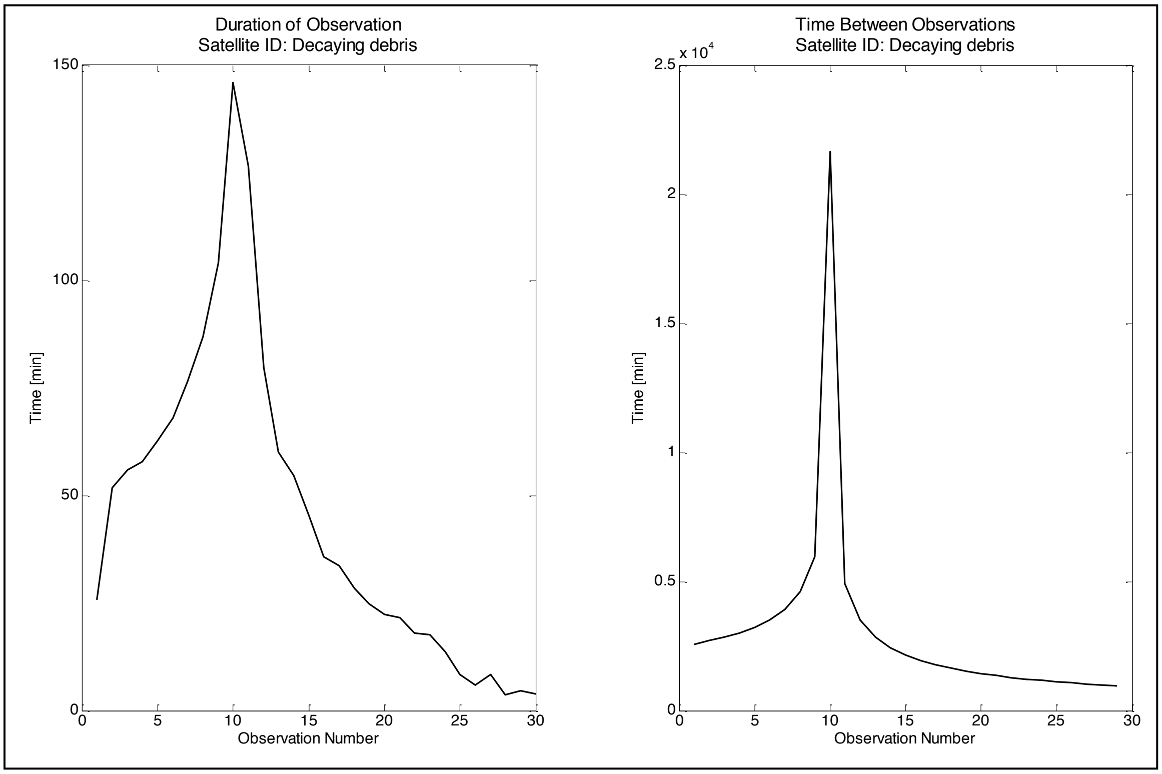

Figure 6.17: Access interval data – decaying debris scenario

6.5. Conclusions

For the orbital scenarios presented in this chapter, key findings suggest that trends concerning the orbit of an object in low-Earth orbit (LEO) can be extracted in terms of a differential semi-major axis relative to the observing satellite and the object's orbital type. The observing satellite was placed in a particular polar low-Earth orbit in order to study the trajectory of debris objects that will pass through such an orbital plane. This orbit was chosen because it is believed that a significant amount of currently untracked, that is not cataloged, space debris may pass through this set of orbits.

The different orbital types are meant to be representative of the orbits that LEO-based debris will experience due to J2 perturbation and during its decay back to Earth due to atmospheric drag.

The purpose of the access interval analysis is to determine if the different orbit types have characteristic access times associated with them that can act as an orbit type discriminator. This hypothesis is confirmed as characteristic trends concerning the orbital type and differential semi-major axis are evident in both the access duration and the time between subsequent accesses. Information extracted from the access interval analysis provides the means to determine the semi-major axis of an observed object relative to the semi-major axis of a known circular polar low-Earth orbiting sensor platform. This analysis determines the differential-semi-major axis metric based on consecutive observations of the object. Furthermore, when considering the levels extracted from the access interval analysis, it is shown that the upper levels tend to be more useful than lower levels because of the contrast in the magnitude of the values at the upper levels. This increased contrast between the upper levels leads to a more effective discriminator relative to the lower levels. This study has also demonstrated that when both the upper and lower levels resulting from the access interval analysis can be realized, orbital type and differential semi-major axis can be uniquely identified. This knowledge in terms of orbital type and differential semi-major axis provide an alternative to two-line elements sets for rapidly providing warning regarding potential collisions. Also, for the interval analysis-based discriminator to work successfully, it was conditioned on the prospect of the observing sensor to be able to faithfully register the object over multiple passes. Efforts are ongoing to seeking more effective and practical means for the space-based correlation and registration problem.

Since registration is not a trivial problem, an alternative for orbital-type and differential semi-major axis discrimination is shown to be possible through the angular rate of the projection of the object on the FPA. This angular rate discriminator is not as robust as the interval analysis-based discriminator, however it can be performed during the onset of access and yield a much quicker hypothesis on the orbital type and differential semi-major axis of the observed object. After each complete pass the angular rate discriminator becomes more accurate in uniquely identifying the orbital type and differential semi-major axis of the observed object. The angular rate discriminator utilizes the magnitude at onset, duration, peak magnitude, and envelope magnitude of the full-track angular rate curves in either the horizontal or vertical axes. With this analysis, the angular rate discriminator can be used as an effective tool for the rapid analysis of an object's orbital trajectory and provide information on whether or not it may pose a collision possibility on current or future passes. The decaying debris example shows that information gleaned from both analyses can be of practical use the SGP4, propagator taking atmospheric drag into account. While the interval analysis-based discriminator produces this information with a higher fidelity, it is at the cost of requiring registration and consecutive observations. The decaying debris case, orbital type 5, shows how the access interval analysis is not limited to the time between observations, but can be combined with data regarding the duration of the observation and used in conjunction with the angular rates data to yield more confident hypothesis. This analysis provides the means for a collision warning system through the discrimination of orbital type and differential semi-major axis.

This research may aid efforts to constrain the admissible region. Constraints can be placed on the admissible region including, range, eccentricity, semi-major axis, and characterization of the orbital type of the debris object from either ground-based or space-based observations. This research shows the feasibility for realizing information regarding orbital type and differential semi-major axis from space-based observations, which in turn can be utilized for constraining the admissible region for initial orbit determination.

For the purposes of this study it has been assumed that the sensor will always first detect the debris object at exactly 500 km. In reality, the range of detection depends on many factors including illumination conditions, or in the case of a thermal sensor on temperature, which vary as the object goes into and out of eclipse. A radar sensor would not be subject to this constraint. Future work can investigate how this technique can be applied to a realistic scenario where the initial range is not so clearly defined. This technique is sensitive to the ellipticity and inclination of the orbit of the observed object, as these factors affect the magnitude of the angular rate plots as well as the access intervals. Other future work will focus on efforts to determine a metric for degree of orbit similarity as well as include other intermediary orbits within the orbital evolution process due to the J2 perturbation.

7. RADIOMETRIC ANALYSIS

Space-based characterization of debris in low-Earth orbit via LWIR imaging

Every space launch increases the overall amount of space debris, especially when circumstances result in the orbital objects being stranded in orbit with no de-orbiting capabilities. Studies contributing to the understanding of space debris aid spacecraft operators in mitigating risk associated with Earth-orbiting debris objects. Accurately characterizing the debris threat to a spacecraft is of vital importance in maximizing the lifespan and mission capabilities of the spacecraft. This investigation aims to build LWIR radiometric models of typical debris and use these models to develop techniques for detecting and characterizing the debris object by signal analysis of unresolved imagery.

7.1. Introduction

The threat of collisions with space debris has become a significant source of concern, with over 3000 known and registered satellites and/or payloads orbiting the Earth as of April 2013 [89]. Providing essential commercial, military, and personal services to billions of people in a host of nations has made space utilization a priority in the coming years [75]. With all data showing that there will be no reduction in the rates at which nations send satellites into orbit, it can be assumed that the number of both trackable and un-trackable debris objects will increase.

As the number of debris objects increase, it will become even more important to detect, track, and characterize these objects, so they can be avoided with minimal impact to services or fuel consumption. An attractive option is to use compact, inexpensive sensors on spacecraft so they can observe such objects as they pass in their vicinity. In order to create compact, simple on-board sensors for the analysis of debris objects, it is most efficient to observe them at their dominant thermal emission wavelengths as predicted by Wien's Displacement Law [76]. Since orbital debris will have temperatures ranging from approximately 100-400K, their emissions will be primarily in the 7-30 μm waveband. Long-wave infrared (LWIR) sensors in the 7-14 μm wavebands, which are commercially available, would be attractive options to consider, especially when the development of a prototype system is considered. Thus, the goal of this investigation is to build LWIR radiometric models of typical types of debris and use these models to develop techniques for detecting and characterizing the debris object by signal analysis of unresolved imagery.

Previous work by the authors developed such models for near-geostationary debris, as observed from a geostationary-based satellite [90]. To adapt the GEO models and analysis to LEO it is imperative to include more representative thermal models of the debris in LEO, including the effects of cyclic solar illumination and earthshine. Debris size, shape, and orbit will all be modulated and simulated according to openly available debris data obtained from the United States Space Surveillance Network (SSN) [89]. Materials properties such as solar absorptivity and emissivity, which were either empirically defined or chosen from various spacecraft materials handbooks, will be accounted for and simulated.

The current investigation includes the development of detection algorithms, novel debris characterization techniques, and extraction of further information from the radiometric analysis of the unresolved debris imagery. Accurately characterizing the debris threat to a spacecraft will be of vital importance in maximizing the lifespan and mission capabilities of the spacecraft.

7.2. Methods

The radiometric analysis documented in this chapter makes use of the STK 10 software suite [83] for the visualization and investigation of several orbital scenarios. A satellite with a sensing platform is placed in a pre-determined polar orbit for observation of space debris in multiple Low-Earth orbits. The STK software suite yields many data providers for each sensor-to-debris observation. These data providers include range from sensor-to-debris, projection angles relative to sensor boresight, debris projections on the sensor focal plane array, and debris temperature using the STK Space Environment and Effects Tool (SEET).

The STK SEET software is a powerful tool that allows for space environmental modeling including the space radiation environment, the South Atlantic Anomaly, particle impacts, and magnetic fields. This work will model the temperature of the debris using the STK SEET software. The thermal aspects of the STK SEET software allow for customizable parameters including the solar absorptivity, emissivity, cross-sectional area, geometry, and orientation of the space debris, along with determination of Earth albedo. This parameterization allows for the approximation of the mean debris temperature as a function of direct solar flux, Earth albedo and long-wave radiation. It is assumed that space debris will have no means of generating internal energy, therefore the aforementioned processes encompass the main components of an appropriate thermal model for the estimation of mean space debris temperature. The details of the different simulated debris are shown in Table 7.1, [91]. The absorptivity, emissivity, cross-sectional area, orientation of the space debris tumble direction, and tumble-rate will vary throughout simulations. The debris sizes were chosen based upon the limit of detectability by the SSN. With the lower bound for detection via the SSN being 0.10 m, the 0.01 case is theoretically un-detectable, and the 0.25 m case should be more easily detected.

Table 7.1: Simulated space debris details

Debris Type	Emissivity	Absorptivity	Debris Size [m]	Tumble-Rate [rpm]	Tumble Type
Graphite Epoxy	0.850	0.930	0.010	0.010	Cross-Track
Titanium	0.120	0.520	0.100	0.100	About Nadir
Anodized Titanium Foil	0.100	0.700	0.250	1.000	
Aluminum Foil	0.027	0.143			
Ge-coated Kapton Sheldal 1 mil	0.911	0.698			
Sheldahl Black Kapton ITAR 100XC	0.906	0.930			
ITO coated 10 mil Sheldall Silvered Teflon	0.502	0.596			

The space debris described in Table 7.1 will be subjected to differing Low-Earth orbits relative to the sensor platform. This will allow for the generalization of results and conclusions across multiple orbits in which space debris may be observed. For this analysis, the orbital elements of the observing satellite are displayed in Table 7.2, while the different orbits that the debris will be subjected to are shown in Table 7.3. The orbits chosen for orbital debris simulations represent in-plane circular low-Earth orbits with a differing semi-major axis of 50 km – 200 km relative to the observing satellite.

Table 7.2: Initial orbital elements of observing satellite

Semi-major Axis	Eccentricity	Inclination	Argument of Perigee	RAAN	True Anomaly
7178.14 km	0	98	0	0	0

Table 7.3: Orbital characteristics of simulated debris objects

Orbit	Semi-major Axis	Eccentricity	Inclination	Propagator
Circular - Prograde	6978.14 km	0	98°	J2
Circular - Prograde	7078.14 km	0	98°	J2
Circular - Prograde	7128.14 km	0	98°	J2
Circular - Prograde	7228.14 km	0	98°	J2
Circular - Prograde	7278.14 km	0	98°	J2
Circular - Prograde	7378.14 km	0	98°	J2

Once range, orientation, projection, and temperature data are extracted for each simulation from the STK software, the data is sent to MATLAB for radiometric modeling and simulation according to the following equations. Utilizing Equations 4.2 through 4.5, which are defined and detailed in Chapter 4, Planck's equation for blackbody radiation, sensor throughput, and radiant flux, the radiant flux of the received signal at the detector is analyzed.

For all simulations, sensor-to-debris observations will be constrained by the range of the defined local area. In this dissertation the local area is defined as a 500 km radius sphere surrounding the orbiting sensor platform. For all times debris objects pass within this local area, a point source derived from the received radiant flux will be projected on the focal plane array (FPA) of the observing sensor and subjected to further analysis.

7.3. Results

The signal received at the detector will be analyzed in terms of Watts as derived by Equation 4.5. The radiant flux, Φ, at the detector is dependent upon the temperature of the debris object and detector waveband as indicated in Equations 4.2 and 4.3. The received signal at the detector is also a function of the angles and distance between the sensor and the debris object, as well as the cross-sectional area of the emitter, or debris object, and the detector, or sensor, as indicated in Equation 4.4. When analyzing the signal as it is represented in Equation 4.5, the data will contain information regarding the aforementioned parameters. The following sub-sections will focus on extraction of this data from the original signal. Projected area, tumble rates, and material analysis are of particular interest.

Parameters A1 and A2 from Equation 4.4 represent the projected area of the debris object emitting radiation and the area that object projects on the FPA of the detector. The simulations conducted account for three separate tumble-rates from 0.01 to 1 rotations per minute (rpm). The tumble-rate of the debris object necessitates dynamics in the projected area of the debris object that is being observed by the sensor. In order to detail the wavelet decomposition analysis, a scenario will be illustrated with the debris object having the orbital characteristics outlined earlier in the fifth data row of Table 7.3. The material being simulated will be Titanium with a tumble-rate of 1 rpm and a 0.25 m^2 cross-sectional area.

7.3.1. Tumble-Rate Analysis

The wavelet decomposition for the aforementioned scenario is shown in Figure 7.1. All graphs illustrating temporal-based analysis stemming from wavelet decomposition, Figures 7.1 through 7.6, have time in seconds as the unit for their x-axis. For this analysis a discrete approximation of the Meyer wavelet is utilized. Meyer wavelets are analytic wavelets whose Fourier Transform is band-limited, meaning it has compact support [92]. The wavelet decomposition separates the signal into a number of different scales set by the level of decomposition. In this way, the wavelet decomposition acts as an adaptive filtering technique in which the user can determine the spectral resolution via setting the number of levels for the decomposition. The received signal is decomposed into a varying number of levels using the Meyer wavelet until an approximation of the signal is reconstructed which is free of the high-frequency components that compose the tumble-rate data. The resultant approximation yielded, denoted as a4, from this analysis along with the original signal and wavelet tree are shown in Figure 7.1. The wavelet tree illustrates the successive levels of high-pass and low-pass filtering at varying levels of decomposition. The original signal shown in red in the sub-figure at the top half of Figure 7.1 contains high-frequency components, while the approximation of the signal at the fourth level of decomposition is devoid of the high-frequency components and will be used for later analysis.

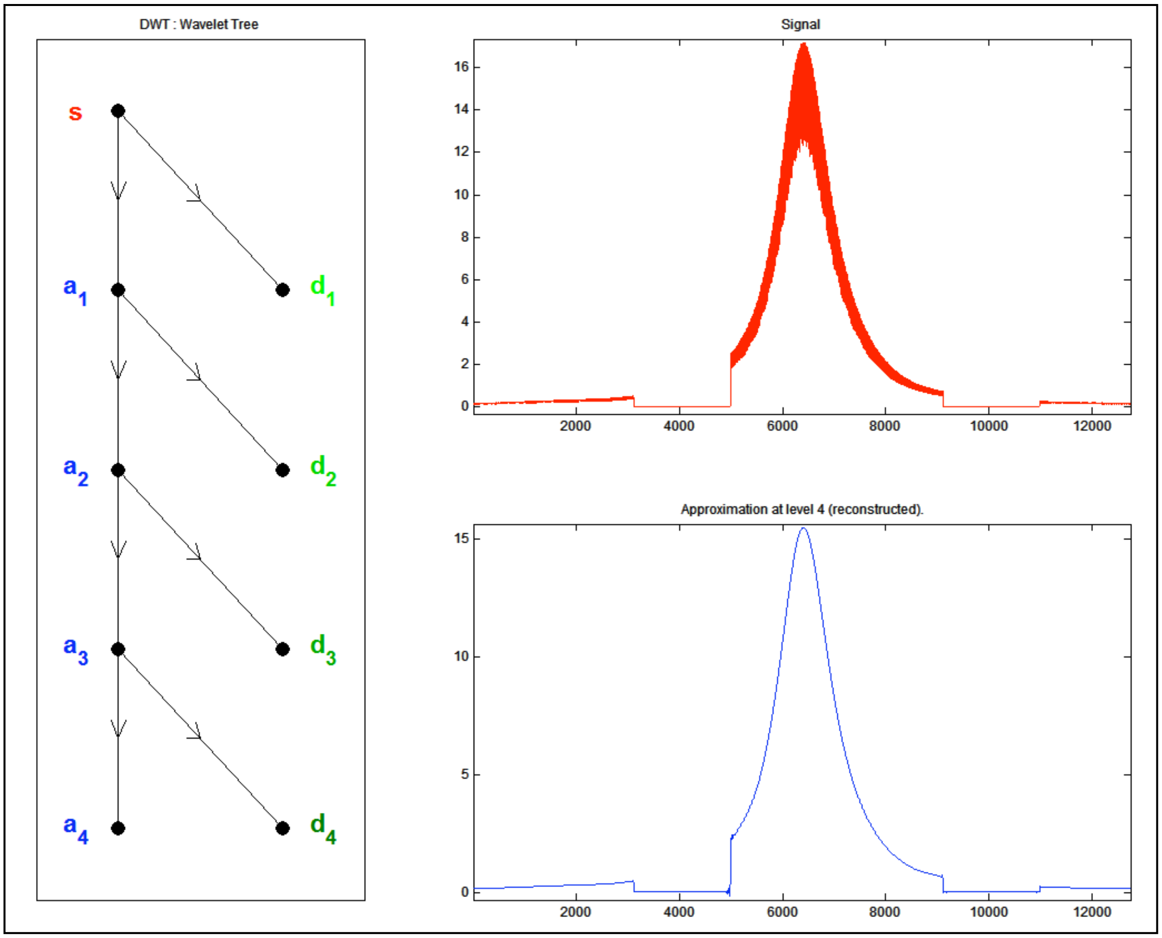

Figure 7.1: Wavelet decomposition overview

After the signal has been deconstructed to a level where the approximation at the last level does not contain the tumble-rate data, the details of the deconstructed signal can be analyzed as they will contain the extracted tumble-rate date. The signals containing the details at both the first and last level of decomposition contain data that can aid in the determination of tumble-rate. At the first level of decomposition the details, d1, will contain higher frequency components than the d4 details at the last level of decomposition. Both signals contain data that aids in the determination of the tumble-rate of the debris object. The d1 signal contains high-intensity high-frequency bursts that represent timestamps that are cataloged and can be used for tumble-rate determination. The d4 signal contains lower frequency components relative to the d1 signal due to the filter bank and wavelet tree associated with the wavelet decomposition process. The d4 signal's peaks and troughs align with the high-frequency peaks and troughs that are evident in the original signal. These timestamps, either the peaks or troughs of the d4 signal, can be used for tumble-rate determination as well. The decomposed detail signals for the last level are shown in Figures 7.2 through 7.4 for all three simulated tumble-rates.

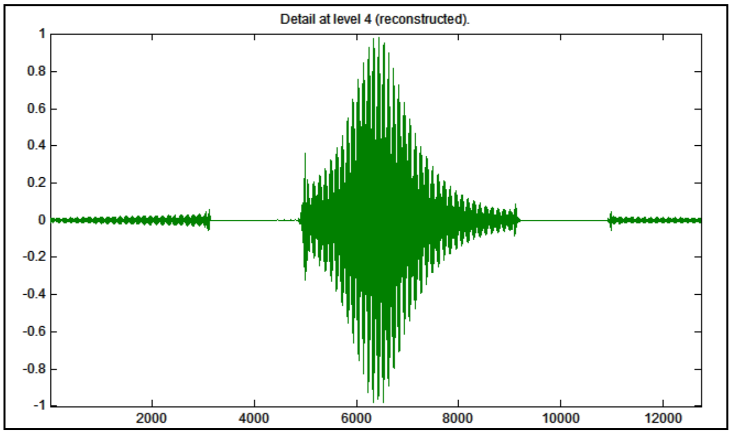

Figure 7.2: Tumble-rate data – 1 rpm

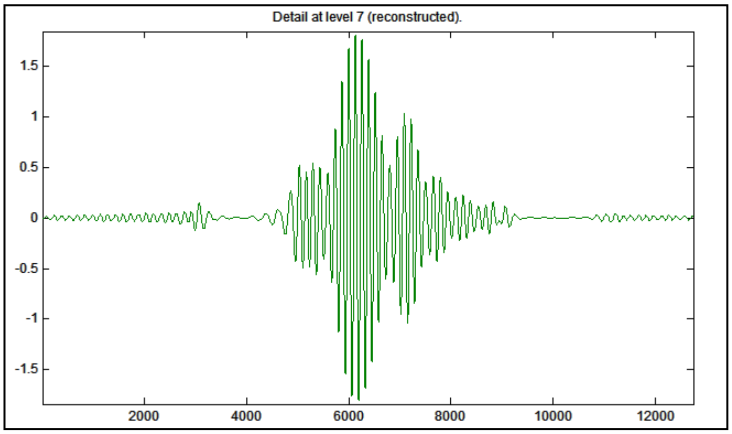

Figure 7.3: Tumble-rate data – 0.1 rpm

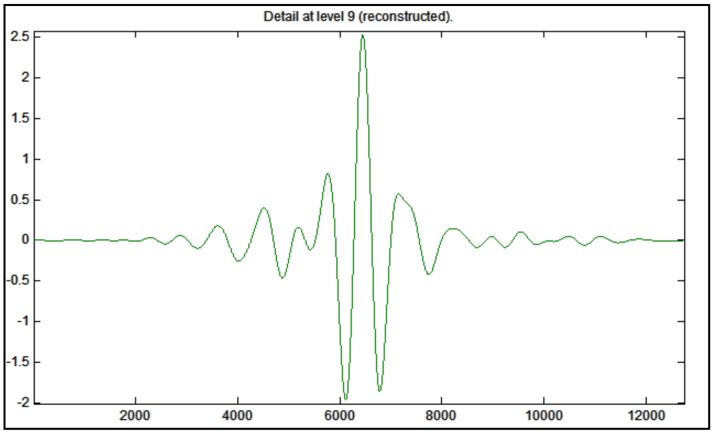

Figure 7.4: Tumble-rate data – 0.01 rpm

The first and last levels of the decomposed details yield deterministic tumble-rate information for the two faster tumble-rates, 0.1 and 1 rpm. The tumble-rate determination is done by extracting the timestamps from five consecutive peaks or troughs. Since the simulations assume cuboid geometries and specific tumble directions, the peaks will represent rotational projections of the four sides that will be observed. This process is illustrated in Figure 7.5 and evaluated in Equation 7.1.

$$Tumble\ Rate = \frac{60}{T_{peak-2} - T_{peak-1}}\ [\text{rpm}] \tag{7.1}$$

The "Peak - 1" and "Peak – 2" parameters in Equation 7.1 represent the magnitude of the peaks used for the tumble-rate determination, while "Tpeak - 1" and "Tpeak – 2" represent the timestamps associated with those peaks. However, for the slower tumble-rate, 0.01 rpm, the wavelet decomposition does not deterministically evaluate the tumble-rate of the observed debris object. This is because the tumble-rate information can no longer be extracted via filtering techniques alone when the tumble-rate is significantly slow. When the tumble-rate is significantly slow, other factors including range to debris object and absorptivity-to-emissivity ratio become the dominating factors affecting the dynamics of the received radiant flux signal. The slow tumble-rate scenario exhibits the constraint for this analysis in regards to tumble-rate analysis for this orbital simulation.

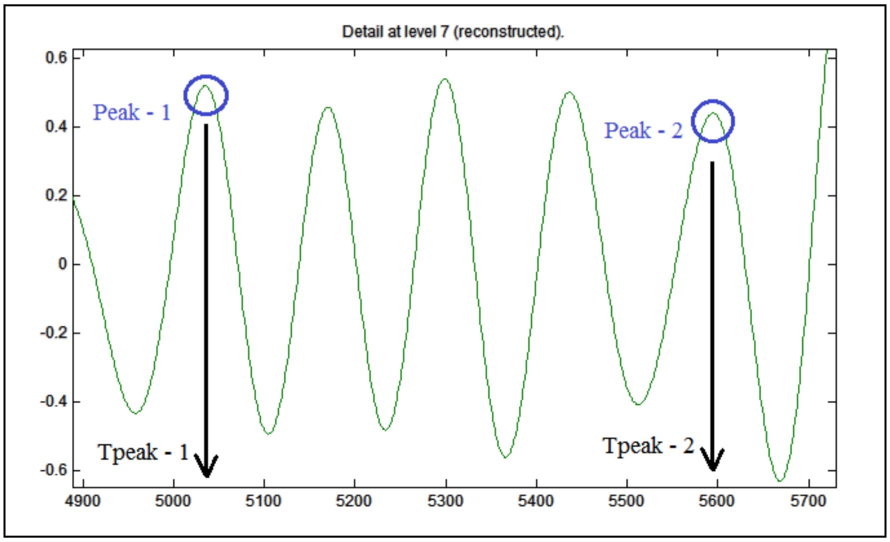

Figure 7.5: Tumble-rate determination – 0.1 rpm

7.3.2. Materials Analysis

At certain levels of the decomposition, information can be extracted regarding the time intervals in which the debris object is most likely undergoing a significant temperature transition. The temperature transition of the debris object is due directly to the object either entering or exiting solar eclipse. By precisely identifying these temperature transition intervals, the received power at the detector can be co-registered and the resulting change in power at the detector can be analyzed. The identification of the onset of temperature transitions derived from the details at the first level of wavelet decomposition is shown in Figure 7.6 with circles highlighting the transition regions. The local thermal equilibrium of an object in space will be proportional to the material's absorptivity-to-emissivity (α-to-ε) ratio, Equation 7.2, with ‘T_E’ representing the non-material dependent thermal equilibrium temperature [50].

$$T_{debris} = \sqrt[4]{\left(\frac{\alpha}{\varepsilon}\right)} * T_E \tag{7.2}$$

Since it is assumed that the materials will reach local thermal equilibrium both in- and out-of-eclipse, the power received at the detector will change according to the resulting temperature of the observed object. The change in received power will occur quickly relative to the corresponding change in range and projection on the FPA, therefore the resulting signal transition will be indicative of the material’s α-to-ε ratio.

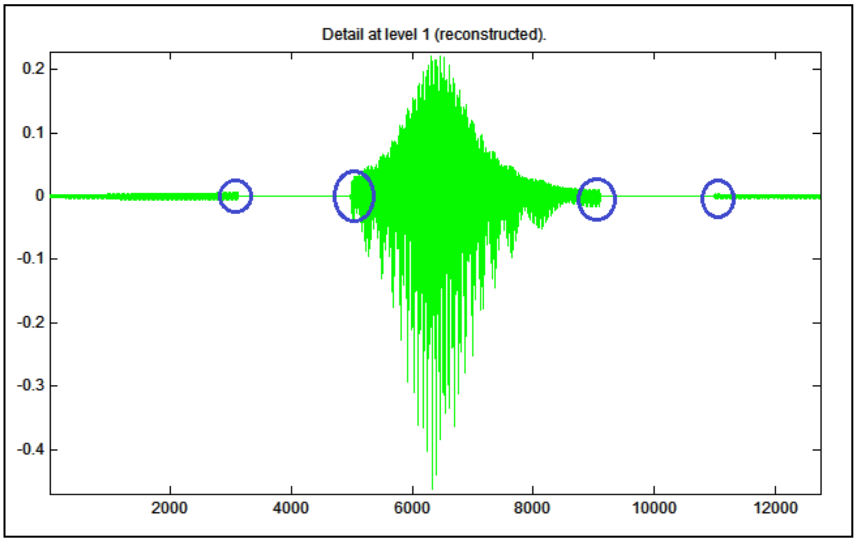

Figure 7.6: Thermal transition identification

The metric used for determination of the α-to-ε ratio will be the change in received signal power at the detector as represented in decibels (dB). The dB calculation for this analysis is expressed in Equation 7.3. The received radiant flux at the detector corresponding to the local thermal equilibrium when the debris object is in-eclipse is used as the reference power, P_0, for the dB calculation, thus resulting in positive dB values.

$$L_{\mathrm{dB}} = 10\mathrm{Log}_{10}(\frac{P_1}{P_0}) \tag{7.3}$$

For each debris object observation, there is an opportunity for multiple temperature changes due to the debris object entering or exiting solar eclipse. For each detected temperature transition, a data point is logged reflecting the corresponding change in power at the detector in dB. Figure 7.7 shows the box plot and relative distribution of the derived dB values for all debris object simulation observations. The box plot illustrates the median value for all data points represented by the marker within the box, while the box itself shows the 25% – 75% range of values around the median, which is referred to as the main lobes. The whiskers extending from the top and bottom of the box demonstrate the entire range of derived values. While there is overlap in terms of dB between different α-to-ε ratio bands, it is important to note the actual α-to-ε ratios for these materials. Most of the overlap occurs for materials where α-to-ε ratios are similar. The data is illustrative of perfect disambiguation between the main lobes of the box plot for the Ge-coated Kapton Sheldal 1 mil, Graphite Epoxy, Titanium, Aluminum Foil, and Anodized Titanium Foil materials; which comprises five out of the seven materials used for simulation.

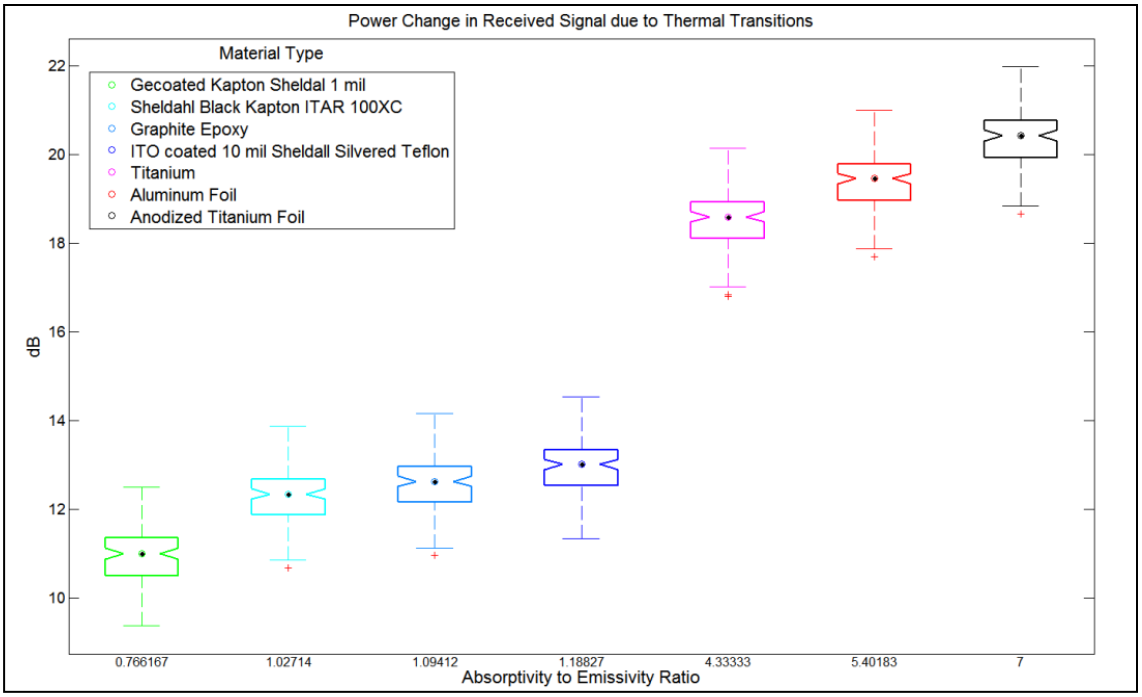

Figure 7.7: α-to-ε ratio analysis – box plot

7.3.3. Cross-Sectional Area Analysis

As described earlier, the wavelet decomposition is performed until an approximation of the signal at the last level of decomposition is lacking the high-frequency data necessary for the tumble-rate analysis. This signal is then used for analysis of the cross-sectional area of the observed debris object across all orbital scenarios. For each object observation the peak magnitude is logged in terms of Watts for all orbital scenarios. Figure 7.8 shows the result of this analysis with the y-axis representing the peak magnitude and the x-axis representing the cross-sectional area for all orbital scenarios. While it can be seen from this figure that discrimination can be performed based on the cross-sectional area of the debris object, there exists significant overlap in regards to the peak magnitude metric which prevents higher-confidence findings. However, if information is made available regarding the range or type of orbit this discrimination between cross-sectional areas may become more straightforward.

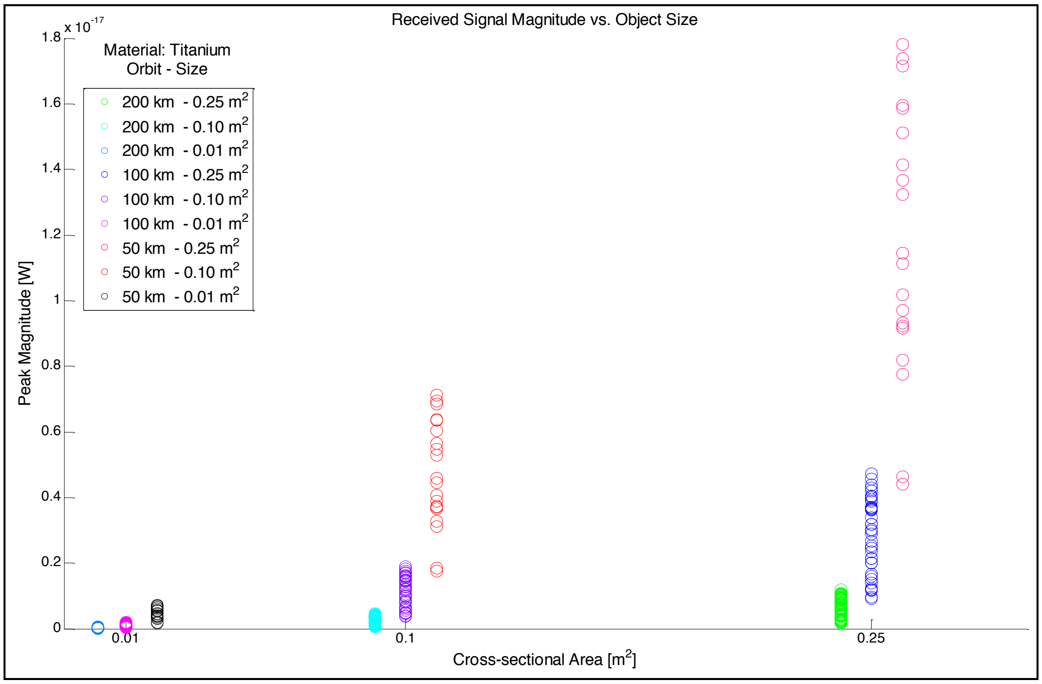

Figure 7.8: Cross-sectional area analysis

The box plots for this data are shown in Figure 7.9, with the subplots representing the different orbital scenarios. Once rudimentary orbital data is known, the ability to disambiguate between cross-sectional areas of the observed debris object is significantly increased. The box plots contained in Figure 7.9 demonstrate that for all data there exists no overlap in the main lobes of the box plot. The discrimination between cross-sectional areas is only non-intuitive where data is yielded outside of the main lobes, +/- 2.7 σ, for the 0.1 m^2 and 0.25 m^2 cases.

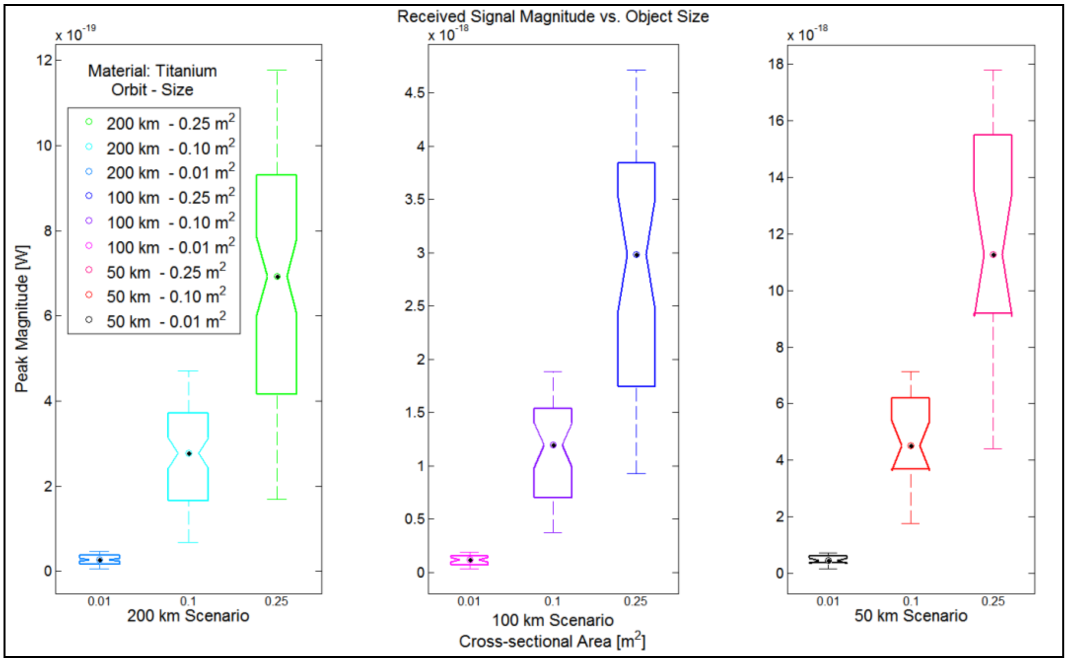

Figure 7.9: Cross-sectional area analysis - box plot

7.4. Conclusions

The power received at the focal plane array (FPA) of a detector due to an observed object is a function of range, object temperature, object projection onto the FPA, cross-sectional area of the emitting and receiving surface, as well as the absorptivity and emissivity of the observed object material. Through wavelet decomposition of the received signal it is possible to separate out information regarding the physical, material, orbital, and thermal aspects of the observed debris object.

For an assumed cuboid debris object structure, wavelet decomposition allows for tumble-rate determination to be performed on the details signal at the last level of decomposition. This analysis yields deterministic tumble-rate information for the two faster tumble-rates simulated at 0.1 and 1 rpm. The slowest tumble-rate contained in these simulations, 0.01

rpm, cannot be identified via wavelet decomposition. This is due to other factors, including range to object and the absorptivity-to-emissivity (α-to-ε) ratio, which could be the dominant factors affecting the dynamics of the received radiant flux signal at the detector. The tumble-rate analyses produce the same conclusions when analyzing both cross-track and about nadir tumble directions. This means that it is difficult to discern between tumble directions for the simulated scenarios. The materials analysis performed via wavelet decomposition allows for disambiguation between the α-to-ε ratios of the simulated debris materials. Discrimination between α-to-ε ratios is performed by analyzing the change in power at the detector thermal transitions associated with the debris object entering and exiting solar eclipse. The materials analysis is more effective when the α-to-ε ratios are not similar and are separated by more than twenty percent. Cross-sectional area analysis is possible utilizing the last level approximation via wavelet decomposition. The peak magnitude of this signal is indicative of the cross-sectional area of the observed debris. However without preliminary information regarding the orbit of the debris object, disambiguation amongst cross-sectional areas is complicated due to overlap in the distribution of the data. If data is made available regarding the orbit of the debris object, the ability to disambiguate between cross-sectional areas of the observed debris may increase significantly.

Work remains to be done simulating more orbital scenarios and various low-Earth orbits. Many other orbital scenarios will lack the long duration observations that are available with the orbits simulated at this current phase of the research. The aforementioned analysis becomes more effective when coupled with the orbital data of the observed debris object.

8. CONCLUSIONS

The research presented here has been aimed at the modeling and characterization of debris in low-Earth orbit with the goal of extracting information that will lead to knowledge about the possible origin, trajectory, and characteristics of space debris moving through the relative proximity of a space-based observing platform. This is defined for our purposes as Local Area Awareness.

The astrometric modeling efforts were focused on a methodology for describing the movement of an object across the focal-plane array of a space-based sensor as a means for the estimation of orbital information. The results presented in Chapter 3 demonstrate the ability of the pixel-speed classifier to characterize the orbits of local area geostationary objects. The proposed classifier provides a means of rapidly distinguishing objects that pose a possible collision hazard within the local area of the sensor platform.

Chapter 4 detailed the radiometric modeling efforts via incorporation of a long-wave infrared sensor. All simulations in Chapter 4 were run with a sensor platform in geostationary orbit. This was done with the goal of understanding how temperature transitions, differing material emissivities, and attitude states of debris contribute to the received radiant flux on an arbitrary detector on a very slow time scale (twenty-four hours at geostationary orbit). This knowledge was subsequently applied via long-wave infrared radiant modeling of debris at LEO from a space-based platform in Chapter 7.

As the long-wave infrared signature of an object is dependent upon temperature, Chapter 5 highlighted the thermal modeling of space debris in low-Earth orbit. Debris objects were modeled with differing materials utilizing both real and hypothetical values for their material and thermal properties for this investigation. The radiance profile was calculated for each face of the cuboid debris object which was simulated in a polar low-Earth orbit. Simplifying assumptions were made regarding the temperature of debris objects as a result of the Finite Element Analysis.

Chapter 6 detailed the astrometic analyses on the basis of the different models that were investigated. For the orbital scenarios presented in Chapter 6 key findings suggest that trends concerning the orbit of an object in low-Earth orbit can be extracted in terms of a differential semi-major axis relative to the observing satellite and the object's orbital type.

In Chapter 7 the radiometric analysis of space debris is documented. Through wavelet analysis information regarding the tumble-rate, material properties, and size of an observed debris object may be extracted. Further analysis and characterization is possible via fusion of the radiometric and astrometric analyses.

Documented in this dissertation are key methods which are shown to be quite effective for the detection, characterization, and extraction of useful information regarding resident space objects as they move through the space environment surrounding a spacecraft as a means of increasing a satellite's Local Area Awareness.

REFERENCES

[1] P. S. Laplace, *Mémoires de l'Académie Royale des Sciences*. Paris, France: Reprinted in Laplace's CollectedWorks 10(93), 1780.

[2] K. F. Gauss, *Theoria motvs corporvm coelestivm in sectionibvs conicis solem ambientivm*. Hambvrgi, Svmtibvs F. Perthes et I. H. Besser, 1809.

[3] D. Farnocchia, G. Tommei, A. Milani, and A. Rossi, "Innovative methods of correlation and orbit determination for space debris," *Celest. Mech. Dyn. Astron.*, vol. 107, no. 1–2, pp. 169–185, Apr. 2010.

[4] P. Escobal, *Methods of orbit determination*. Malabar, FL: Krieger Publishing Company, 1965.

[5] R. H. Gooding, "A New Procedure for Orbit Determination Based on Three Lines of Sight (Angles Only)," 1993.

[6] G. Tommei, a. Milani, and a. Rossi, "Orbit determination of space debris: admissible regions," *Celest. Mech. Dyn. Astron.*, vol. 97, no. 4, pp. 289–304, Feb. 2007.

[7] L. Ansalone and F. Curti, "A genetic algorithm for Initial Orbit Determination from a too short arc optical observation," *Adv. Sp. Res.*, vol. 52, no. 3, pp. 477–489, Aug. 2013.

[8] K. Fujimoto and D. J. Scheeres, "Applications of the admissible region to space-based observations," *Adv. Sp. Res.*, vol. 52, no. 4, pp. 696–704, Aug. 2013.

[9] T. Kelecy and M. Jah, "Analysis of high area-to-mass ratio (HAMR) GEO space object orbit determination and prediction performance: Initial strategies to recover and predict HAMR GEO trajectories with no a priori information," *Acta Astronaut.*, vol. 69, no. 7–8, pp. 551–558, Sep. 2011.

[10] J. Li, W. An, and Y. Zhou, "Initial orbit determination and correlation of the uncatalogued targets with too short arcs in space-based optical surveillance," *Aerosp. Sci. Technol.*, vol. 21, no. 1, pp. 41–46, Sep. 2012.

[11] A. Milani, G. F. Gronchi, and Z. Knez, "Orbit determination with very short arcs. I admissible regions," *Celest. Mech. Dyn. Astron.*, vol. 90, no. 1–2, pp. 59–87, 2004.

[12] a Milani, G. Gronchi, Z. Knezevic, M. Sansaturio, and O. Arratia, "Orbit determination with very short arcs II. Identifications," *Icarus*, vol. 179, no. 2, pp. 350–374, Dec. 2005.

[13] a. Milani, D. Farnocchia, L. Dimare, a. Rossi, and F. Bernardi, "Innovative observing strategy and orbit determination for Low Earth Orbit space debris," *Planet. Space Sci.*, vol. 62, no. 1, pp. 10–22, Mar. 2012.

[14] a. Milani, G. Tommei, D. Farnocchia, a. Rossi, T. Schildknecht, and R. Jehn, "Correlation and orbit determination of space objects based on sparse optical data," *Mon. Not. R. Astron. Soc.*, vol. 417, no. 3, pp. 2094–2103, Nov. 2011.

[15] D. Kaya, D., Snow, "Short arc initial orbit determination using angles-only space-based observations," in *Proceedings AAS/AIAA Astrodynamics Specialists Conference, Vol. 29*, 1991.

[16] D. Snow, D., Kaya, "Short arc orbit determination using angles-only space-based observations," in *Proceedings AAS/AIAA Spaceflight Mechanics Meeting*, 1992, pp. 57 – 74.

[17] D. L. H. L.G. Taff, "The Use of Angles and Angular Rates I: Initial Orbit Determination," *Celest. Mech.*, vol. 16, no. 4, pp. 481–488, 1977.

[18] D. L. H. L.G. Taff, "The Use of Angles and Angular Rates II: Multiple Observation Initial Orbit Determination," in in *Celestial Mechanics*, vol. 21, 1980, pp. 281–290.

[19] K. J. DeMars, M. K. Jah, and P. W. Schumacher, "Initial Orbit Determination using Short-Arc Angle and Angle Rate Data," *IEEE Trans. Aerosp. Electron. Syst.*, vol. 48, no. 3, pp. 2628–2637, Jul. 2012.

[20] G. J. Der, "New Angles-only Algorithms for Initial Orbit Determination," in *Advanced Maui Optical and Space Surveillance Technologies Conference*, 2012, pp. 412–427.

[21] R. R. Karimi and D. Mortari, "Initial orbit determination using multiple observations," *Celest. Mech. Dyn. Astron.*, vol. 109, no. 2, pp. 167–180, Dec. 2010.

[22] J. Tombasco and P. Axelrad, "Observability of Relative Hybrid Elements, Given Space-Based Angles-Only Observations," *J. Guid. Control. Dyn.*, vol. 35, no. 5, pp. 1681–1686, Sep. 2012.

[23] D. A. Vallado, "Evaluating Gooding Angles-only Orbit Determination of Space Based Space Surveillance Measurements," in *Paper 10-S4.5 presented at U.S. Russian Workshop. Maui, HI*, 2010, pp. 1–21.

[24] P. . Krisko, "EVOLVE historical and projected orbital debris test environments," *Adv. Sp. Res.*, vol. 34, no. 5, pp. 975–980, Jan. 2004.

[25] N. L. Johnson, P. H. Krisko, J.-C. Liou, and P. . Anz-Meador, "NASA ' S NEW BREAKUP MODEL OF EVOLVE 4 . 0," *Adv. Sp. Res.*, vol. 28, no. 9, pp. 1377–1384, 2000.

[26] J.-C. Liou, D. . Hall, P. . Krisko, and J. . Opiela, "LEGEND – a three-dimensional LEO-to-GEO debris evolutionary model," *Adv. Sp. Res.*, vol. 34, no. 5, pp. 981–986, Jan. 2004.

[27] J. Liou, M. J. Matney, P. D. Anz-meador, and N. Carolina, "The New NASA Orbital Debris Engineering Model ORDEM2000," 2002.

[28] Y.-L. Xu, M. Horstman, P. H. Krisko, J.-C. Liou, M. Matney, E. G. Stansbery, C. L. Stokely, and D. Whitlock, "Modeling of LEO orbital debris populations for ORDEM2008," *Adv. Sp. Res.*, vol. 43, no. 5, pp. 769–782, Mar. 2009.

[29] P. . Anz-Meador and M. . Matney, "An assessment of the NASA explosion fragmentation model to 1 mm characteristic sizes," *Adv. Sp. Res.*, vol. 34, no. 5, pp. 987–992, Jan. 2004.

[30] P. H. Krisko, M. Horstman, and M. L. Fudge, "SOCIT4 collisional-breakup test data analysis: With shape and materials characterization," *Adv. Sp. Res.*, vol. 41, no. 7, pp. 1138–1146, Jan. 2008.

[31] S. K. Flegel, J. Gelhaus, M. Möckel, C. Wiedemann, H. Krag, H. Klinkrad, and P. Vörsmann, "Multi-layer insulation model for MASTER-2009," *Acta Astronaut.*, vol. 69, no. 11–12, pp. 911–922, Dec. 2011.

[32] C. Wiedemann, S. Flegel, J. Gelhaus, H. Krag, H. Klinkrad, and P. Vörsmann, "NaK release model for MASTER-2009," *Acta Astronaut.*, vol. 68, no. 7–8, pp. 1325–1333, Apr. 2011.

[33] H. Krag, T. Flohrer, and S. Lemmens, "Consideration of Space Debris Mitigation Requirements in the Operation of LEO Missions," in *SpacOps COnference*, 2012.

[34] M. S. David Sibert, Maj David Borgeson, Glenn Peterson, Alan Jenkin, "OPERATIONAL IMPACT OF IMPROVED SPACE TRACKING ON COLLISION AVOIDANCE IN THE FUTURE LEO SPACE DEBRIS ENVIRONMENT," in *Advanced Maui Optical and Space Surveillance Technologies Conference*, 2010.

[35] J. Liou, "Low-Earth Orbit Environment Remediation with Active Debris Removal," *NASA Bienn. Res. Rep.*, vol. 273, pp. 273–274, 2011.

[36] D. Mehrholz, "Radar detection of mid-size debris," *Adv. Sp. Res.*, vol. 16, no. 11, pp. 17–27, Jan. 1995.

[37] D. Mehrholz, “RADAR OBSERVATIONS IN LOW EARTH ORBIT,” vol. 19, no. 2, pp. 203–212, 1998.

[38] D. Mehrholz, “Radar techniques for the characterization of meter—sized objects in space,” *Adv. Sp. Res.*, vol. 28, no. 9, pp. 1259–1268, Jan. 2001.

[39] X. Bai, M. Xing, A. Member, F. Zhou, Z. Bao, and S. Member, “High-Resolution Three-Dimensional Imaging of Spinning Space Debris,” vol. 47, no. 7, pp. 2352–2362, 2009.

[40] T. Sato, “Shape estimation of space debris using single-range Doppler interferometry,” *IEEE Trans. Geosci. Remote Sens.*, vol. 37, no. 2, pp. 1000 – 1005, 1999.

[41] L. Hong, F. Dai, and H. Liu, “Sparse Doppler-only snapshot imaging for space debris,” *Signal Processing*, vol. 93, no. 4, pp. 731–741, Apr. 2013.

[42] J. Morio and F. Muller, “Spatial object classification by radar measurements,” *Aerosp. Sci. Technol.*, vol. 14, no. 4, pp. 259–265, Jun. 2010.

[43] J. . Africano, E. . Stansbery, and P. . Kervin, “The optical orbital debris measurement program at NASA and AMOS,” *Adv. Sp. Res.*, vol. 34, no. 5, pp. 892–900, Jan. 2004.

[44] P. W. Kervin, J. L. Africano, P. F. Sydney, and D. Hall, “Small satellite characterization technologies applied to orbital debris,” *Adv. Sp. Res.*, vol. 35, no. 7, pp. 1214–1225, Jan. 2005.

[45] D. Hall, K. Hamada, T. Kelecy, and P. Kervin, “Surface Material Characterization from Non-resolved Multi-band Optical Observations,” in *Advanced Maui Optical and Space Surveillance Technologies Conference*, 2012.

[46] M. Laas-Bourez, G. Blanchet, M. Boër, E. Ducrotté, and A. Klotz, “A new algorithm for optical observations of space debris with the TAROT telescopes,” *Adv. Sp. Res.*, vol. 44, no. 11, pp. 1270–1278, Dec. 2009.

[47] M. Laas-Bourez, D. Coward, A. Klotz, and M. Boër, “A robotic telescope network for space debris identification and tracking,” *Adv. Sp. Res.*, vol. 47, no. 3, pp. 402–410, Feb. 2011.

[48] T. Schildknecht, R. Musci, and T. Flohrer, “Properties of the high area-to-mass ratio space debris population at high altitudes,” *Adv. Sp. Res.*, vol. 41, no. 7, pp. 1039–1045, Jan. 2008.

[49] T. Schildknecht, C. Früh, J. Herzog, A. Hinze, and A. Vananti, "AIUB EFFORTS TO SURVEY, TRACK, AND CHARACTERIZE SMALL-SIZE OBJECTS AT HIGH ALTITUDES," in *Advanced Maui Optical and Space Surveillance Technologies Conference*, 2010.

[50] J. V. Lambert, T. J. Osteen, and W. A. Kraszewski, "Determination of debris albedo from visible and infrared brightnesses," in *Space Debris Detection and Mitigation*, 1993, vol. 1951, pp. 32–36.

[51] C. M. Alcala and J. H. Brown, "Space Object Characterization Using Time-Frequency Analysis of Multi-spectral Measurements from the Magdalena Ridge Observatory," in *Advanced Maui Optical and Space Surveillance Technologies Conference*, 2009.

[52] M. D. Hejduk, M. D. Cowardin, and E. G. Stansbery, "Satellite Material Type and Phase Function Determination in Support of Orbital Debris Size Estimation," in *Advanced Maui Optical and Space Surveillance Technologies Conference*, 2012.

[53] T. Yanagisawa and A. Nakajima, "Detection of Small LEO Debris with Line Detection Method," *Trans. Jpn. Soc. Aeronaut. Space Sci.*, vol. 47, no. 158, pp. 240–248, 2005.

[54] T. Yanagisawa and H. Kurosaki, "Shape and motion estimate of LEO debris using light curves," *Adv. Sp. Res.*, vol. 50, no. 1, pp. 136–145, Jul. 2012.

[55] M. Oswald, H. Krag, P. Wegener, and B. Bischof, "Concept for an orbital telescope observing the debris environment in GEO," *Adv. Sp. Res.*, vol. 34, no. 5, pp. 1155–1159, Jan. 2004.

[56] T. Flohrer, T. Schildknecht, and R. Musci, "Proposed strategies for optical observations in a future European Space Surveillance network," *Adv. Sp. Res.*, vol. 41, no. 7, pp. 1010–1021, Jan. 2008.

[57] T. Flohrer, H. Krag, H. Klinkrad, and T. Schildknecht, "Feasibility of performing space surveillance tasks with a proposed space-based optical architecture," *Adv. Sp. Res.*, vol. 47, no. 6, pp. 1029–1042, Mar. 2011.

[58] W. P. Seniw, "LWIR Observations of Geosynchronus Satellites," in *MIT Lincoln Laboratories Space Control Conference*, 1993, pp. 21 – 30.

[59] M. a. Skinner, R. W. Russell, R. J. Rudy, D. J. Gutierrez, D. L. Kim, K. Crawford, S. Gregory, and T. Kelecy, "Time-resolved infrared spectrophotometric observations of high area to mass ratio (HAMR) objects in GEO," *Acta Astronaut.*, vol. 69, no. 11–12, pp. 1007–1018, Dec. 2011.

[60] M. a. Skinner, R. W. Russell, T. Kelecy, S. Gregory, R. J. Rudy, D. J. Gutierrez, D. L. Kim, and K. Crawford, "Further analysis of infrared spectrophotometric observations of high area to mass ratio (HAMR) objects in GEO," *Acta Astronaut.*, vol. 80, pp. 154–165, Nov. 2012.

[61] J. A. Dawson and C. T. Bankston, "Space debris characterization using thermal imaging systems," in *Advanced Maui Optical and Space Surveillance Technologies Conference*, 2010.

[62] A. Harms, K. Hamada, C. J. Wetterer, K. Luu, C. Sabol, and K. T. Alfriend, "UNDERSTANDING SATELLITE CHARACTERIZATION KNOWLEDGE GAINED FROM RADIOMETRIC DATA," in *Advanced Maui Optical and Space Surveillance Technologies Conference*, 2011.

[63] E. M. Gaposchkin and R. J. Bergemann, "Infrared Detections of Satellites with IRAS," in *MIT Lincoln Laboratories Space Control Conference*, 1995.

[64] A. K. Mainzer, P. Eisenhardt, E. L. Wright, F. Liu, W. Irace, I. Heinrichsen, R. Cutri, and V. Duval, "Preliminary Design of The Wide-Field Infrared Survey Explorer," in *SPIE – UV/Optical/IR Space Telescopes: Innovative Technologies and Concepts II.*, 2005, pp. 262 – 273.

[65] S. D. Price and M. P. Egan, "Spaced based infrared detection and characterization of near earth objects," *Adv. Sp. Res.*, vol. 28, no. 8, pp. 1117–1127, Jan. 2001.

[66] M. Griffiths, "Space Debris," *Parliam. Off. Sci. Technol.*, no. 355, pp. 1–4, 2010.

[67] J.-C. Liou, "Avoiding Satellite Collisions in 2009," *NASA Orbital Debris Q. News*, vol. 14, no. 1, 2010.

[68] C. Jaramillo, *Space Security*. 2010.

[69] T. Watson, "Two Satellites Collide 500 Miles Over Siberia," *USA Today*, 12-Feb-2009.

[70] J. Tombasco, "Orbit Estimation of Geosynchronous Objects Via Ground-Based and Space-Based Optical Tracking," University of Colorado, 2011.

[71] M. G. S. Bruno and J. M. F. Moura, "Multiframe Detector Tracker Opti2mal Performance," *IEEE Trans. Aerosp. Electron. Syst.*, vol. 37, no. 3, pp. 925 – 945, 2001.

[72] Z. Liu, D. Zhao, and Z. Jiang, "A background rejection method based on star-point matching in star-background image," in *Proc. SPIE 6795, Second International Conference on Space Information Technology*, 2007.

[73] K. Sun, W. Zhou, Q. Wu, and J. Yu, "Star-point moving target detection and tracking on star space background," *Int. J. Digit. Content Technol. its Appl.*, vol. 6, no. 5.15, pp. 124 – 135, 2012.

[74] W. P. Yang, Z. A. Shen, and Z. Y. Li, "Application of difference method to dim point target detection in infrared images," in *SPIE Signal and Data Processing of Small Targets, vol.2235*, 1994, pp. 258 – 263.

[75] J. West, *Space Security 2009*. 2010.

[76] C. L. Wyatt, *Electro-Optical System Design For Information Processing*. New York: McGraw-Hill, 1991.

[77] "Emissivity Values for Metals," *Emissivity of Metals*, 2013. [Online]. Available: www.raytek.com.

[78] "Emissivity of Specific Materials," *Technical Resource Library from Cole-Parmer*, 2013. [Online]. Available: www.coleparmer.com.

[79] "Hawaii Infrared Parallax Star Catalog," *Strasbourg astronomical Data Center*, 2012. [Online]. Available: http://cds.u-strasbg.fr.

[80] W. J. Smith, *Modern Optical Engineering*. New York: Mcgraw-Hill, 2007.

[81] F. Niklaus, H. Jakobsen, and C. Vieider, "MEMS-based uncooled infrared bolometer arrays: a review," in *MEMS/MOEMS Technologies and Applications III, 68360D*, 2008.

[82] "MATLAB." The Mathworks, Natick, Massachusetts, USA, 2013.

[83] "Systems Tool Kit." Analytic Graphics Inc., Exton, Pennsylvania, 2013.

[84] P. McCall, R. Sharples, J. H. Andrian, A. Barreto, N. Rishe, and M. Adjouadi, "Thermal modeling of space debris via Finite Element Analysis," in *Advanced Maui Optical and Space Surveillance Technologies Conference*, 2013.

[85] P. D. McCall, M. L. Naudeau, M. E. Sorge, T. Farrell, and M. Adjouadi, "Rapid orbital characterization of local area space objects utilizing image-differencing techniques," in *Sensors and Systems for Space Applications VI*, 2013, vol. 8739, pp. 873908–1 – 873908–8.

[86] "Orbit Propagators for Satellite, STK 10.0.1, Programming Interface." 2013.

[87] C. Frueh and M. Jah, "Detection Probability of Earth Orbiting Objects Using Optical Sensors," in *Astrodynamic Specialist Conference*, 2013.

[88] C. Frueh, M. Jah, E. Valdez, P. Kervin, and T. Kelecy, “Taxonomy and Classification Scheme for Artificial Space Objects,” in *Advanced Maui Optical and Space Surveillance Technologies Conference*, 2013.

[89] “Space Object Catalog,” *Space-Track.org*, 2013. .

[90] P. D. McCall, M. L. Naudeau, T. Farrell, M. E. Sorge, and M. Adjouadi, “Sensor model for space-based local area sensing of debris,” in *Infrared Imaging Systems: Design, Analysis, Modeling, and Testing XXIV*, 2013, vol. 8706, pp. 87060M–1 – 87060M–11.

[91] D. G. Gillmore, *Satellite Thermal Control Handbook*. El Segundo, CA: Aerospace Corporation, 1994.

[92] L. Debnath, *Wavelet Transforms and Time-frequency Signal Analysis*. Boston, MA: Birkhäuser, 2001.

Appendix A: Finite Element Analysis details for thermal simulations

To begin building a simulation-based database of temperature profiles of debris in orbit, the FEA-based thermal simulation tool in SolidWorks was used to simulate the temperature of cuboid structures representing a small part of the debris tradespace. Results and conclusions drawn from these simulations will be used to justify simplifications that make simulating a much larger part of the entire debris tradespace more feasible.

The first set of FEA simulations examined the thermal profile of a cuboid geometry with respect to time. A 10cm hollow cube with a 5mm shell, a 17cm hollow cube with an 8.5mm shell, and a 10cm solid cube were exposed to the heat flux produced from a nadir-pointing circular orbit in LEO. Note that the 17cm cube with an 8.5mm shell is simply scaled up from the 10cm cube with a 5mm shell. Each cuboid geometry was simulated with three in-orbit tumble rates: 0.01, 0.1, and 1.0 revolutions per minute. In addition to the effects of the orbit on the thermal profile, the simulations also examined the effect of overall mass, the absorptivity-to-emissivity (α/ε) ratio, and the mechanical thermal properties of different materials on each cube's thermal profile.

Aluminum 7075 was chosen as the initial material for simulation, since it is a common material used in CubeSat structures. CubeSat aluminum structures are also often chromanodized, so the emissivity and absorptivity values were set to 0.56 and 0.44, respectively, which represent chromanodized aluminum [91]. A separate set of simulations with emissivity of 0.56 and absorptivity of 1.0 were also run to determine the effect of increased absorptivity-to-emissivity ratio on the thermal profile. (Note that the second set of values for absorptivity and emissivity are not realistic, as $\alpha + \varepsilon$ should sum to 1.) These values and ratios are listed in Table A.1.

Table A.1: Absorptivity and emissivity values for chromanodized comparative coating

Property	Chromanodized Value	Comparison Value
Emissivity (ε)	0.56	0.56
Absorptivity (α)	0.44	1.0
α/ε	0.79	1.79

The chromanodized absorptivity/emissivity ratio was also applied to titanium, along with two purely theoretical materials: Al-7075 with the specific heat (c_p) of titanium and Al-7075 with the conductivity (k) of titanium. The goal of simulating these three additional materials is to first isolate the effects of different specific heat and conductivity values on the overall thermal profile and then to examine the combined effects of these two mechanical thermal properties in a realistic material. Table A.2 summarizes the materials used along with their thermal and material properties.

Table A.2: Thermal and material properties used for simulations

Material	$c_p \left[\frac{J}{kg * K}\right]$	$k \left[\frac{W}{m * K}\right]$	$\rho \left[\frac{kg}{m^3}\right]$	α/ε
Al-7075	960	130	2810	0.79, 1.79
Al7075_cpTi	520	130	2810	0.79
Al7075_kTi	960	16.4	2810	0.79
Titanium	520	16.4	4510	0.79

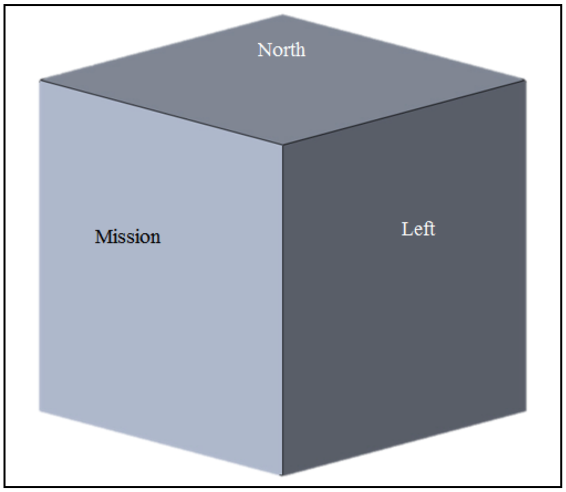

Figure A.1: Solid model rendering of a cube

A solid model of the cuboid geometry as rendered in SolidWorks is shown in Figure A.1. The Mission, anti-mission, right, left, north, and south faces were assigned to the cube according to convention for application of the orbit-determined heat flux.

The radiance profiles described in the previous section were used to create a database of face-by-face heat flux profiles in SolidWorks. Each face had an individual heat flux profile of 8641 points with a time step of 10 seconds in between each point that was uploaded to that face from the database. Since the heat flux profiles are based on the geometry of orbit, in this way orbit was simulated for each object. SolidWorks, however, will only allow 5000 points at a time in any heat flux profile in the database. To fit into the database format, the 8641-point profiles were split into two separate files, one 5000 points long and the other 3641 points long. When the first simulation was complete (up to 49990 seconds) using the first 5000 points, the thermal profile from the final time step was used as the initial thermal profile for a new simulation that would cover the remaining 3641 points. For objects that took longer than 86410 seconds to reach steady state, the heat flux profile was repeated—i.e., another simulation using the final time step's thermal profile (point 3641) as the initial thermal profile was run with the heat flux profile starting over for the first 5000 points. Absorptivity of the object is also a parameter set during this part of simulation set-up. This process was repeated until the object had achieved steady state.

All six faces were set to radiate surface-to-ambient to 77K, which is the standard ambient radiation temperature in Time-domain Analysis Simulation for Advanced Tracking (TASAT), with the desired emissivity value as discussed previously. In addition, the entire object was set to an initial temperature of 77K. However, one limitation of SolidWorks is that initial temperature values can only be set on the surfaces of an object, not throughout the entire object. To create this initial temperature profile, all six faces were set to 77K and run to steady state without a transient analysis, thus creating a 77K temperature profile throughout the entire object. The result of this simulation was set as the initial thermal profile of the first transient simulation as the initial thermal condition.

All simulations used a time step size of 10 seconds and were run with a coarse mesh and SolidWorks' FFEPlus iterative solver. Figure A.2 shows the coarse mesh over a 10cm cube. Simulations were run and their final thermal profiles fed into the next simulation as the new initial thermal profile, thus keeping continuity from one simulation to the next and allowing for longer simulations to be run than the heat flux profile size limitations would allow, until the object reached steady state.

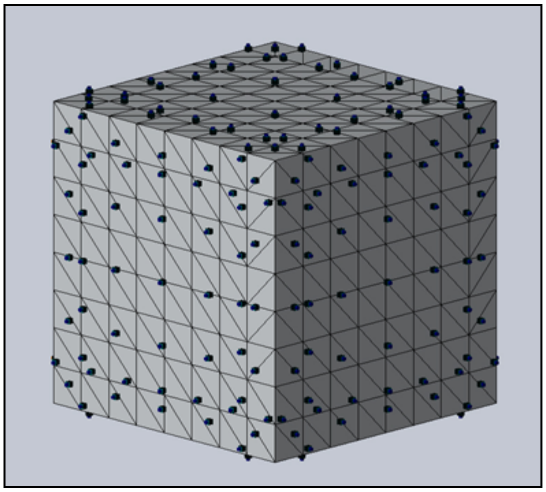

Figure A.2: Coarse finite element mesh applied to hollow 10cm cube in SolidWorks

Each simulation produces a comprehensive set of results. It is possible to pull the temperature from any element at any 10-second time step. The software can also calculate the maximum, minimum, and bulk temperature with respect to time for any surface of the object. For this study, only the bulk temperature of the mission, anti-mission, and north faces with respect to time were used.

One way that SolidWorks Simulation presents results is a visual representation of the temperature gradient of the object at any single time step of the simulation. An example of this type of thermal profile for a 10cm hollow cube with absorptivity 0.44 and tumble rate 1.0 rpm is shown in Figure A.3.

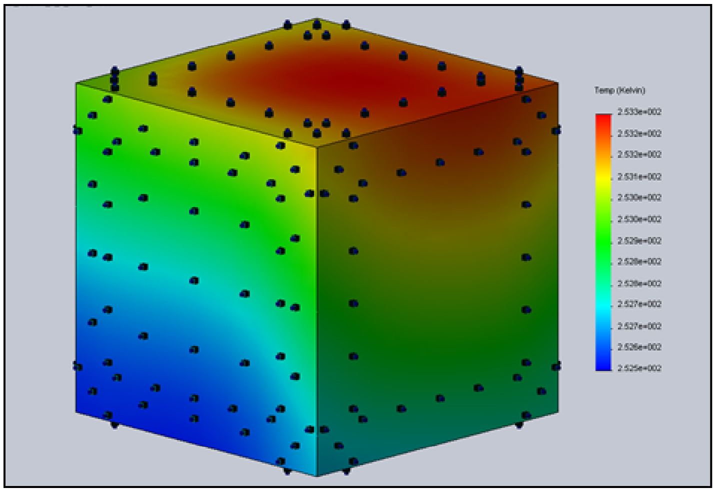

Figure A.3: Thermal profile at time 49990 seconds for a 10cm Al-7075 hollow cube with absorptivity 0.44 in a circular, nadir-pointing orbit with a 1.0 rev/min tumble rate at LEO

The thermal profiles from each time step can also be put together as an animation demonstrating shifts in the temperature gradient. For this study, SolidWorks was used to calculate the bulk temperature of each face with respect to time. This information was exported as a .csv file containing the time step, the time in simulation, and the calculated temperature. These files were then read into MATLAB for processing. If a simulation required more than one run, the file from each run for each face would be loaded separately and then plotted on a single graph for each face to check for continuity between time segments. The steady state portion of the data was then isolated by face. Figure A.4 shows the points used in this process for a chromanodized Al-7075 10cm hollow cube with a tumble rate of 0.01 rpm.

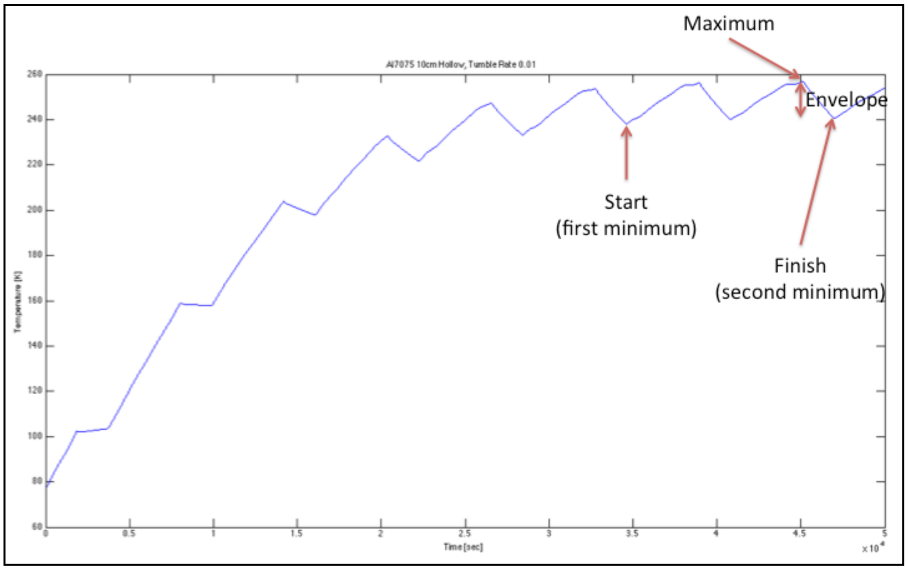

Figure A.4: Key points in steady-state analysis

The value and time of the first and last minimum temperatures after steady state were recorded to ensure that the steady state average was taken after *n* complete cycles and not mid-cycle. The steady-state average between these two minima was then calculated using MATLAB's average function. Once the average had been calculated for the mission, anti-mission, and north faces, the standard deviation between the three faces was also calculated using the STDEVP function in Excel. The value and time of the last maximum temperature between the two minima were also recorded. The final minimum was subtracted from the maximum to yield the thermal envelope.

Appendix B: Orbital simulation details for the different orbital scenarios

Table B.1: Orbital parameters for debris objects

Orbital Type	Semi-major Axis	Eccentricity	Inclination	Orbital Period [min]	Propagator
Circular - Prograde	6978.14 km	0	98°	96.6	J2
Circular - Prograde	7078.14 km	0	98°	98.7	J2
Circular - Prograde	7128.14 km	0	98°	99.8	J2
Circular - Prograde	7228.14 km	0	98°	101.9	J2
Circular - Prograde	7278.14 km	0	98°	102.9	J2
Circular - Prograde	7378.14 km	0	98°	105.1	J2
Crossing	6978.14 km	0	8°	96.6	J2
Crossing	7078.14 km	0	8°	98.7	J2
Crossing	7128.14 km	0	8°	99.8	J2
Crossing	7228.14 km	0	8°	101.9	J2
Crossing	7278.14 km	0	8°	102.9	J2
Crossing	7378.14 km	0	8°	105.1	J2
Circular - Retrograde	6978.14 km	0	98°	96.6	J2
Circular - Retrograde	7078.14 km	0	98°	98.7	J2
Circular - Retrograde	7128.14 km	0	98°	99.8	J2
Circular - Retrograde	7228.14 km	0	98°	101.9	J2
Circular - Retrograde	7278.14 km	0	98°	102.9	J2
Circular - Retrograde	7378.14 km	0	98°	105.1	J2

Elliptical	6978.14 km	0.057323	98°	96.6	J2
Elliptical	7078.14 km	0.028257	98°	98.7	J2
Elliptical	7128.14 km	0.014029	98°	99.8	J2
Elliptical	7228.14 km	0.013835	98°	101.9	J2
Elliptical	7278.14 km	0.02748	98°	102.9	J2
Elliptical	7378.14 km	0.054215	98°	105.1	J2

Table B.2: Orbital parameters for decaying debris scenario

Orbit	Mean Motion	Eccentricity	Inclination	Argument of Perigee
Decaying Debris	0.0570833 deg/sec	0	98	0
	RAAN	True Anomaly	Propagator	Bstar (B^*)
	0	0	SGP4	0.7

VITA

PAUL DAVID MCCALL

	Born, Hollywood, Florida
2008	B.S., Electrical Engineering Florida International University Miami, Florida
2010	M.S., Electrical Engineering Florida International University Miami, Florida
Fall 2010	National Collegiate Athletic Association Postgraduate Scholarship Recipient National Collegiate Athletic Association
Summer 2012	Outstanding Scholar Award Air Force Research Laboratory Kirtland Air Force Base, New Mexico
Spring 2012	Best Presentation Biomedical Studies FIU Annual Scholarly Forum
2010-2013	National Defense Science and Engineering Graduate Fellowship Recipient United States Department of Defense Department of the Air Force
Fall 2013	Betty G. Reader Graduate Scholarship Recipient Florida International University
2010-2013	Doctoral Candidate Florida International University Miami, Florida

PUBLICATIONS AND PRESENTATIONS

Paul D. McCall, Madeleine L. Naudeau, Marlon E. Sorge, Malek Adjouadi, "On-Orbit Trajectory Analysis of Local Area Low-Earth Orbit Objects", *Advances in Space Research [submitted]*

Paul D. McCall, Rachel Sharples, Jean H. Andrian, Armando Barreto, Naphtali Rishe, Malek Adjouadi, “Thermal modeling of space debris via Finite Element Analysis”, Presented at the *Advanced Maui Optical and Space Surveillance Technologies Conference*, Wailea-Maui, HI, Sept. 2013

Paul D. McCall, Madeleine L. Naudeau, Jean H. Andrian, Armando Barreto, Naphtali Rishe, Malek Adjouadi, “Space-based Characterization of Debris in Low-Earth Orbit via LWIR Imaging”, Presented at the *AAS/AIAA Astrodynamics Specialist Conference*, Hilton Head Island, SC, AAS 13-851, 2013

Paul D. McCall, “Local Area Sensors for GEO Space Situational Awareness”, Presented at the *AFRL – AFIT Space Colloquia,* Kirtland AFB, NM, July 2013 – *Secret*

Paul D. McCall, Madeleine L. Naudeau, Marlon E. Sorge, Thomas Farrell, Malek Adjouadi, “Rapid Orbital Characterization of Local Area Space Objects Utilizing Image-Differencing Techniques”, Proc. SPIE 8739, Sensors and Systems for Space Applications VI, 873908, pp. 1-8, (May 21, 2013); doi:10.1117/12.2017888.

Paul D. McCall, Madeleine L. Naudeau, Thomas Farrell, Marlon E. Sorge, Malek Adjouadi, “Sensor Model for Space-based Local Area Sensing of Debris”, Proc. SPIE 8706, Infrared Imaging Systems: Design, Analysis, Modeling, and Testing XXIV, 87060M, pp. 1-11 (June 5, 2013); doi:10.1117/12.2017890.

P. McCall, G. Torres, K. LeGrand, M. Adjouadi, C. Liu, J. Darling, and H. Pernicka, “Many-core computing for space-based stereoscopic imaging,” *Aerospace Conference, 2013 IEEE*, pp.1-7, 2-9 March 2013; doi: 10.1109/AERO.2013.6497430

McCall, P.; Cabrerizo, M.; Adjouadi, M., "Spatial and temporal analysis of interictal activity in the epileptic brain," *Signal Processing in Medicine and Biology Symposium (SPMB), 2012 IEEE*, pp.1-6, 1 Dec. 2012 doi: 10.1109/SPMB.2012.6469459

G. Torres, P. McCall, C. Liu, M. Cabrerizo, and M. Adjouadi, “Parallelizing Electroencephalogram Processing on a Many-Core Platform for the Detection of High Frequency Oscillations”, pp. 9-15, *Proceedings of the Seventh International Workshop on Unique Chips and Systems,*UCAS-7, New Orleans, Louisiana, February 26, 2012.